Advances in surface wave studies: 3D wavefield simulation across East Asia and imaging shear wave anisotropic structures beneath Alaska

by

Lili Feng

B.S., Geophysics, Peking University, Beijing, China, 2011

M.S., Geophysics, Peking University, Beijing, China, 2014

A thesis submitted to the

Faculty of the Graduate School of

the University of Colorado in partial fulfillment

of the requirement for the degree of

Doctor of Philosophy

Department of Physics

2019

This thesis entitled:

Advances in surface wave studies: 3D wavefield simulation across East Asia and imaging shear wave anisotropic structures beneath Alaska

written by Lili Feng

has been approved for the Geophysics Program in the Department of Physics

---

Michael H. Ritzwoller

Shijie Zhong

Date:_____

The final copy of this thesis has been examined by the signatories, and we find that both the content and the form meet acceptable presentation standards of scholarly work in the above mentioned discipline.

Feng, Lili (Ph.D., Geophysics)

Advances in surface wave studies: 3D wavefield simulation across East Asia and imaging shear wave anisotropic structures beneath Alaska

Thesis directed by Professor Michael H. Ritzwoller

Abstract

The development of computational tools and deployment of new and dense seismic arrays (e.g. USArray, ChinaArray) are accelerating the advancement of surface wave studies. Indeed, powerful numerical tools have made it feasible to perform wavefield simulation in 3D complex Earth's structures with high accuracy, and the seismic data collected by dense networks provide us unprecedented opportunity to infer the isotropic and anisotropic Earth's structures. The surface wave studies presented in this thesis are based on advanced computational techniques and high-quality seismic data. The thesis is organized in three parts, including 3D surface wavefield modelling and inferring shear wave anisotropic structures with surface waves.

In the first part of the thesis, I simulate seismic wavefield propagation through a recent 3D crustal and upper mantle model of East Asia. I demonstrate that significant Rayleigh wave amplification downstream from sedimentary basins could be produced by elastic focusing of low velocity anomalies inside the basins. Understanding this amplification effect could help us better estimate earthquake source parameters. This is the first systematic study of the basin residual effects on short period through-passing surface waves.

The second part of the thesis presents a model of the 3-D shear velocity structure of the crust and uppermost mantle beneath Alaska and surroundings, including crustal and mantle radial anisotropy. The model derives from a Bayesian Monte Carlo inversion of Rayleigh and Love wave dispersion data. The model captures several prominent features, including the subduction zones, cratonic areas, major sedimentary basins and mid-Cretaceous extensional regions. This study presents the first radially anisotropic model across Alaska and surroundings.

In the third part of the thesis, I present a hypothesis test to verify whether a simple two-layer azimuthally anisotropic model could fit azimuthal variation in Rayleigh wave phase speed

measurements. The hypothesis test confirms our understanding that the crustal azimuthal anisotropy is dominantly produced by deformationally-aligned cracks and fractures in the upper crust undergoing brittle deformation. It also infers the existence of vertically coherent deformation in the uppermost mantle. This is the first study that infers apparent shear wave azimuthal anisotropy beneath Alaska using surface waves from ambient noise and earthquakes.

Acknowledgement

This thesis would be impossible without the help of many people. Amount those, I particularly would like to thank my advisor Professor Michael H. Ritzwoller for his mentoring and support for the past five years. Mike treats me as a student when I need guidance but otherwise as a researcher to work independently. He always encourages me to have my own thoughts about research and persistently urges me to present my thoughts in a logically clear way. I benefit a lot from his motivation in science, immense knowledge and skills of critical thinking. Besides, he has been very patient to help me, as a foreign student, to write good scientific articles in English. In a lot of ways, Mike is a typical example what a good scientist and mentor should be.

People in our group also help me a lot. Weisen Shen, who was the post-doc when I joined the group five years ago, has been constantly helping me with my research. He also helped me a lot in personal life and I have learnt a lot from him. Ye Tian and Jiayi Xie were the senior students when I came to Boulder. Ye and I got to know each other when we were in high school. I have learnt a lot from him in coding skills and he is also a good friend to hang out with. Jiayi taught me how to perform inversion to infer anisotropic structures, most parts of this thesis is related to her work. I also would like to thank other people in our group. Hongda Wang, Chuanming Liu, Mengyu Wu and Shane Zhang are the junior students who joined our group years after me. I benefit a lot from discussing research problems with them. In particular, I would like to thank Hongda for being such a great roommate! Misha Barmin, as our computer administrator, provided numerous help in solving technique problems. The codes he wrote related to my research saved me a great amount of time. Anatoli Levshin, as the senior researcher, taught me a lot in surface wave theory. My thank also goes to other fellow students and post-docs that are not in our group, Ashley Bellas, Wei Mao, Min Yan, Mingming Li, Kaixuan Kang, Xi Liu, Chuan Qin, Baochen Wu and Xin Qian. Hanging out with you guys is a great fun!

My particular thank goes to Professor Shijie Zhong, Professor Michael Calkins, Professor Craig Jones and Professor Anne Sheehan, for being willing to serve as members of my thesis defense committee. I took classes from Shijie, Craig and Anne, and really learnt a lot in geodynamics and seismology from them. I also would like to thank Vera Schulte-Pelkum for being in my committee

for my comprehensive exam, and Teri Keeler for constantly helping me on various administration issues.

I would like to thank people in other institutes who helped me. I benefit from discussion with Roel Snieder, Fan-chi Lin, Yingjie Yang and Xin Liu. Xin is a good friend to me. My special thank goes to people that I got to know at Peking University. To Professor Yun-tai Chen and Professor Jieyuan Ning for their help and support. To Haoran Meng, Wenjun Xie and Yichao Wu, for being friends for life.

I would like to thank my parents, Xiaoling Li and Kaixiang Feng, for their unconditional love and support. Ever since my childhood, my mother has been always encouraging me that I can do something great and my father has been very supportive in a lot of ways. I am greatly indebted to them for raising me up. Finally, I want to thank my beloved girlfriend, Chun Hu. We got to know each other when we were thirteen years old and it was you who made me choose the path of physical sciences. Thank you so much for appearing in my life.

Table of Contents

List of Figures

List of Tables

Chapter 1

Introduction

1.1 Scientific Motivations and Objectives

Recent development of seismology benefits a lot from the advancement of computational tools and the deployment of dense seismic arrays (e.g., USArray, ChinaArray), which motivates the work presented in this thesis.

The rapid growth in computer capabilities facilitates computational seismologists to develop a variety of packages to solve seismic wave equation in 3D complex Earth's structures, making it cheaper and easier to perform seismic wavefield simulation. Combining the advanced computational tools with newly constructed high-resolution 3D Earth models (e.g., China Reference Model, Shen et al., 2016), it becomes feasible to accurately predict seismic ground motion. Ground motion prediction is important for a variety of reasons, it can help us to do better in seismic hazard assessment, estimation of earthquake source parameters and understanding seismic wave propagation effect. In order to determine earthquake magnitude more accurately, I investigate surface wave amplification effect caused by sedimentary basins using spectral element method to perform wavefield simulation through a 3D complex Earth model. This part of work is a typical example to show how to use powerful computational tools and high-resolution Earth model to improve our understanding of seismic wave propagation effect.

Another important part of the thesis is motivated by the willing to better understand the isotropic and anisotropic shear wave velocity structures beneath Alaska using surface wave tomography, based on high-quality seismic data collected by recently deployed dense seismic arrays. With newly developed Bayesian Monte Carlo inversion algorithm empowered by modern computational resources, I infer the 3D distribution of isotropic and anisotropic structures beneath Alaska in a

probabilistic approach. The new high-resolution 3D model that I construct is a stepping stone to a better understanding of Earth's interior structures and dynamical processes, and the model can also be used to make ground motion predictions to better assess potential seismic hazard. In this thesis, seismic anisotropy is also carefully studied, because it is typically associated with crustal and mantle deformation processes.

1.2 Roadmap

This thesis consists of a total of five chapters. Besides the introductory chapter (this chapter) and the concluding chapter at the end, there are three chapters on research findings, each formatted for journal publication. A brief summary of these three chapters is given as follows.

In Chapter 2, published in Geophysical Journal International as Feng & Ritzwoller (2017), we investigate Rayleigh wave amplification effect downstream from sedimentary basin based on wavefield simulations through a recent 3D crustal and upper mantle model of East Asia, with particular emphasis on continental basins and propagation paths, elastic structural heterogeneity, and Rayleigh waves at 10 s period. We show that surface wave amplification caused by basins results predominantly from elastic focusing and that amplification effects produced through 3D basin models are reproduced using 2D membrane wave simulations through an appropriately defined phase velocity map. The principal characteristics of elastic focusing in both 2D and 3D simulations include (1) retardation of the wavefront inside the basins; (2) deflection of the wave propagation direction; (3) formation of a high amplitude lineation directly downstream from the basin bracketed by two low amplitude zones; and (4) formation of a secondary wavefront. We illustrate with several examples how the size and geometry of the basin affects focusing. Finally, by comparing the impact of elastic focusing with anelastic attenuation, we argue that on-continent

sedimentary basins are expected to affect surface wave amplitudes more strongly through elastic focusing than through the anelastic attenuation.

In Chapter 3, submitted to Journal of Geophysical Research as Feng & Ritzwoller (2019), we present a model of the 3-D shear velocity structure of the crust and uppermost mantle beneath Alaska and surroundings on a ~50 km grid, including crustal and mantle radial anisotropy, based on seismic data recorded at more than 500 broadband stations. The model derives from a Bayesian Monte Carlo inversion of Rayleigh wave group and phase speeds and Love wave phase speeds determined from ambient noise and earthquake data. Prominent features resolved in the model include: (1) Apparent crustal radial anisotropy is strongest across the parts of central and northern Alaska that were subject to significant extension during the Cretaceous, consistent with crustal anisotropy being caused by deformationally-aligned middle to lower crustal sheet silicates (micas) with shallowly dipping foliation planes beneath extensional domains. (2) Crustal thickness estimates are similar to those from receiver functions by Miller & Moresi (2018). (3) Very thick lithosphere underlies Arctic-Alaska, with high shear wave speeds that extend at least to 120 km depth, which may challenge rotational transport models for the evolution of the region. (4) Subducting lithosphere beneath Alaska is resolved, including what we call the “Barren Islands slab anomaly”, an “aseismic slab edge” north of the Denali Volcanic Gap, the “Wrangellia slab anomaly”, and Yakutat lithosphere subducting seaward of the Wrangell volcanic field. (5) The geometry of the Alaskan subduction zone generally agrees with the slab model Alaska_3D 1.0 of Jadamec & Billen (2010) except for the Yakutat “slab shoulder region”, which is newly imaged in our model.

In Chapter 4, to be submitted to Earth and Planetary Science Letters as Feng & Ritzwoller (2019), we present a complementary study of Chapter 3. It is essentially a hypothesis test to verify if the azimuthal variation of Rayleigh wave phase speed measurements can be fit with a simple two-layer azimuthally anisotropic model, with anisotropy confined in the brittle upper crust and uppermost mantle. The hypothesis test confirms our understanding that crustal azimuthal anisotropy is dominantly produced by deformationally-aligned cracks and fractures in the upper crust undergoing brittle deformation. Furthermore, by comparing with SKS splitting results, it provides evidence that vertically coherent deformation in the upper mantle generally exists across most parts of Alaska and surroundings.

Chapter 2

The Effect of Sedimentary Basins on Surface Waves That Pass Through Them

2.1 Summary

Surface waves propagating through sedimentary basins undergo elastic wavefield complications that include multiple scattering, amplification, the formation of secondary wavefronts, and subsequent wavefront healing. Unless these effects are accounted for accurately, they may introduce systematic bias to estimates of source characteristics, the inference of the anelastic structure of the Earth, and ground motion predictions for hazard assessment. Most studies of the effects of basins on surface waves have centered on waves inside the basins. In contrast, the purpose of this chapter is to investigate wavefield effects downstream from sedimentary basins, with particular emphasis on continental basins and propagation paths, elastic structural heterogeneity, and Rayleigh waves at 10 s period. Based on wavefield simulations through a recent 3D crustal and upper mantle model of East Asia, we demonstrate significant Rayleigh wave amplification downstream from sedimentary basins in eastern China such that Ms measurements made on the simulated wavefield vary by more than a magnitude unit. We show that surface wave amplification caused by basins results predominantly from elastic focusing and that amplification effects produced through 3D basin models are reproduced using 2D membrane wave simulations through an appropriately defined phase velocity map. The principal characteristics of elastic focusing in both 2D and 3D simulations include (1) retardation of the wavefront inside the basins; (2) deflection of the wave propagation direction; (3) formation of a high amplitude lineation directly downstream from the basin bracketed by two low amplitude zones; and (4) formation of a secondary wavefront. We illustrate with several examples how the size and geometry of the basin affects focusing. Finally, by comparing the impact of elastic focusing with anelastic attenuation,

we argue that on-continent sedimentary basins are expected to affect surface wave amplitudes more strongly through elastic focusing than through the anelastic attenuation.

2.2 Introduction

The Earth's interior is heterogeneous in composition and phase. This is particularly true near the Earth's surface, where the presence or absence of sedimentary basins is a principal contributor to lateral heterogeneity in the shallow Earth. However, because sedimentary basins amplify seismic noise, seismologists tend to site seismic stations outside of basins. Together with the fact that earthquakes commonly occur either deep within basins or below them, this means that seismic body waves are often recorded with a minimal imprint of the effect of basins. As a result, sedimentary basins are often poorly modeled (e.g., Xie et al., 2017) and this makes it more difficult to recover information about structures below them than in regions devoid of basins (e.g., Ferreira et al., 2010).

These considerations are not true for surface waves, which are trapped near Earth's surface and propagate through sedimentary basins even to stations that may be situated outside of them. Thus, surface waves hold key information about sedimentary basins and are affected by them strongly. There have been many studies of the effects of sedimentary basins on the amplification of surface waves that are recorded within a basin (e.g., Aki & Larner, 1970; Bard & Bouchon, 1980a,b; Bard et al., 1988; Kawase, 1996; Olsen et al., 1995, 2006, 2009; Olsen, 2000; Alex & Olsen, 1998; Graves et al., 2011; Day et al., 2012; Denolle et al., 2014; Bowden & Tsai, 2017). These studies interpret such amplitude effects as a "site response" of the basin, which is seen to terminate at the boundary of the basin. The physical cause of the site amplification inside basins is predominantly constructive interference between body waves and surface waves (e.g., Kawase, 1996), which is commonly regarded as a 2D vertical cross-section effect. In comparison, there are very few studies

of the residual effects on surface waves after they have passed through a basin. This is particularly true regarding the role of lateral heterogeneity on the surface waveforms at short to intermediate periods that propagate over regional distances, although surface wave focusing/defocusing caused by lateral heterogeneity has been studied at intermediate to long periods for waves that propagate over teleseismic distances (e.g., Lay & Kanamori, 1985; Woodhouse & Wong, 1986; Wang et al., 1993; Wang & Dahlen, 1995; Selby & Woodhouse, 2000; Yang & Forsyth, 2006).

The purpose of this chapter is to attempt to improve understanding of the nature of elastic propagation effects on surface waves, particularly their amplitudes downstream from sedimentary basins. The focus of the chapter is on lateral wavefield effects on Rayleigh waves at 10 sec period, which is typically well excited by small earthquakes and nuclear explosions and is also well represented in ambient noise cross-correlations that are commonly used in tomographic studies (e.g. Shapiro et al., 2005; Lin et al., 2007; Yang et al., 2007; Shen et al., 2013a,b; Shen & Ritzwoller, 2016; Kang et al., 2016). The existence and nature of sedimentary basins strongly affect regionally propagating Rayleigh waves at this period. To the best of our knowledge, the work we present here is the first systematic study of the basin residual effects on short period through-passing surface waves. As discussed below, our results indicate that a significant fraction of the observed amplitude variability is caused by 2D elastic focusing/defocusing due to lateral wave propagation effects. The amplitude anomalies caused by 2D focusing/defocusing can be significantly larger than site amplification inside basins as well as anelastic attenuation.

We mention now two examples how this chapter are relevant to other studies.

(1) The inference of the anelastic structure of the Earth based on surface wave amplitude information may be biased by amplitude effects caused by elastic structures. Some studies of surface wave attenuation have taken focusing/defocusing into account (e.g., Dalton & Ekstrom,

2006; Dalton et al., 2008; Bao et al., 2016), but have applied corrections only at long periods. At shorter periods, surface wave attenuation tomography has been performed by extracting amplitude information from ambient noise (e.g., Prieto et al., 2009; Lawrence & Prieto, 2011). Such studies typically assume, however, that focusing and defocusing average out in the data processing. Ignoring elastic focusing effects can produce locally negative values of effective Q which are actually commonly observed but are often discarded in observational studies (e.g., Levshin et al., 2010).

(2) Source characterization generally, and moment or magnitude estimation specifically, depend in part on interpreting the amplitude of surface waves that propagate at regional distances. Strong amplitude effects imparted to surface waves by elastic heterogeneities may bias magnitude estimates and other source characteristics. This may be particularly important in the context of nuclear discrimination. Indeed, the ability to discriminate nuclear explosions from naturally occurring seismic events such as earthquakes rests in part on the ability to measure reliably and interpret the amplitude of body waves and surface waves that are generated by these sources. Body and surface wave amplitude measurements are commonly converted into the magnitude estimates mb and Ms, respectively. Although many nuclear explosions are characterized by a small mb:Ms ratio relative to most earthquakes, there are exceptions (e.g. Bowers & Selby, 2009; Selby et al., 2012). Strong spatial variations in the amplitudes of surface wave have been observed for nuclear tests in North Korea (e.g., Bonner et al., 2008; Koper et al., 2008; Zhao et al., 2008; Shin et al., 2010). Figure 2-1 presents five Ms measurements observed on real data following a North Korean nuclear test in 2006 to illustrate the variation of observed Ms (measurements are obtained from Michael Pasyanos, personal communication, 2017). It also shows Ms predictions from a numerical simulation through a recent 3D model (Shen et al., 2016). We describe the details of the numerical

simulations in sections 2.3.2-2.3.4. Both the real data and the predictions show a similar pattern of amplification and de-amplification in Ms. One of principal goals of this chapter is to illuminate the physical cause of such amplifications effects.

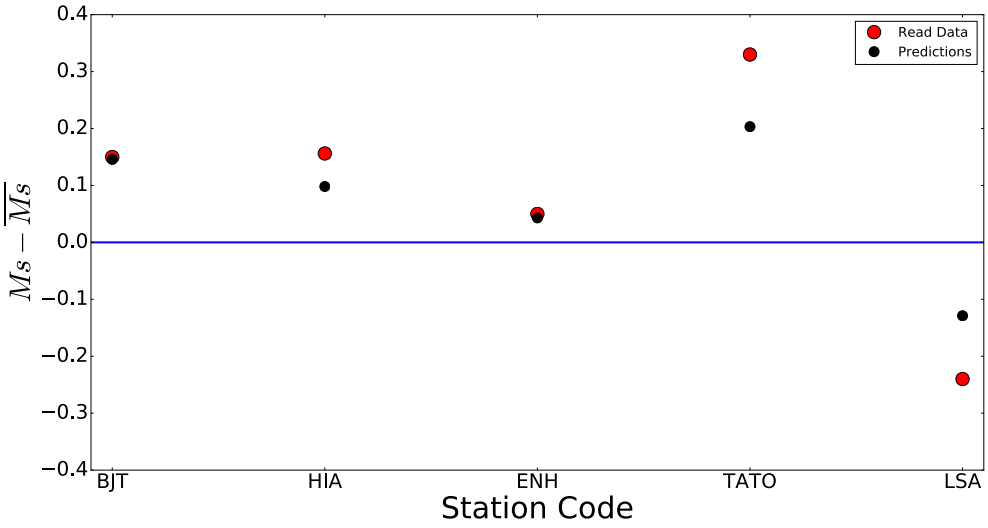

Figure 2-1 Ms measurements using real data.

Illustration of the variations of Ms measurements using real data (red dots, 2006 DPRK nuclear test) compared with Ms predictions based on the China Reference Model (black dots). The measurements are provided by Michael Pasyanos (personal communication, 2017), obtained at the stations indicated on the horizontal axis. The data shown are differences relative to the average Ms of each dataset, which is 3.1 for the real data and 3.15 for the numerical predictions.

The chapter is organized in three parts. The first part of the chapter illustrates the importance of the impact of elastic heterogeneity on through-passing short period surface waves. It comprises sections 2.3 – 2.5 where we present a 3D wavefield simulation in East Asia (Fig. 2-2), a region chosen because of the presence of significant sedimentary basins, identified by cross-hatching in Figure 2-2 and named in Table 2-1. We describe the Earth model used in the 3D simulations and the corresponding numerical schemes (section 2.3) and present simulated observations of surface wave travel times and amplitudes (section 2.4) across East Asia at 10 s period. The final section of the first part illustrates how elastic structure would bias surface wave magnitude (Ms)

measurements when the amplitude effects of elastic heterogeneity are ignored. The 3D wavefield simulations across East Asia are based on the code SES3D, which is a 3D spectral element solver in spherical coordinates (Gokhberg & Fichtner, 2016). One of the features of this code is that it is straightforward to implement arbitrary 3D models.

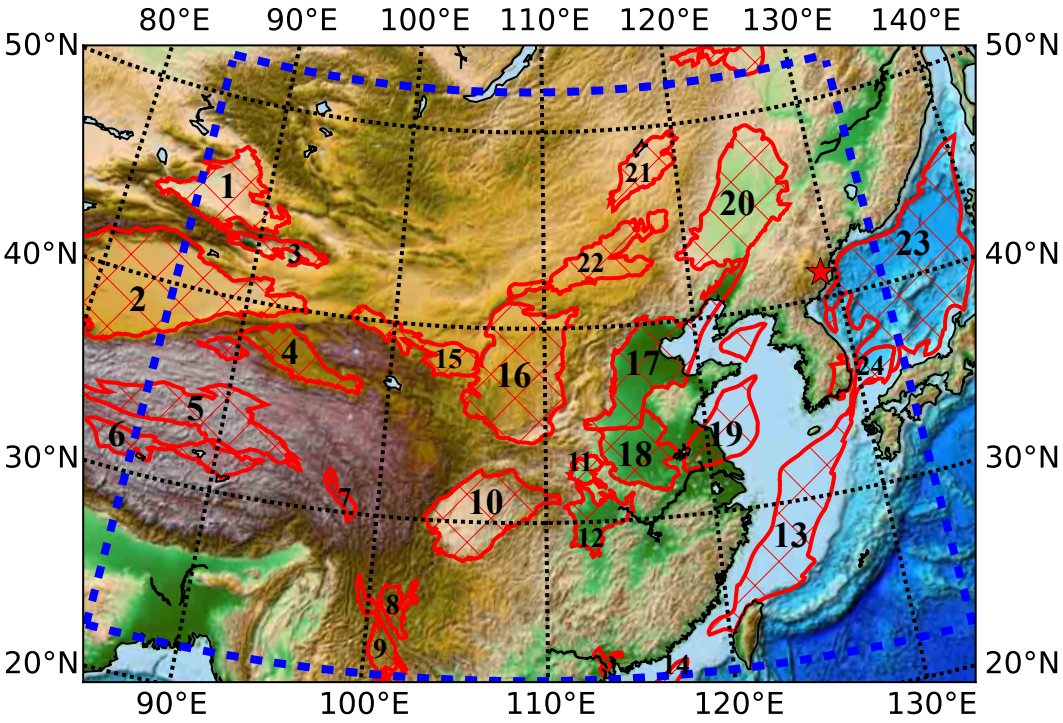

Figure 2-2 Region of Study of East Asia

The blue dashed box encloses the study region in which stippled areas identify the sedimentary basins, which are named in Table 1. The red star is the location of the source for the 3D simulation near the North Korea nuclear test site.

Table 2-1 Major basins in the study region

Zones	Major Basins
Xiyu (Northwestern China)	Junggar Basin (1) Tarim Basin (2) Turpan Basin (3)
Tibetan Plateau and Nearby Areas	Qaidam Basin (4) Qiangtang Tanggula Basin (5) Cuoqing Lunpola Basin (6) Qabdu Basin (7) Chuxiong Basin (8)
Southeastern Tibet	Lanping-Simao Basin (9)
South China	Sichuan Basin (10) Nanyang Basin (11) Jianghan Basin (12) East China Sea Basin (13) Pearl River Mouth Basin (14)
North China Craton and nearby seas	Jiuquan Minle Wuwei Basin (15) Ordos Basin (16) Bohaiwan Basin (17) Taikang Hefei Basin (18) Subei Yellow Sea Basin (19)
Northeastern China, Korean Peninsula, and the Sea of Japan	Songliao Basin (20) Temtsag Hailar Basin (21) Erlian Basin (22) Sea of Japan Backarc Basin (23) Tsushima Basin (24)

The second part of the chapter comprises sections 2.6, which aims to illuminate the physical cause(s) of the surface wave amplitude anomalies across East Asia simulated in the first part of the chapter. The full waveform numerical examples presented in this part of the chapter are carried out using SPECFEM2D (e.g., Komatitch et al., 2001) and SW4 (Petersson & Sjogreen, 2014), which are designed for 2D and 3D wavefield simulations in Cartesian coordinates, respectively. We propose that 2D lateral elastic focusing is the dominant physical cause of amplitude anomalies for short period surface waves propagating in a 3D Earth. This lateral focusing effect includes several principal characteristics that can be observed in both 2D and 3D simulations, which are: (1) retardation of the wavefront inside the basin; (2) deflection of the wave propagation direction; (3) a high amplitude lineation or stripe directly downstream from the basin bracketed by two low amplitude zones; and (4) formation of a secondary wavefront. We also quantitatively show that most of the wavefield effects observed in the 3D simulations can be reproduced quite accurately with horizontal 2D membrane wave simulations.

Section 2.7 is the third part of the chapter in which we discuss how surface wave focusing depends on the scale and geometry of the basin and compare the effects of anelastic attenuation with elastic focusing. We show that on a regional scale elastic focusing through sedimentary basins is more likely to cause significant surface wave amplitude anomalies than anelastic attenuation produced by the basins.

2.3 Numerical Schemes for the Simulation across East Asia

We describe here the numerical setups for the 3D simulation across East Asia, which include descriptions of the input 3D velocity model, the Q model, surface topography, the source parameters, and the numerical mesh. The simulation code is SES3D, a 3D seismic wave equation

solver based on the spectral-element method (Gokhberg & Fichtner, 2016). The 3D model is a recent model of the crust and uppermost mantle constructed for China by Shen et al. (2016).

2.3.1 3D Velocity Model

The input Earth model for the full waveform simulation is a recently produced 3D isotropic model of the crust and uppermost mantle beneath China (Shen et al., 2016) developed using Rayleigh wave dispersion measurements (8 – 50 s period) obtained from ambient noise and earthquake tomography. The model is intended as a reference for studies like ours, and the authors refer to it as a "China Reference Model". The model is presented on a 0.5°x0.5° grid and extends from the surface to a depth of 150 km. The authors of the model took care in representing sedimentary basins in which sedimentary structure is summarized with three unknowns at each grid node: sedimentary thickness and the top and bottom shear wave speeds (Vs) in the basin. Vs grows monotonically and linearly with depth in the sediments. The density of the sediments and the crystalline crust are computed from Vs using the scaling relationship of Brocher (2005), whereas Vp/Vs is 2.0 in the sediments and 1.79 in the crystalline crust.

The geographical region of the model is shown in Figure 2-2 by the blue box near whose boundary we place a perfectly matched layer (PML, Berenger, 1994). Similarly, there is a perfectly matched layer at 200 km depth. Because the simulation code, SES3D, does not model seismic wave propagation in water, we replace water layers with sediments but we design the sedimentary structure at each location to fit the observed local surface wave speeds from the study of Shen et al. (2016). The largest impact of this replacement occurs in the Sea of Japan, where water depth is the greatest. Because this results in a physically unrealistic model off the coast, we attempt to confine our simulation to the continent as much as possible. The original China Reference Model

has an irregular shape; therefore, we smoothly extrapolate the edges of the original model to get a "rectangular" model that is acceptable for our simulations.

Figure 2-3 illustrates some of the structural features of the China Reference Model by presenting horizontal slices of Vs at the depths of 3 km, 10 km and 20 km as well as topography on the Moho. The model captures many geological structures of the uppermost crust such as the Songliao Basin, the Bohaiwan Basin, the Sichuan Basin and the Subei Yellow Sea Basin, which are all seen on the 3 km depth slice.

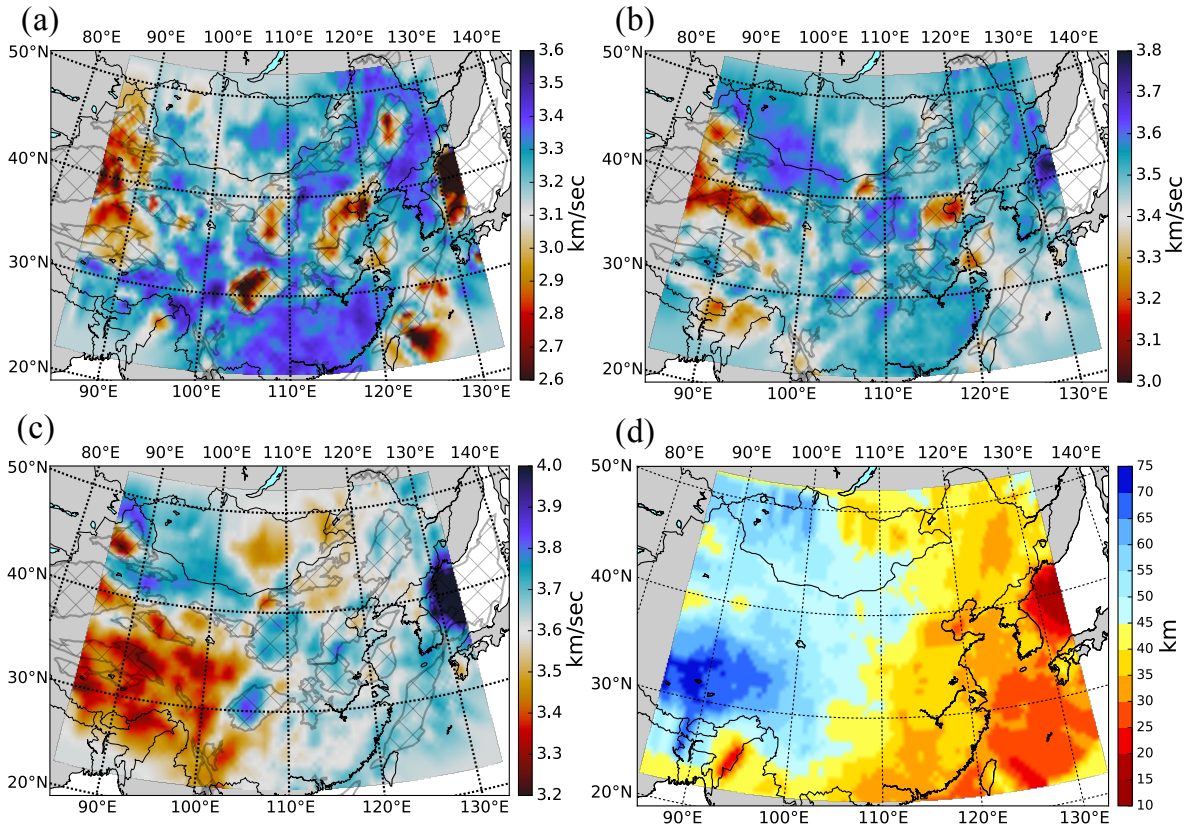

Figure 2-3 Vs Slices of China Reference Model

Horizontal cross-sections from the China Reference Model (Shen et al., 2016) of Vs are presented at depths of (a) 3 km, (b) 10 km, and (c) 20 km as well as (d) crustal thickness. The grey polygons in (a)-(c) indicate major basins in the study region (Table 2-1).

The 3D model is an oversimplification of sedimentary structure, although it fits surface wave phase speeds quite well across our study region. Shen et al. (2016) show that the standard deviation of the misfit to interstation phase time measurements is less than 1 s at most periods. As is common with tomographic models, the amplitude and sharpness of the structural anomalies are probably underestimated, a problem that grows in significance as structures reduce in spatial size. We believe, however, that the model is the best alternative to represent structural effects on surface waves across the study region.

2.3.2 Q Model

For anelasticity, we replace the 3D Q model employed by Shen et al. (2016) with the 1D Q model of Durek & Ekström (1996) because we are primarily interested in the impact of lateral variations in elastic structures on surface waveforms. The visco-elastic relationship is implemented in the simulation using a series of Standard Linear Solids (SLS). We find a set of relaxation times and the corresponding weights using a simulated annealing algorithm (Kirkpatrick et al., 1983), which results in an almost constant Q from about 10 to 20 s period. The result of using a 1D Q model is that all lateral variations in the wavefield will derive exclusively from elastic structure.

2.3.3 Surface Topography

Surface topography is not implemented in the simulation because our interest centers on the impact of elastic velocity heterogeneity within the Earth on short period surface waves. This is also due to the fact that the effect of topography on the 10 s surface waves is believed to be negligible (e.g. Kohler et al., 2012).

2.3.4 Source Parameters

As shown in Figure 2-2 (red star), the seismic source is located on the North Korea nuclear test site with a longitude of 129.1°and latitude of 41.3°. The moment tensor is:

$$\mathbf{M}=\begin{bmatrix} 1.45 & 0 & 0 \\ 0 & 1.45 & 0 \\ 0 & 0 & 1.45 \end{bmatrix}\times 10^{15} N\cdot m \tag{1}$$

which is isotropic to remove the radiation pattern from the wavefield. The source has a moment magnitude Mw = 4.07. We apply a fourth order Butterworth bandpass filter to the Heaviside step function (e.g., eq. (13.22) in Riley et al., 2006) with corner frequencies at $f_{min} = 0.05$ Hz and $f_{max} = 0.1$ Hz to produce the input source time function (Figure 2-4).

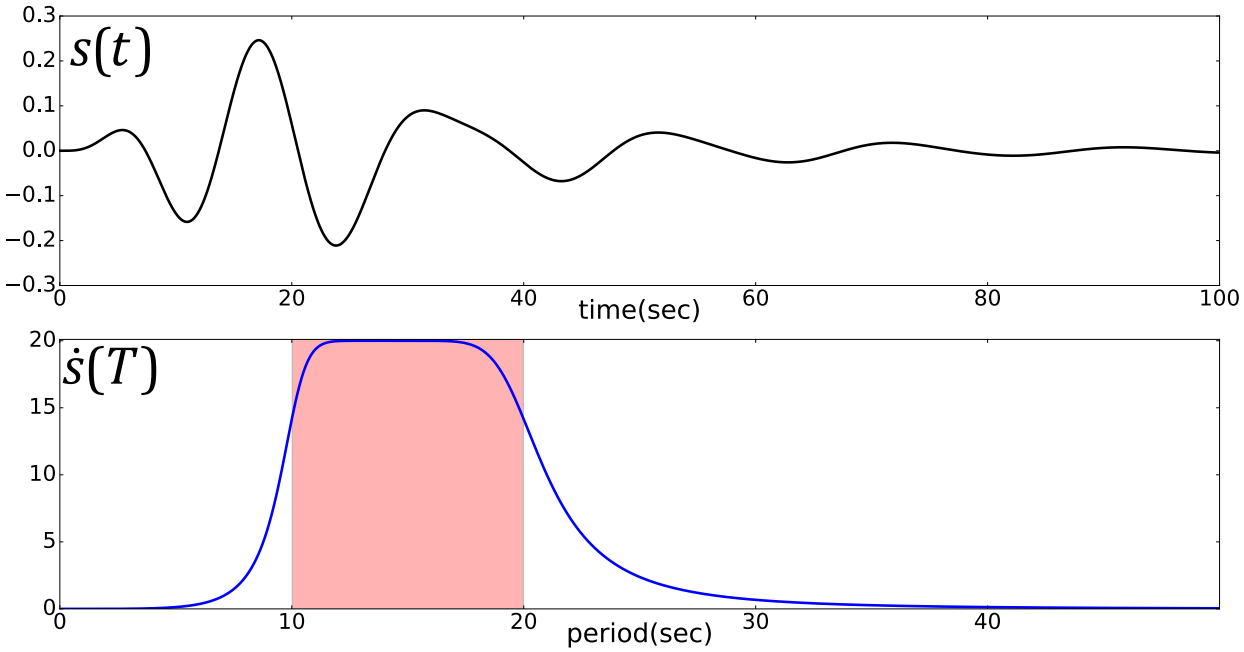

Figure 2-4 Source Time-function

The upper panel is the time series while the lower one is the time derivative of the source time function in the period domain. (Far field displacement is proportional to the derivative of the source time function).

2.3.5 Mesh Setup

Our study focuses on the analysis of the 10 second Rayleigh wave, which can be accurately simulated with a mesh scheme in which the maximum element size is around 6 km. Because each element has 5 cells with nodes located at the Gauss-Lobatto-Legendre points, the maximum grid

spacing is approximately 1.2 km. Because the minimum wavelength in the simulation is 10 km (minimum shear wave velocity is 1 km/s in the model), 8.3 grid points per minimum wavelength is sufficient for our simulation (larger than the 5 grid points per minimum wavelength suggested by Komatitsch & Tromp, 1999, for example).

2.4 Wavefield Analysis

Vertical component wavefield snapshots at times of 120, 460, 700, 1020 s after the initiation of the source are presented in Figure 2-5. The Rayleigh wave dominates these wavefields. A corresponding wavefield animation can be found in the supplementary materials. Wavefront distortions are primarily caused by the sedimentary basins. There are four principal types of distortion. (1) The wavefront is retarded and buckles inward during propagation through a basin (e.g., 460 s snapshot, Fig. 2-5b). (2) The wavefield propagation direction is deflected. (3) After the wavefront emerges from a basin it amplifies, and there is attendant de-amplification that brackets the region of strong amplification. (4) The basins generate a secondary wavefront with a smaller radius of curvature that trails the primary wavefront (e.g, 700 s inset, Fig 2-5c). Note that the de-amplification is harder to observe in the 3D wavefield simulation through the China Reference Model, but we attempt to clarify it in the simulations through idealized structures presented later in the chapter. The basin that has the largest impact on the wavefield is the Bohaiwan Basin.

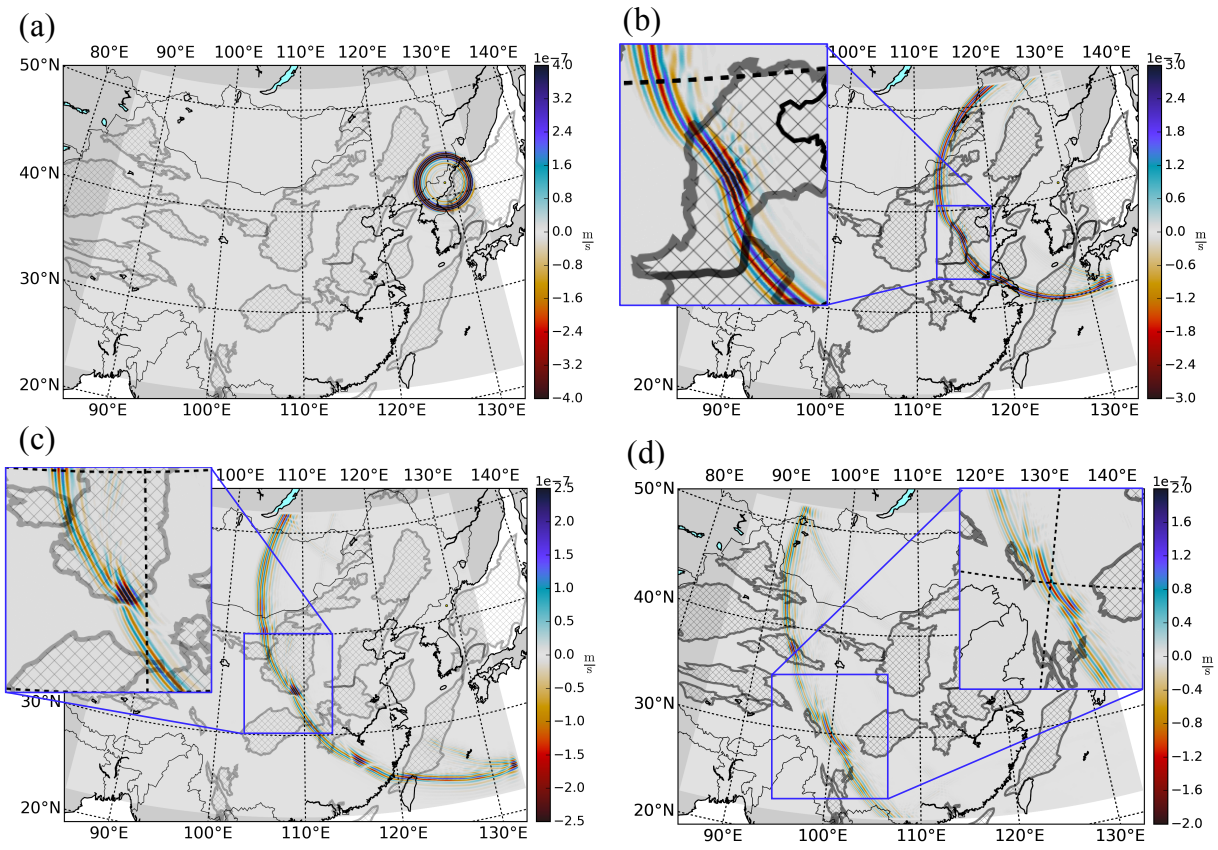

Figure 2-5 Wavefield Snapshots

Wavefield snapshots at times t = 120, 460, 700, 1020 s. (a) At t = 120 s, the wavefront is still approximately circular. (b) At t = 460 s, the wavefront is traveling through the Bohaiwan and Subei basins and has been greatly distorted. (c) At t = 700 s, a secondary wavefront has been generated where amplification occurs, shown in the inset. (d) At t =1020 s, the Sichuan basin's impact on the wavefront is apparent.

Given the synthetic seismograms from the simulation, we measure the dispersion curves for phase velocity and spectral amplitudes to determine the travel time (Fig. 2-6a) and amplitude maps (Fig. 2-6b). We make these measurements using frequency-time analysis (FTAN, Levshin et al., 1972; Levshin & Ritzwoller, 2001). Although the simulation is for the band between 10 and 20 s period, we concentrate interpretation at 10 s period because the impact from sedimentary basins is stronger

at the shorter period end of our bandwidth of study. Large amplitude stripes appear (Fig. 2-6b) where the travel time level lines cave inward (Fig. 2-6a).

We can determine the apparent propagation direction at each grid point using the eikonal equation:

$$\frac{\mathbf{k}}{c(\mathbf{r})} = \nabla\tau(\mathbf{r}) \qquad (2)$$

where the left hand side is the unit wavenumber vector located at position r divided by the corresponding phase speed and the right hand side is the gradient of the local travel time. Thus, the local direction of the gradient of the travel time field gives the apparent propagation direction. The angular difference between the propagation direction and the great circle path, which reflects the local deflection of the propagation direction, is presented in Figure 2-6c. As discussed further in section 2.6, the propagation deflections bracket the amplification stripes in Figure 2-6b.

For comparison, we also present in Figure 2-6d the direction of propagation and deviation from the great-circle path using travel times computed by 2D ray tracing on a sphere followed by the application of the eikonal equation. This is computed using the phase speed map in Figure 2-6e from the China Reference Model. Ray tracing is performed with the fast-marching method (FMM) of Rawlinson & Sambridge (2004) for the 10 s Rayleigh wave. We also discuss this result in section 2.6.

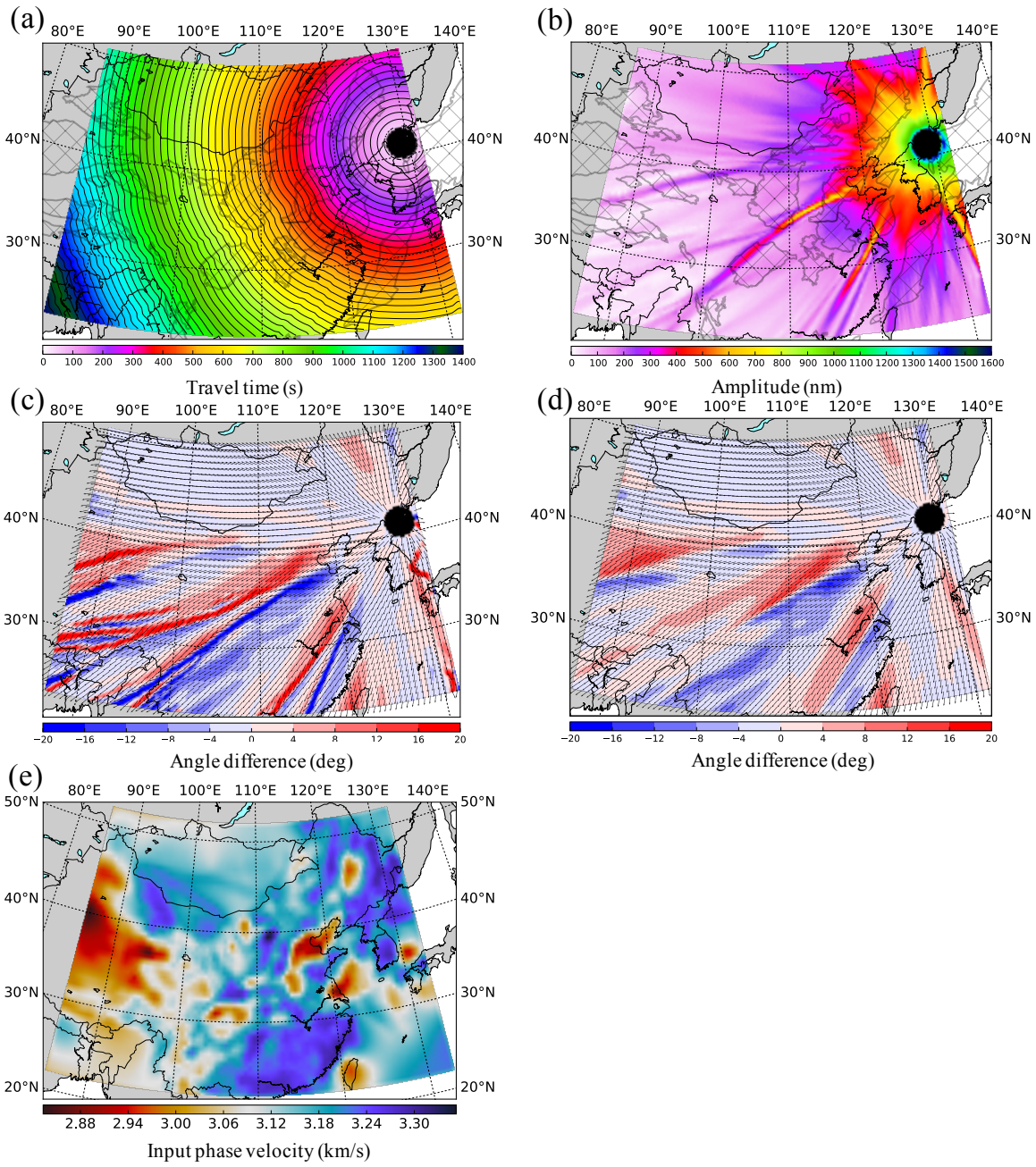

Figure 2-6 Rayleigh Wave Measurements

Plots of 10 s Rayleigh wave measurements in the 3D simulation through the China Reference Model of (a) travel time, (b) amplitude, and (c) angular difference between the propagation direction and the local great circle direction. (The angle is defined in polar coordinates with the axis pointing to the East, counterclockwise direction is positive.) (d) Angular difference between 2D ray tracing propagation direction and the local great circle direction. (e) Input phase velocity map (10 s Rayleigh wave) for the ray tracing computation in (d).

2.5 Bias of Surface Wave Magnitudes Due to Elastic Propagation Effects

As discussed earlier, reliable surface wave magnitude (Ms) measurements are needed to help discriminate nuclear explosions from earthquakes because many explosions are characterized by a small mb:Ms ratio relative to most earthquakes (e.g. Bonner et al., 2008; Bowers & Selby, 2009). Here, we illustrate how large of a bias can be introduced in the Ms measurement unless 3D propagation effects through sedimentary basins are taken into account.

We apply Russell's empirical formula (Russell, 2006) to measure Ms in our simulations, which is defined as follows:

$$M_s = \log(a_b) + \frac{1}{2}\log(\sin(\Delta)) + 0.0031\left(\frac{20}{T}\right)^{1.8}\Delta - 0.66\log\left(\frac{20}{T}\right) - \log(f_c) - 0.43 \qquad (3)$$

where T is period, f_c is the corner frequency controlled by the period and the epicentral distance Δ (in degree). a_b is the measured amplitude filtered with a bandwidth [1/T-f_c, 1/T+f_c]. The formula is designed to correct the amplitude measurements empirically for geometrical spreading, anelastic attenuation and surface wave dispersion. We first use this formula to measure Ms based on simulation through the laterally homogeneous model ak135 (Kennett et al., 1995) using the same source we applied to the 3D simulation. At an epicentral distance of $\Delta = 20°$, at 10 s period, we find Ms = 3.2. This value of Ms serves as the 1D reference for the analysis of the 3D synthetic data through the China Reference Model.

Figure 2-7 presents the resulting Ms measurements through the China Reference Model at 10 s period, which vary from 2.5 to 3.9 across the study region. The range of variation is similar to measurements made on real data across the region (e.g., Michael Pasyanos, personal communication, 2017), a subset of which are shown in Figure 2-1. The five Ms measurements from real data (2006 DPRK Nuclear Test) shown in Figure 2-1 are presented with triangles in Figure 2-7. The color inside the triangles indicates the Ms measurement from real data. We

discarded Ms estimates from stations that have an epicentral distance $\Delta < 500$ km, which may suffer from near-field complications of the wavefield. The five real Ms measurements indeed show amplification and de-amplification in accord with predictions. Further data analysis, which is beyond the scope of this chapter, is called for in the future to investigate this comparison further.

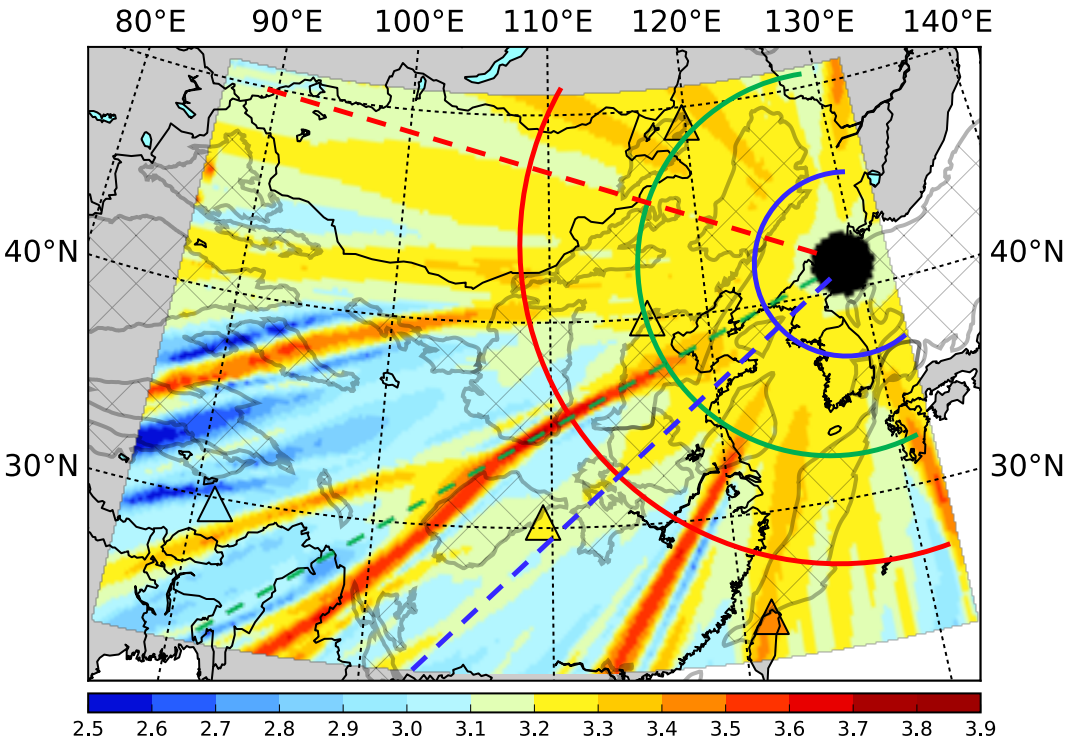

Figure 2-7 Surface Wave Magnitude Map

Computed using Russell's formula (Russell, 2006) from the amplitude map (Fig. 2-6b) taken from the 3D simulation through the China Reference Model. The color of the triangles indicates Ms measurements extracted from real data (2006 DPRK Nuclear Test, Michael Pasyanos, personal communication, 2017). For comparison, as in Fig. 1, the mean of the measurements has been shifted to the mean of the predictions. The colored solid and dashed lines mark locations for the azimuthal and distance dependent curves shown in Fig. 2-8.

Because the reference Ms = 3.2, we consider Ms estimates that fall in the range from 3.1 to 3.3 as unaffected by elastic amplification or de-amplification. More than one third of the region has measurements that are biased outside this range. The Ms map clearly illustrates attendant de-

amplification zones that bracket the stripes of strong amplification. We discuss this effect further in section 2.6.

Figure 2-8 illustrates the variation of measurements of surface wave amplitude and Ms with azimuth and distance. The selected grid nodes for Figure 2-8 are identified with bold color-coded lines in Figure 2-7. Assessment of azimuth variation is based on three groups of grid nodes at different distances (distance ~ 500 km, 1100 km, 1700 km) and is shown in Figure 2-8a and c. For a distance of about 500 km (blue dots), amplitude measurements display very little azimuthal variation and Ms estimates are approximately constant. However, for a distance of about 1100 km (green dots), the measurements oscillate with azimuth and display several peaks or troughs due to amplification and de-amplification. At greater distances (~ 1700 km, red dots), the peaks corresponding to the amplifications become narrower with larger variations in both amplitude and Ms. To illustrate the variation with distance, we also group our measurements in three azimuth ranges in Figures 2-8b and 2-8d at azimuths of 235°-236° (blue dots), 253°-254° (green dots), and 300°-301° (red dots), respectively. The 253°-254° azimuth range has the largest amplification effect, while the 235°-236° range is expected to be de-amplified as it is between two amplification stripes. The 300°-301° range has neither amplification nor de-amplification. Two of these groups of measurements (235°-236° and 300°-301°) display a clear decay of amplitudes with distance while for the other azimuth range (235°-236°) amplitudes tend to be systematically smaller than the other groups at distances larger than 1500 km. The Ms measurements in the two groups of measurements shown in Figure 2-8 illustrate how Russell's empirical formula does not account for the amplitude variation in a 3D Earth model.

In summary, elastic structures in sedimentary basins strongly impact both surface wave amplitudes and Ms estimates of regionally propagating surface waves at 10 s period. Amplitudes may be

several times larger and the Ms variation can be as large as 1.4 magnitude units across East Asia for events on the North Korea nuclear test site.

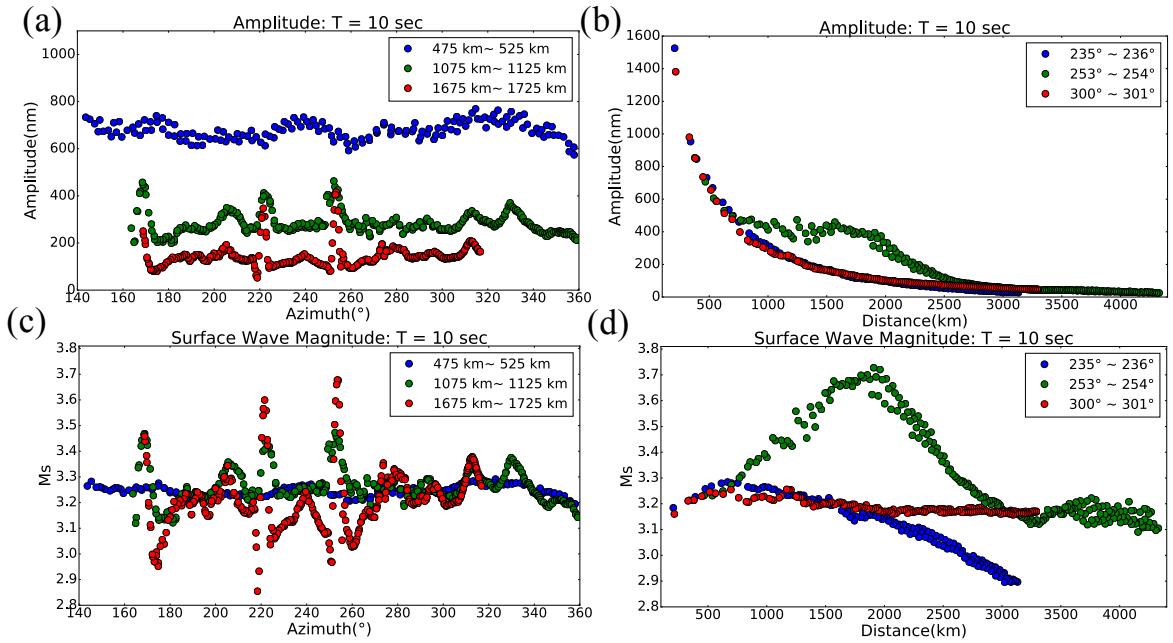

Figure 2-8 Rayleigh Wave amplitude and Ms

Detailed plots of the 10 s Rayleigh wave amplitude and Ms as a function of distance and azimuth from the 3D wavefield simulation through the China Reference Model. Locations of the points on these plots are presented in Fig. 2-7 where those lines are colored coded as the symbols in this figure. (a) and (b) are the amplitude measurements while (c) and (d) are the Ms estimates. The full amplitude field across the study region is shown in Fig. 2-6b and the Ms across the region is shown in Fig. 2-7. Ms ~ 3.2 for a laterally homogeneous model.

2.6 The Physical Cause of Surface Wave Amplification/De-Amplification – 2D Lateral Focusing/Defocusing

In this section, we propose a physical mechanism to explain the amplitude effect that we observe in the 3D simulation. If we take a closer look at the wavefield snapshot (t = 730 s) shown in Figure 2-5c, large amplification occurs where the wavefront travels through the Bohaiwan Basin. We also notice that a secondary wavefront (a wavefront with larger curvature compared with the major one) is generated at the amplification location. Because of this, we hypothesize that the amplitude anomalies observed from the 3D simulation across East Asia are predominantly caused by 2D focusing due to lateral heterogeneity, rather than more complicated 3D effects that may include vertical scattering and mode mixing.

2.6.1 2D Focusing Effect

The 2D focusing effect proposed here is fundamentally a wavefront deflection phenomenon due to the impact of a lateral velocity heterogeneity. Figure 2-9 illustrates the principal characteristics of the 2D focusing effect, depicting the effect of a low velocity anomaly on a surface wavefield. When the wavefront propagates through the anomaly, we would observe:

(1) The formation of a wavefield concavity inside the velocity anomaly.

(2) The deflection of wave propagation direction, which indicates the bending of the wavefield energy flux.

(3) A high amplitude lineation or stripe directly downstream of the anomaly bracketed by two low amplitude zones. This is due to the fact that the wavefield energy off center-axis flows into the center and is fundamentally a consequence of conservation of energy.

(4) A secondary wavefront with a smaller radius of curvature than the primary wavefront outside the velocity anomaly, which is radiated from the focal point where the energy converges.

If true, these principal characteristics should be observed in both 2D and 3D wavefield simulations. Because we propose that 2D focusing/defocusing dominates the amplitude effect downstream from sedimentary basins for surface waves propagating in a 3D Earth, we also need to evaluate quantitatively the consistency between the 2D and 3D amplitude predictions. In the following sections, we verify these characteristics of the wavefield that are needed to support the hypothesis that 2D focusing dominates the amplitude effect for surface waves propagating in a 3D Earth.

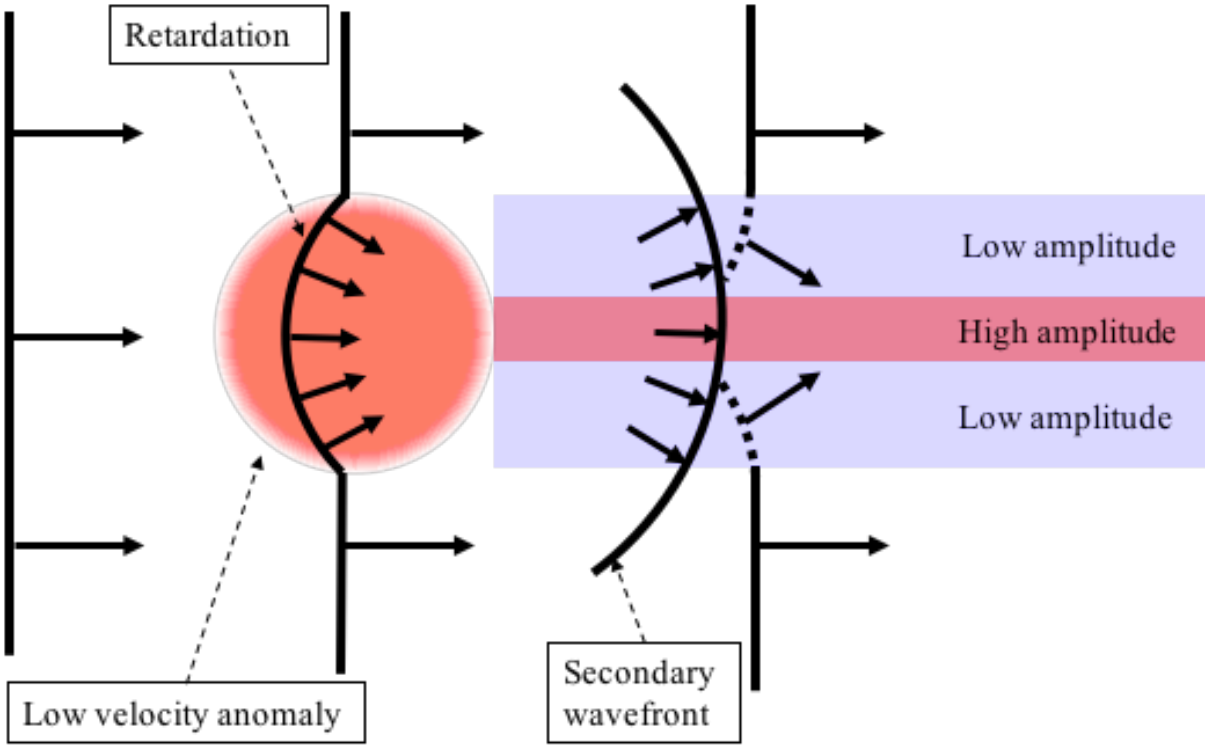

Figure 2-9 Elastic Focusing Effect

Cartoon summarizing some of the principal wavefront characteristics in our 3D simulations including the formation of a concavity inside the low velocity anomaly, the formation of a secondary wavefront with a smaller radius of curvature than the primary wavefront, the bending of the primary wavefront as it adheres to the secondary wavefront (dashed lines), and amplification and de-amplification downstream from the velocity anomaly. Wavefronts are shown with solid lines and the normals to them are shown with arrows, which represent local wavefield propagation directions.

2.6.2 Wavefront Bending and Amplification

We begin with a 2D membrane wave simulation to investigate the distortion of a wavefront propagating downstream from a circular low velocity anomaly, with particular concentration on the direction of propagation of the wavefield. Figure 2-10 presents the simulation results using SPECFEM2D (e.g., Komatitch et al., 2001). The source and low velocity anomaly locations are shown in Figure 2-10a. The distance from the center of the anomaly to the source is a little less than 1000 km. The fractional wave speed perturbation of the low velocity anomaly in the "basin" is given by:

$$\frac{\delta\beta}{\beta} = \begin{cases} \frac{\varepsilon}{2}[1+\cos(\pi r / R)] & r \in [0,R] \\ 0 & r \in (R,\infty) \end{cases} \qquad (4)$$

where $\varepsilon = -10\%$ is the maximum velocity perturbation in the center of the basin, R = 100 km is the radius of the low velocity anomaly, and r is the radial distance from the center of the anomaly. Due to the effect of the low velocity anomaly, the travel time contour is distorted (Fig. 2-10b) inside the anomaly and there is an amplification stripe downstream from the low velocity anomaly (Fig. 2-10c). There is also attendant de-amplification that brackets the amplification stripe (white stripes in Fig. 2-10c). The emergence of the de-amplification stripes is consistent with the shape of the cross-section of the amplitude sensitivity kernel (Fig. 2-15b). Using the eikonal equation (eq. 2), the gradient of the travel time map provides the propagation direction of the wavefield. The angular difference between the propagation and the straight ray directions gives the wavefront deflection, as shown in Figure 2-10d. The red and blue stripes, which represent positive and negative deflections, come in pairs that bracket the amplification stripe in Figure 2-10c. This

simple 2D membrane wave simulation shows characteristics (1) - (3) of 2D focusing effect hypothesized in section 2.6.1.

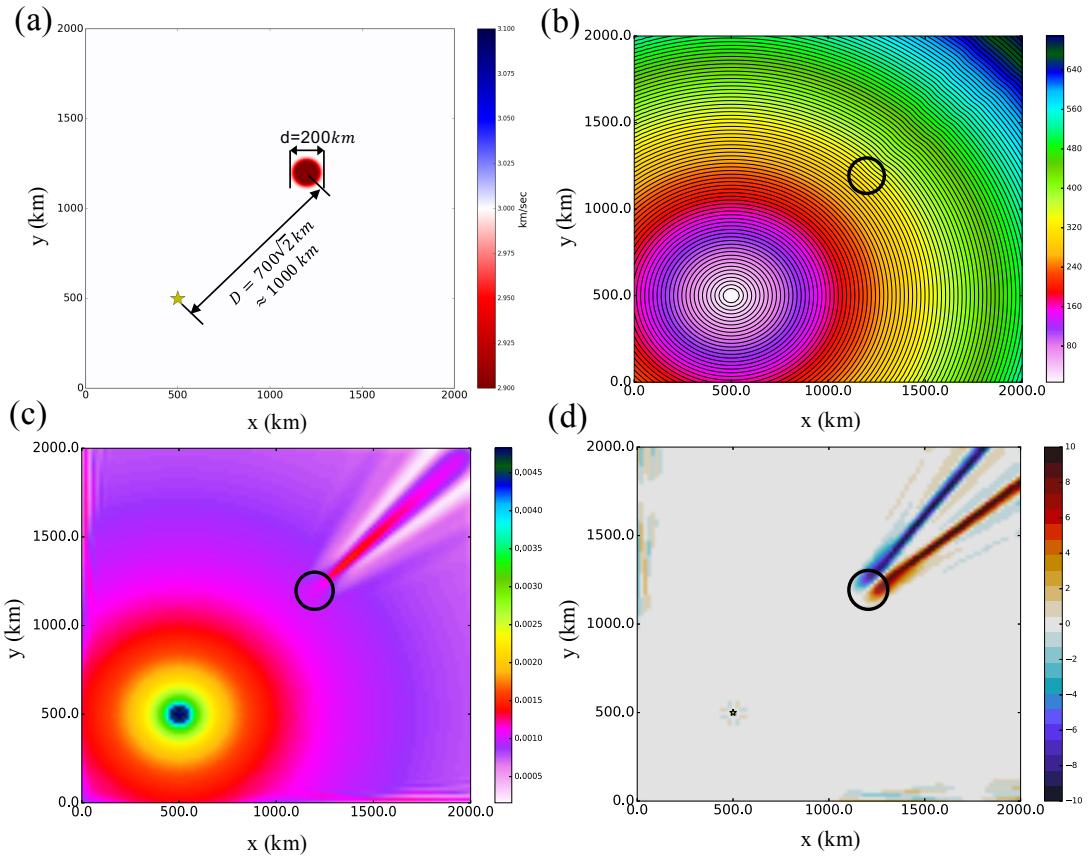

Figure 2-10 Membrane Wave Measurements

A 2D membrane wave simulation to illustrate the impact of a low velocity anomaly on the deflection of the propagation direction. (a) Input velocity model and source location, (b) travel time map, (c) amplitude map, (d) angular difference between the propagation direction and the straight ray path. (The angle is defined in polar coordinates where the axis points to the right and the counterclockwise direction is positive). The impact of a 2D low velocity anomaly or "basin" is to produce a high amplitude streak downstream from the anomaly in (c) which is bracketed by two de-amplification stripes. The amplification stripe is also bracketed by lines of wavefield deflections clockwise (blue) and counterclockwise (red) in (d). This signature of wavefield amplification/de-amplification and deflection is characteristic of surface wave focusing and is also seen in the 3D wavefield simulation (e.g., Fig. 2-6b,c).

These principal characteristics (1)-(3) of 2D focusing are also observed in the 3D simulation across East Asia. Indeed, Figure 2-6a shows the distortion of travel time contour when the wavefield propagates through the Bohaiwan Basin, and the location of the distortion is consistent with the largest amplification stripe in the amplitude map (Fig. 2-6b). As mentioned earlier, the attendant low amplitude zones that brackets the amplification stripe can be identified in Figure 2-7. Also, the propagation deflection map (Fig. 2-6c) computed by using the eikonal equation indicates that all the amplification stripes that emerge in the amplitude map (Fig. 2-6b) are caused by bending and focusing of the energy flux of the wavefield.

For a simple comparison, Figure 2-6d shows the ray tracing result computed using the input phase velocity map presented in Figure 2-6e. The full waveform propagation deflection map (Fig. 2-6c) has more detailed bifurcations and somewhat larger magnitudes of the off-great circle deflection than the ray theoretical propagation deflection map (Fig. 2-6d), which may be due to wavefield scattering.

2.6.3 2D versus 3D Amplitude Predictions

Another piece of evidence we need to provide to support the hypothesis that 2D focusing dominates the amplitude effect for surface waves propagating in the 3D Earth is to quantitatively compare amplitude predictions generated by 2D and 3D simulations.

A complication in comparing 2D and 3D simulations is that overtones are generated in the 3D simulations that are absent in the 2D simulations. To test this effect, we compare amplitudes and group velocities measured through the laterally homogeneous model ak135 (Kennett et al., 1995) using full waveform seismograms (produced by SW4, Petersson & Sjogreen, 2014) and normal mode synthetics that include only the fundamental mode (Herrmann & Ammon, 2002). The source is an explosion at a depth of 1 km. We use frequency-time analysis to measure the group velocity

and the amplitude from the synthetic seismograms as a function of epicentral distance. The amplitude measurements are corrected using a 2D geometrical spreading factor and normalized using:

$$A = \frac{A_{obs}\sqrt{D}}{A_{1000}\sqrt{1000}} \quad (5)$$

where A_{obs} is the observed amplitude, D is the source-receiver distance along the Earth's surface, A_{1000} is the amplitude measured at a distance of 1000 km. As Figure 2-11 shows (red dots), the group velocity and corrected normalized amplitude measurements from the 3D full waveform synthetics display oscillations that decays with distance from the source. In contrast, the fundamental mode measurements are range-independent (black dashes).

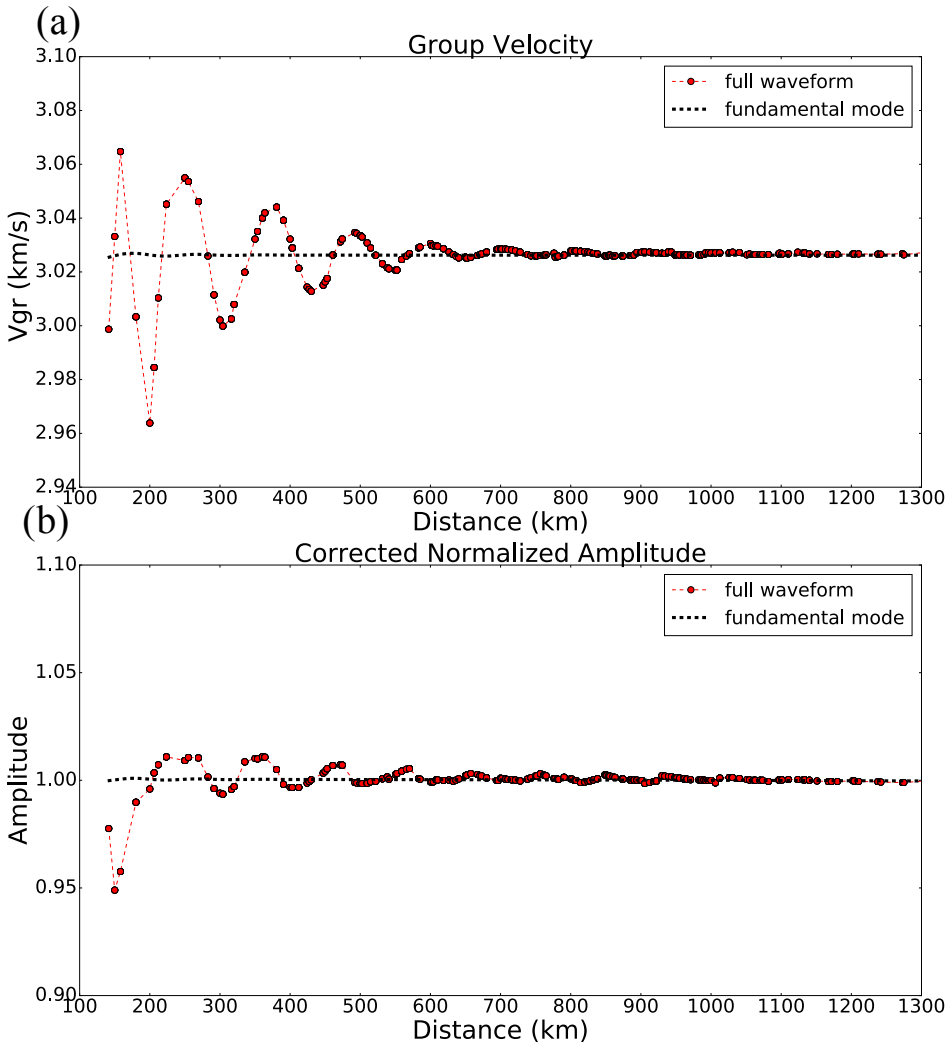

Figure 2-11 Impact of Overtone Interference

Synthetic experiment to test overtone interference on measurements of the fundamental mode in a 3D simulation. Red dots result from a 3D simulation through a laterally homogeneous model whereas the black dashed lines represent fundamental mode synthetic results through the same model. (a) Measured group velocity and (b) corrected normalized amplitude measurements are presented as a function of epicentral distance. Oscillations in the measurements made on the 3D synthetics are caused by overtone interference near the source where the overtones and fundamental mode are not yet separated in time. Amplitude interference decays below about 1% at distances beyond 200 km, whereas group velocity perturbations extend to greater distances.

We conclude that for source-receiver distances greater than about 200 km, overtone interference is weak enough to interpret amplitude measurements made on the fundamental mode. Only at epicentral distances greater than 200 km, therefore, can we compare amplitude measurements obtained on 2D and 3D synthetics.

Figure 2-12 illustrates the input models for the comparison between the 2D and 3D simulations. The input model for the 3D simulation is a rectangular region with dimensions 5000 km × 600 km × 200 km (the green rectangle in Fig. 2-12b), in which an explosive source is located at x = 500 km, y = 300 km, z = 1 km. The velocity structure is ak135 in which a circular sedimentary basin is embedded centered at x = 1500km, y = 300km. The basin has a diameter of 200 km and extends to a depth of 5 km. Shear wave velocity inside the basin increases linearly with depth from 2 km/s at the top (z = 0 km) to 3 km/s at the bottom (z = 5 km) of the basin. Figure 2-12a illustrates the 3D shear wave speed profiles inside and outside the basin.

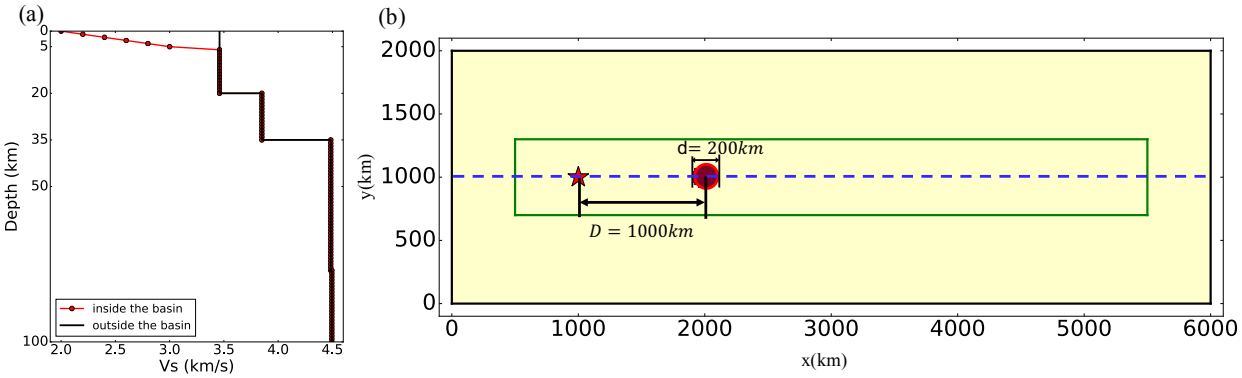

Figure 2-12 Input 2D and 3D Models

Specification of the input 2D and 3D models to test the similarity of wavefield measurements obtained in 2D and 3D simulations. (a) Vertical Vs profile for the 3D input model (red line with dots: inside the basin, black line: outside the basin). (b) Input model geometry for the simulations. The green rectangle is the size of 3D simulation region whereas the black rectangle is the 2D simulation region. The red star is the location of the source. Receivers are aligned on the horizontal blue dashed line.

The 2D model is constructed from the 3D model. In fact, the 2D phase velocity map for the 10 s Rayleigh wave is the input model for the 2D membrane wave simulation. Because the absorbing boundary conditions (Stacey, 1988) implemented in the 2D membrane wave code (SPECFEM2D) do not perform ideally and artificial reflections from the boundaries are generated, the 2D simulation region is larger than the 3D case. As shown in Figure 2-12b, the green rectangle represents the size of the 3D simulation region while the black one illustrates the size of the 2D modeling region.

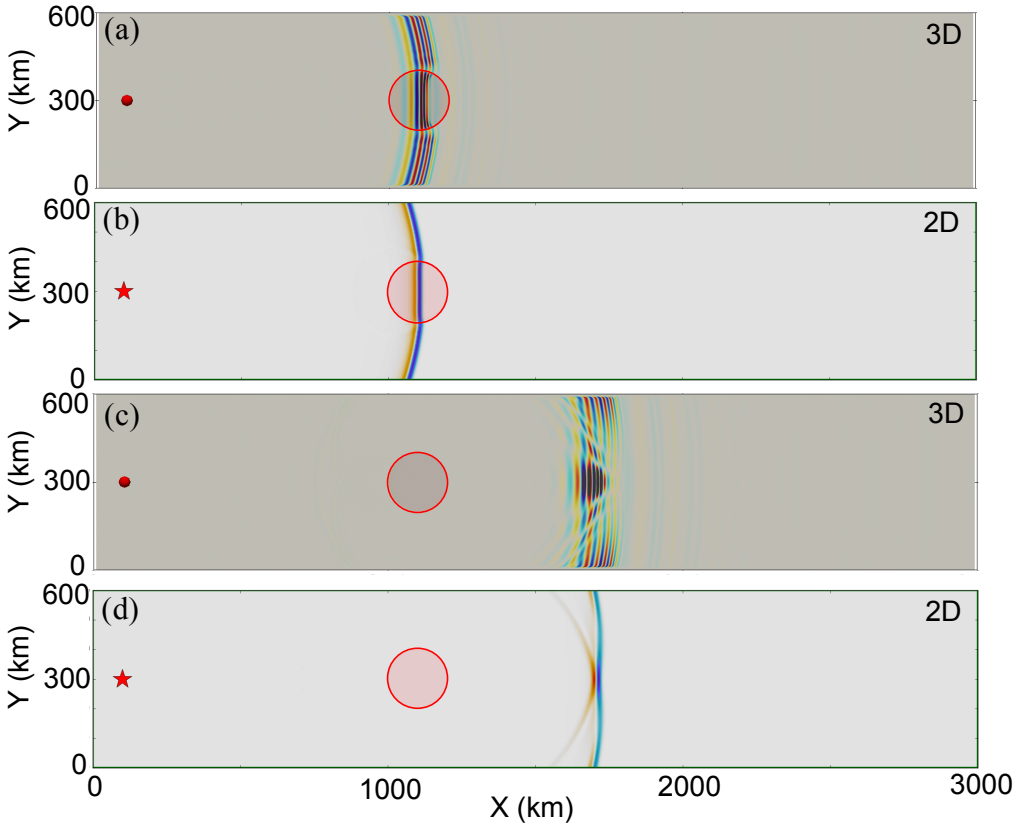

Figure 2-13 Wavefield Snapshot of 2D and 3D Modeling

Wavefield snapshots extracted from the 3D and 2D simulations through a circular low velocity anomaly or "basin" for the simulation geometries shown in Fig. 2-12. (a, b) Distortion of wavefront inside the basin for the 3D and 2D cases, respectively. (c, d) Amplification (focusing) and the generation of a secondary wavefront for the 3D and 2D cases. The 3D wavefield is more protracted in time due to surface wave dispersion.

Figure 2-13 presents wavefield snapshots from the 3D and 2D simulations. The principal difference is that the wavefield in 2D is non-dispersive whereas the wavefront in 3D is dispersed, and is therefore wider. The simulations show several similar qualitative patterns, however. (1) The wavefronts are retarded inside the basin (Fig. 2-13a,b). (2) Downstream from the basin, there is increased amplitude (Fig. 2-13c,d). (3) There is the generation of secondary wavefronts where there is amplification (Fig. 2-13c,d). The secondary wavefront is clearer on the 2D simulation (Fig. 2-13d). In these snapshots, we observe characteristics (1), (3) and (4) of 2D focusing mentioned in section 2.6.1. Together with the facts presented in section 2.6.2, we have observed all four principal characteristics of 2D focusing in both the 2D and 3D simulations.

To perform a quantitative comparison between the 2D and 3D wavefields, we measure spectral amplitudes at 10 s period for the 2D and 3D synthetics and compare them directly in Figure 2-14. The amplitude measurements are normalized to the value observed at 500 km. The red vertical rectangle in the figure indicates the location of the sedimentary basin and the low velocity anomaly. The dominant features of the 2D and 3D results are consistent with each other: they both predict similar amplitude anomalies downstream from the basin, which we conclude is a 2D focusing phenomenon. Both simulations depict amplification inside the basin, although the differences inside the basin are somewhat larger than outside the basin. We also observe an oscillation pattern of the 3D amplitude curve relative to the 2D results, wherever there is an abrupt change in the surface wave eigenfunctions. Consistent with results presented in Figure 2-11, we believe these oscillations are caused by the interference of multimode surface waves in the 3D simulation, which are not simulated in the 2D computation. The results in Figure 2-14 also imply that, for the 10 s Rayleigh wave (vertical component), amplification caused by focusing is much larger than the site response inside basin. This is consistent with Bowden & Tsai (2017), who investigated the site

amplification effect inside sedimentary basins both analytically and numerically. Their results show that site amplification is small for the 10 s Rayleigh wave (vertical component).

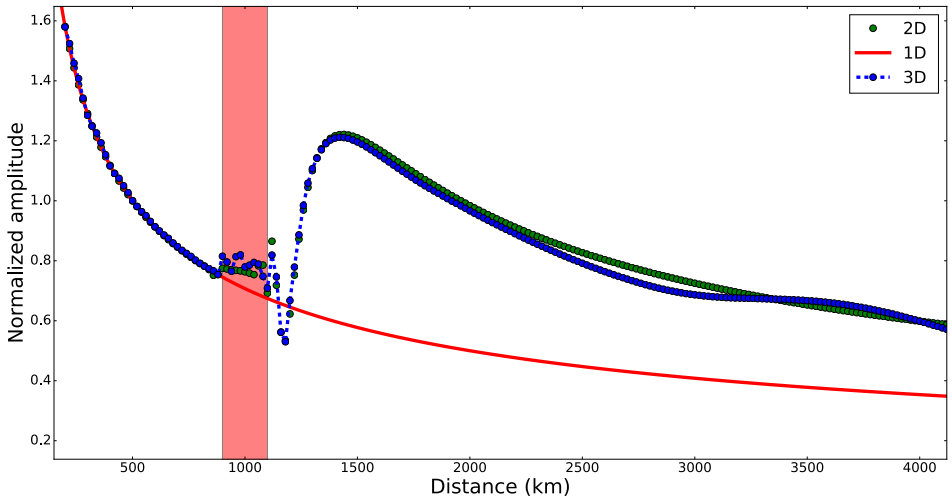

Figure 2-14 2D v.s. 3D Amplitudes

Normalized amplitudes obtained at 10 s period from the 2D and 3D simulations (green dots: 2D amplitudes, blue dots with dashed line: 3D amplitudes, red line: 1D (horizontally homogeneous) amplitudes). The simulation geometries for the 2D and 3D cases are shown in Fig. 2-12 and wavefield snapshots in Fig. 2-13. The colored box indicates the distance range of the low velocity "basin".

In summary, we first hypothesize that 2D focusing dominantly governs the amplitude of surface waves propagating in a 3D Earth, and then we use a variety of 2D and 3D simulation results to test the hypothesis. This conclusion is significant because it implies that the dominant residual effect of sedimentary basins on through-passing surface wave is not a complicated 3D phenomenon as some researchers may suggest. The conclusion also means that phase velocity maps can be used to make amplitude predictions. This is not only computationally much faster, but phase velocity maps are a more direct observable than 3D models, which are inferred from phase velocity maps and perhaps other data. Also, accurate 3D simulations of short period seismic waves through water

layers (e.g., Japan Sea) are challenging (e.g. Komatitsch et al., 2000), but can be circumvented with 2D membrane wave modeling.

2.7 Further Discussion of Elastic Focusing

Here we discuss other issues related to the elastic focusing of surface waves, which include: Does the focusing effect diminish with distance? How does the scale and geometry (e.g., aspect ratio) of sedimentary basins affect focusing? Compared with anelastic attenuation, does focusing have a larger impact on amplitude?

2.7.1 Wavefront Healing

The simulation results presented in Figure 2-14 show decay of the surface wave amplification downstream from the anomaly. This decay results from wavefront healing (e.g., Nolet & Dahlen, 2000), which is a diffraction phenomenon consistent with Huygens' principle that causes wavefront distortion and amplification to decay with distance downstream from the basin. In contrast with body waves (Marquering et al, 1999), where the travel time perturbation asymptotically approaches zero at large propagation distances, surface waves undergo only incomplete healing of both travel time and amplitude perturbations irrespective of the epicentral distance. This phenomenon is reflected in 2D surface wave sensitivity kernels, which do not go to zero at the center of the kernel (Fig. 2-15) unlike the 3D body wave travel time kernel.

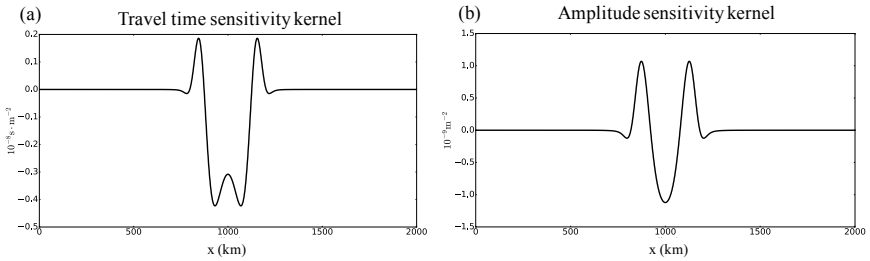

Figure 2-15 Cross-sections of 2D surface wave sensitivity kernels

Shown to illuminate wavefront healing. (a) Cross-section of the travel time kernel, (b) cross-section of the amplitude kernel. (Sensitivity kernels are not used in any of the quantitative analysis presented here).

2.7.2 Effects of Basin Size/Geometry on Surface Wave Focusing

2.7.2.1 Effect of Basin Size

Surface wave focusing depends on the size of basin (low velocity anomaly). To illustrate this, we present several 2D membrane wave simulations with circular anomalies of different diameters. In the numerical scheme the distance from the source to the center of the circular velocity anomaly is 3000 km. The fractional wave speed perturbation of the anomaly is given by equation (4) with $\varepsilon = -10\%$. We vary the radius of the anomaly, which is R in equation (4), incrementally from 100 km to 400 km in the different simulations.

The amplitude curves for different simulations are presented in Figure 2-16a from which we draw two conclusions.

(1) The maximum amplitude downstream from the basin increases as the size of the basin grows. When the size of the basin increases, the primary wavefield out-distances the secondary wavefield by a larger amount than for a smaller basin, which increases the curvature of the diffracted part of the wavefield and increases the amplitude. This is summarized in Figure 2-16b, which shows both the increase in the maximum amplitude with the size of the basin and the increase in the maximum ratio between the observed amplitude and the amplitude of the wavefield without the basin, which we call the maximum amplitude ratio. The maximum amplitude increases sub-linearly with the size of the basin, whereas the maximum amplitude ratio changes more linearly with the size of the basin.

(2) The location of the maximum amplitude also changes with basin radius. If the incoming wavefront were perfectly planar, the location of the maximum amplitude would be the focal point. However, the incoming wavefront is only approximately planar. To estimate the focal length of the velocity anomaly for the non-planar incoming wavefront, we use the thin lens equation. If we define the image distance (d_i) as the distance from the center of the velocity anomaly to the

location of the maximum amplitude, we can approximately determine the focal length using the thin lens formula:

$$\frac{1}{d_i}+\frac{1}{d_o}=\frac{1}{f} \quad (6)$$

where $d_o = 3000\ km$ is the object distance from the source to the center of the basin, and f is the focal length to be computed. Figure 2-16c shows that the focal length defined in this way increases approximately linearly with the radius of the basin (blue dots: computed focal length from eq. (6); black line: linear regression curve). This analysis is only approximately valid, because a circular low velocity anomaly is not an ideal thin lens and it is not expected to have a single focus. Also, the lens equation is ray theoretical, which may be inappropriate in the presence of strong diffraction as exists in these simulations.

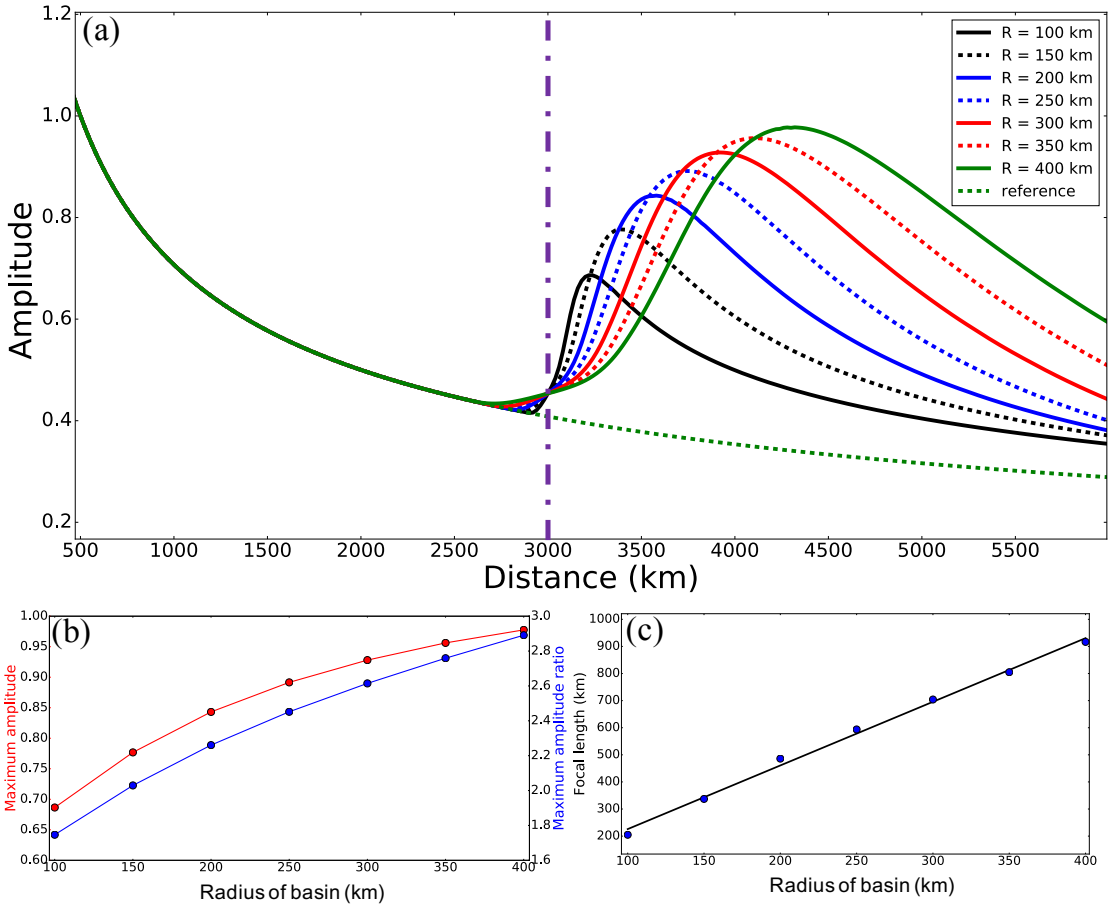

Figure 2-16 Impact of Size of Basins

(a) Amplitude measurements from 2D simulations through circular low velocity anomalies or "basins" with radii ranging from 100 to 400 km. (b) The maximum amplitude and maximum amplitude ratio plotted as a function of the radius of the basin. Amplitude ratio is the amplitude in the simulation with the basin divided by the amplitude in the laterally homogeneous model. (c) The focal length is computed using equation (6). The blue dots are the computed values and the black curve is the linear regression curve.

2.7.2.2 Effect of Basin Shape

We now discuss the effect of the shape of the basin on surface wave amplitudes by presenting two examples. Figure 2-17 shows surface wave amplitudes measured in a 2D membrane wave simulation through a rectangular low velocity anomaly centered 1000 km from the source. The aspect ratio of the velocity anomaly is extremely small; i.e., the long direction of the anomaly

(perpendicular to the direction of propagation) is much greater than the short direction (along the direction of propagation). In this case, there is almost no amplification downstream from the basin, as shown in Figure 2-17b, although there is amplification inside the basin, which is caused by the stacking up of the waves as they slow down. Amplification caused by focusing is due to the bending of the wavefront, but when a plane wave hits an anomaly that is very long in the direction transverse to the propagation direction, the wavefront will not bend, which is why there is little focusing.

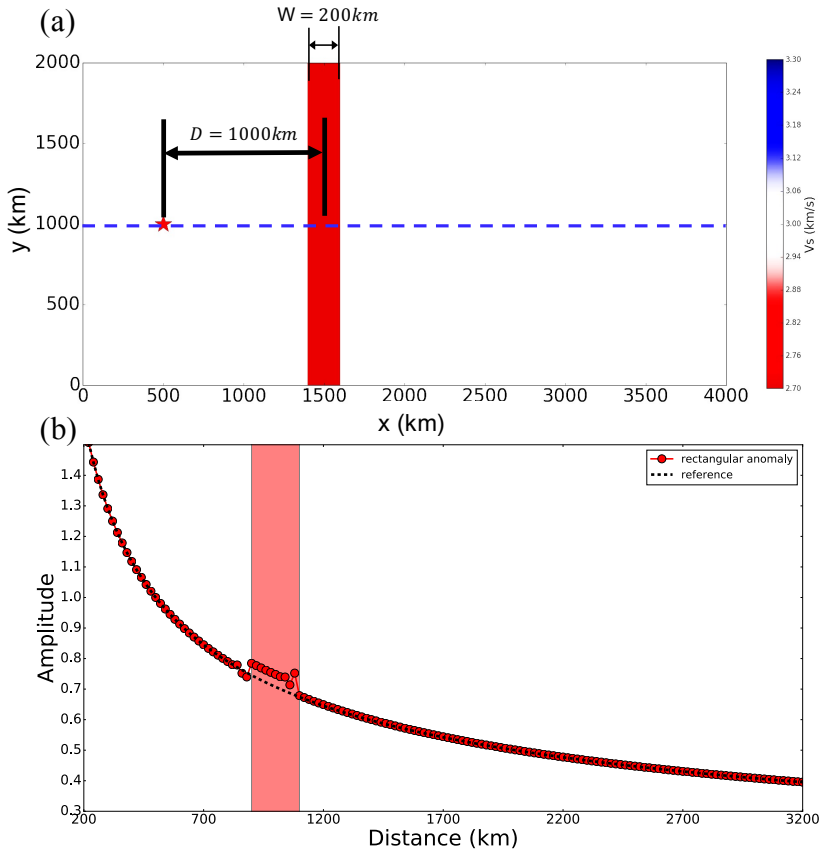

Figure 2-17 Impact of the Shape of Basins

The first 2D membrane wave simulation to contrast with Fig. 2-16 to illustrate the importance of the shape of the velocity anomaly or "basin". (a) Source location (red star) and position of the basin (red rectangle with the long axis in the vertical direction, normal to the long axis in the wave propagation direction). The receivers are aligned along the blue dashed line. (b) The amplitude measurements obtained through the basin in (a).

Figure 2-18 shows another example of a 2D membrane wave simulation through an elliptical velocity anomaly with an aspect ratio of 2. As illustrated by the blue curve in Figure 2-18b, amplitudes increase dramatically as the wavefield travels through the low velocity basin, but then decrease to be even smaller than the reference amplitude curve (amplitude predictions in a horizontally homogeneous media). The synthetic seismograms illuminate the cause of the amplitude decrease in Figure 2-18b. Figure 2-19c presents the synthetic seismogram at a source-receiver distance of 4000 km, where the measured amplitude is smaller than the reference value (shown in Fig. 2-18b). Figure 2-19a is the synthetic seismogram that serves as a reference; it is extracted at the distance of 1000 km, which is not yet affected by the elliptical anomaly. We notice two important characteristics from Figure 2-19. (1) The phase of the two wave packets in Figure 2-19c implies their origins. The primary waveform (shown in blue) is similar to the waveform in Figure 2-19a, while the secondary waveform (shown in red) has similar shape as the wave packet in Figure 2-19b, which is an inverse Hilbert transformed version of Figure 2-19a. Therefore, we conclude that the primary wavefront is generated by wavefront healing while the $\pi/2$ advance of the secondary wavefront indicates that it travels through a caustic. The $\pi/2$ phase shift through caustics is consistent with WKBJ theory (p463, Dahlen & Tromp, 1998). (2) Because the seismogram shown in Figure 2-19c consists of two wave packets, wavefield energy is separated into two parts. This explains why the amplitude curve in Figure 2-18b changes from enhanced amplitudes to reduced amplitudes as distance increases. In this case, amplitude measured on the primary waveform does not characterize the wavefield energy accurately. Indeed, as shown in Figure 2-20a, downstream from the velocity anomaly, the central stripe shows amplification at smaller distance but quickly becomes a low amplitude zone for larger distances. A more accurate measurement of amplitude that depicts the full waveform energy would be given by:

$$A = \frac{1}{N}\sqrt{\sum_{i=0}^{N} a^2(t_i)} \tag{7}$$

where $a(t_i)$ is the envelope of the seismogram at the time t_i, N is the total length of the seismogram. Figure 2-20b shows the amplitude map measured using eq. (7) in which the central amplification stripe downstream from the anomaly behaves normally. In reality, however, measuring a quantity that accurately depicts wavefield energy can be very challenging if there are two separated wavefronts. This is because this waveform separation behaves differently for different surface waves with different periods. Conventional methods that make amplitude measurement, like FTAN, may yield biased results in this situation.

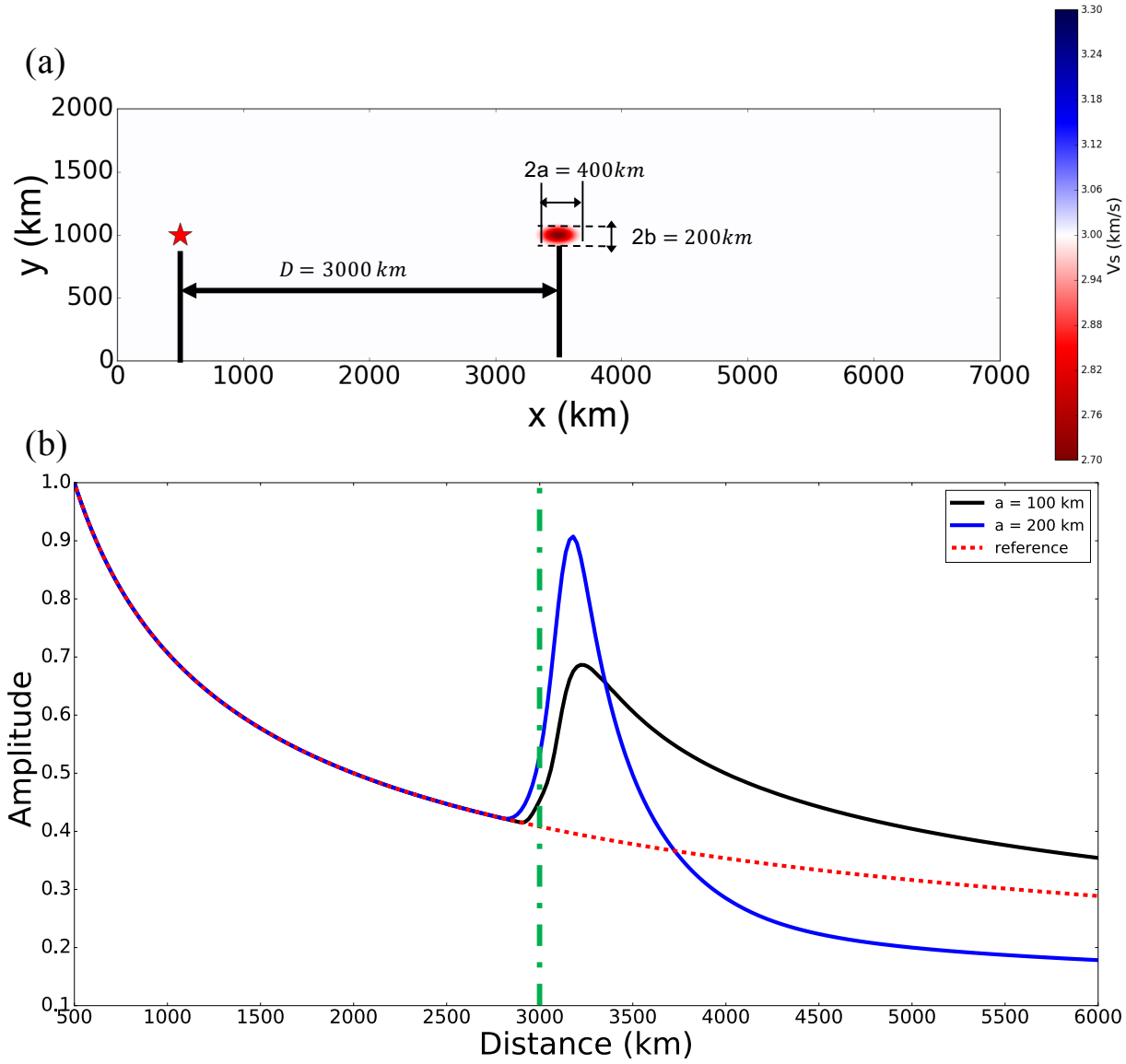

Figure 2-18 Impact of the Aspect Ratio of Basins

The second 2D membrane wave simulation to contrast with Fig. 2-16 to illustrate the importance of the shape of the velocity anomaly or "basin". (a) Source location (red star) and position of the basin (red ellipse with an aspect ratio of two). (b) The blue curve represents amplitude measurements obtained through the low velocity basin in (a), while the black one is the amplitude predictions generated from a basin with a semi-major axis of 100 km (a=b=100km, which is a circular basin). The red dashed line is the reference amplitude curve for horizontally homogeneous media, while the green dashed line indicates the center of basin.

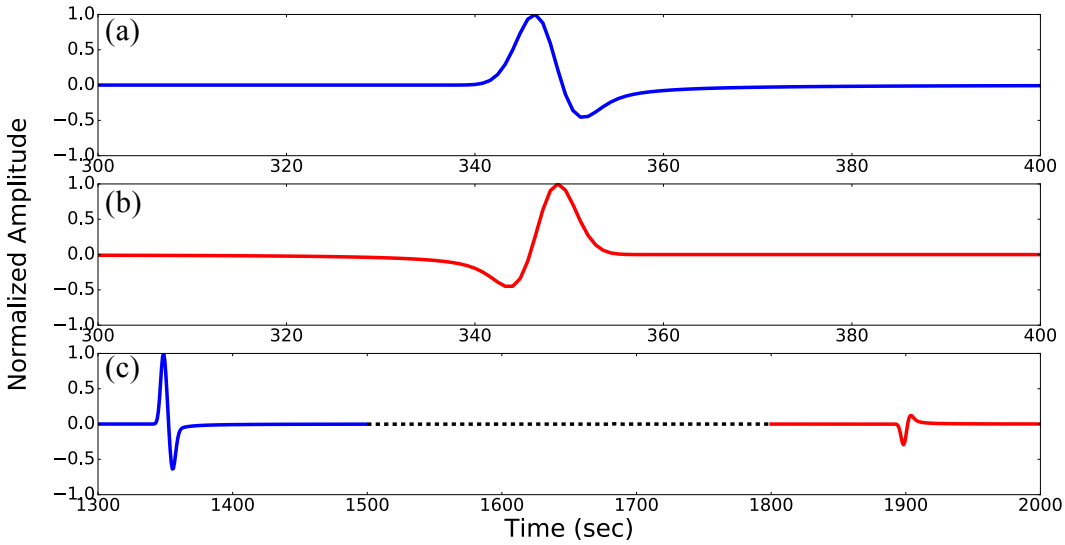

Figure 2-19 Membrane Wave Seismograms

Synthetic seismograms extracted from the 2D membrane wave simulation with an elliptical low velocity anomaly or "basin", the amplitude for each waveform has been normalized. (a) Seismogram extracted at a source-receiver distance of 1000 km. (b) Inverse Hilbert transformed version of (a). (c) Seismogram extracted at a source-receiver distance of 4000 km in which the primary and secondary wave packets are well separated.

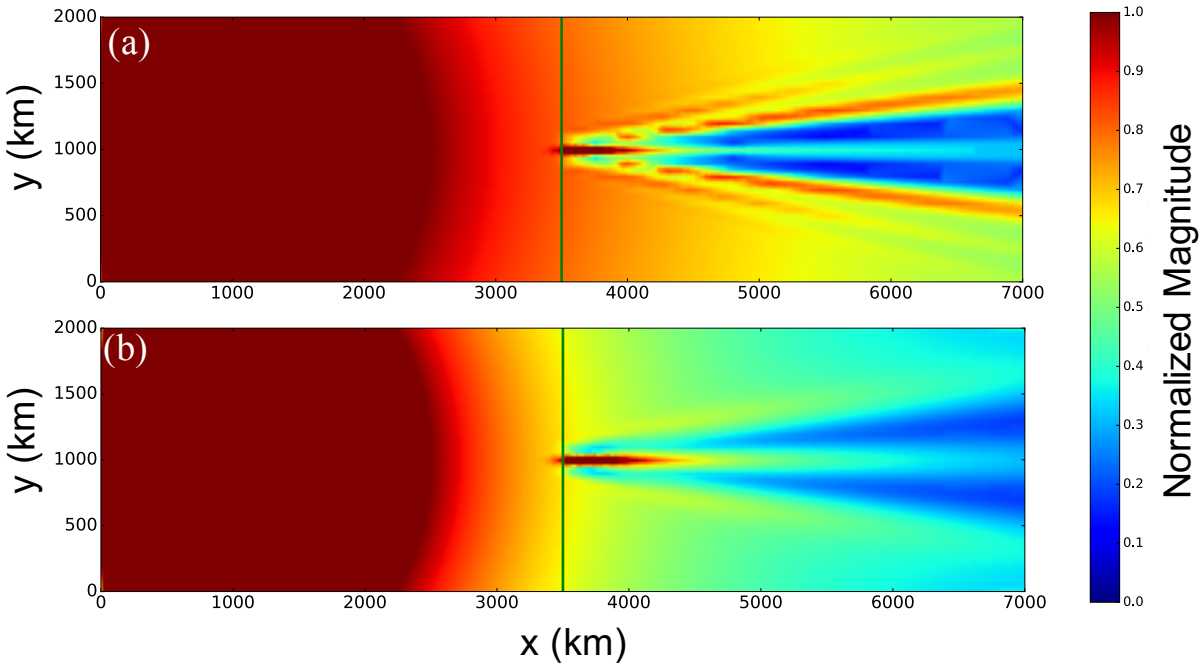

Figure 2-20 Membrane Wave Amplitude Maps

Normalized amplitude maps extracted from the 2D membrane wave simulation with an elliptical low velocity anomaly or "basin". (a) Amplitude map measured based on FTAN. (b) Amplitude map measured based on eq. (7). The vertical green line indicates the center of basin.

In summary, a rule of thumb is that amplification strengthens and the focal length increases when the size of the low velocity anomaly increases, approximately linearly for a low velocity basin with an aspect ratio near 1. However, this relation breaks down for basins with extreme aspect ratios.

2.7.3 Anelastic Attenuation versus Elastic Focusing

The simulations we have presented so far emphasize the effect of near surface elastic heterogeneity on surface wave amplitudes. Now, for comparison, we address the effect of anelastic attenuation

by presenting more 3D simulations using the code SW4. (None of the simulations in this section are in 2D.)

The quality factor Q is lower in sedimentary than non-sedimentary rocks, thus strong anelastic attenuation will decrease amplitudes of surface waves that pass through sedimentary basins, somewhat offsetting amplitude gains caused by elastic structures. Here, we show that the amplification effect due to focusing is expected to be much larger than the attenuation effect due to the anelasticity, at least for basins with an aspect ratio near 1.

We present several different 3D simulations in Cartesian coordinates to investigate this problem. The background input velocity structure in 3D is the 1D model ak135 with a circular basin inserted. The basin has a smoothly varying cross-sectional depth, defined as:

$$z = \begin{cases} \frac{z_{\max}}{2}[1+\cos(\pi r / R)] & r \in [0,R] \\ 0 & r \in (R,\infty) \end{cases} \qquad (8)$$

where $z_{max} = 4\ km$ is the maximum depth of the basin, R = 200 km is the basin's radius, r is the radial distance from the center of the basin. The depth of the basin varies as a half-cosine with radial distance from the center of the basin. The basin's center is 1000 km from the source. The shear wave quality factor Q_s and the shear wave speed v_s are constant in the basin. Given Q_s, Q_P is determined with the empirical relationship of Clouser & Langston (1991) and v_P is determined from v_s by the scaling relationship of Brocher (2005). The three simulations have input basins that differ in quality factor and shear velocity, but have the same geometry.

The model parameters inside the basin for the three input models are summarized in Table 2 and are described as follows. Model 1 has both elastic and anelastic heterogeneity: a low Vs, low Q basin. Model 2 has only elastic heterogeneity: a low Vs but normal Q basin. Model 3 has only

anelastic heterogeneity: a normal Vs but low Q basin. Thus Model 1 contains both a Vs and Q anomaly, Model 2 contains only a Vs anomaly, and Model 3 contains only a Q anomaly. Our main interest is to compare the results of Models 2 and 3, which contain purely elastic and purely anelastic effects, respectively.

Table 2-2 Velocity and quality factor inside the basin for different simulations

Model id	v_S	v_P	Q_S	Q_P
1	2 km/s	3.59 km/s	40	96.8
2	2 km/s	3.59 km/s	600(ak135)	873(ak135)
3	3.46 km/s (ak135)	5.8 km/s(ak135)	40	96.8

We use the amplitude ratio in Figure 2-21a to illustrate the results, which is the ratio of observed amplitude in the simulation (A_{obs}) to the reference amplitude observed with the horizontally homogeneous model ak135 (A_{ref}). Strong anelastic attenuation (Model 3) alone only decreases amplitudes to a small extent (red dots). The elastic structural anomaly (Model 2) has a much larger effect on amplitudes downstream from the basin (green dots). A basin that has both low velocity and low quality factors (Model 1) still results in a significant increase in the amplitudes downstream from the basin (blue dots).

Figure 2-21b shows that the magnitude of the downstream amplitude anomalies in simulations with a purely anelastic heterogeneity varies approximately linearly with the size of the basin, as does the maximum elastic amplitude ratio (Fig. 2-16b). However, the anelastic effect is much smaller. As shown in Figure 2-21a, for a basin with a radius of 200 km, the magnitude of anelastic amplitude decay would be ~7% but the maximum elastic amplification would be ~200%. Thus, the expectation is that elastic amplification effects will have larger impact than anelastic attenuation effects for basins with an aspect ratio near 1.

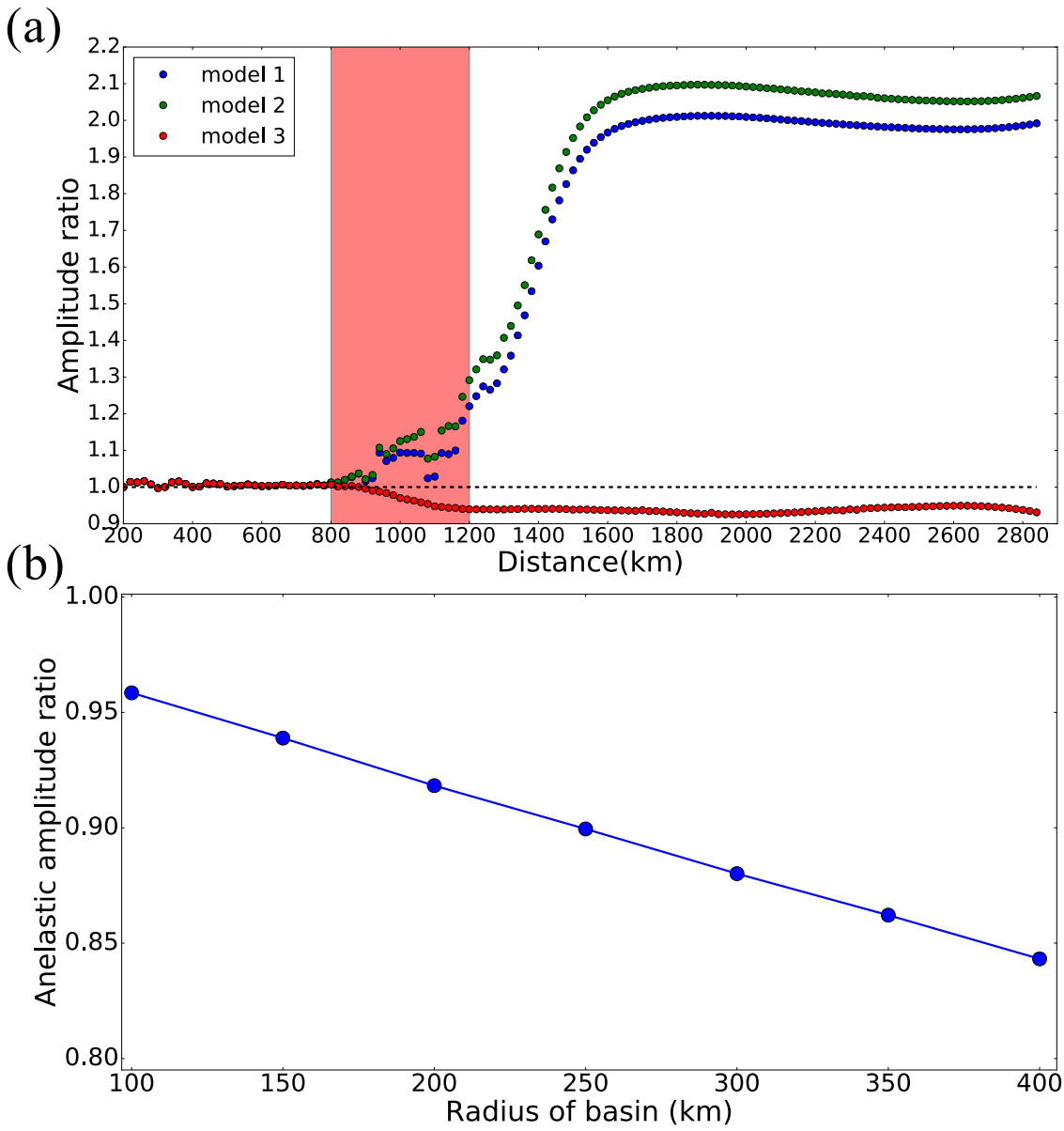

Figure 2-21 Amplitudes from Anelastic Simulations

(a) Amplitude ratio from three 3D simulations with different input models with varying amounts of elastic and anelastic heterogeneity. Model 1: both elastic and anelastic heterogeneity, Model 2: only elastic heterogeneity, Model 3: only anelastic heterogeneity. A full description of the models is summarized in Table 2. (b) Anelastic amplitude ratio is plotted as a function of the radius of the basin, where the anomaly is purely anelastic (i.e., no elastic heterogeneity).

There are three primary exceptions to the dominance of elastic amplification over anelastic attenuation. (1) Anelastic attenuation begins to set on as soon as the wavefield enters the basin and persists approximately constant downstream after the wavefield exists the basin. Elastic amplification does not set on immediately, but maximizes near the focal point which will occur several hundred kilometers downstream from the basin and then decays slowly (Fig. 2-16a). This caveat is more important for large basins whose focal point lies at a greater distance from the basin. For a basin with a 400 km radius, anelastic attenuation will be stronger than elastic amplification within about 250 km from the basin edge in our simulations, but will be weaker outside this distance. (2) Elastic amplification reduces downstream from the focal point, whereas anelastic attenuation remains constant with distance. Thus, for waves that propagate far enough from a basin the elastic amplification may decay to become commensurate with anelastic attenuation. This will be more likely for small basins where the amplification decays more rapidly with distance. However, elastic focusing does not asymptotically approach zero (as discussed earlier). Even for a basin that is only 100 km in radius, the elastic focusing is expected to be much stronger than anelastic attenuation at continental scales (distances less than 10000 km). (3) For basins with extreme aspect ratios, such as shown in Figure 2-17, elastic focusing may be minimal and anelastic attenuation may have a larger impact on amplitudes simply because there is barely any focusing. (4) For an elliptical basin, the wavefield propagating through the long axis may separate into two wave packets. Although focusing of energy still occurs (as shown in Fig. 2-20b), the measured amplitude based on conventional methods may not accurately reflect the amplification of wavefield energy (as shown in Fig. 2-20a). In this case, it is hard to determine whether focusing has a larger impact compared with anelastic attenuation or not.

In conclusion, we expect elastic amplification downstream of on-continent sedimentary basins to dominate anelastic attenuation except very near the basin edge and for basins with extreme aspect ratios.

2.8 Conclusions

This chapter explores the nature of elastic propagation effects on short period surface waves, particularly their amplitudes downstream from sedimentary basins. Our results show that a significant fraction of amplitude variability observed in regionally propagating surface waves (e.g., Bonner et al., 2008) is caused by elastic focusing/defocusing due to lateral wave propagation effects through shallow structures. The focus of this chapter is to understand elastic focusing effects on Rayleigh waves at 10 sec period, which is typically well excited by small earthquakes and nuclear explosions and is also well represented in ambient noise cross-correlations that are commonly used in tomographic studies. The existence and nature of sedimentary basins strongly affect regionally propagating Rayleigh waves at this period.

The primary findings of this chapter are summarized as follows:

(1) With the example of a 3D full waveform simulation across East Asia, we illustrate that elastic velocity heterogeneity of sedimentary basins has a large impact on short period surface wave amplitudes. Ignoring these effects may introduce significant bias in studies that require the correct interpretation of amplitude information, including attenuation tomography and source parameter estimation. We also present an example of Ms estimates to highlight the amplitude variability caused by velocity heterogeneity.

(2) We conclude that the amplitude effect of short period surface wave propagation in a 3D Earth is predominantly governed by horizontal 2D focusing/defocusing, rather than complicated 3D wave propagation phenomena. Several pieces of numerical evidence are provided to establish this

conclusion, which is particularly useful due to the fact that 2D phase speed maps can be used as proxy for 3D structural models to predict surface wave amplitude anomalies. There are several reasons why we believe 2D simulations through phase velocity maps may be preferable to 3D simulations. First, 2D membrane wave simulations are much faster. Second, the existence of water layers can complicate simulations through a 3D model that does not happen in 2D simulations. Third, phase speed maps are closer to data than 3D models and are, therefore, more accurate representations of heterogeneity. Thus, phase speed maps present several advantages in computing amplitude predictions, including that they may be more accurate than those computed through a 3D model.

(3) Several important questions related to the nature of 2D focusing effect are discussed in detail. Most importantly, we compare the effects of anelastic attenuation to elastic focusing and show that on a regional scale elastic focusing through sedimentary basins is more likely to cause significant surface wave amplitude anomalies than anelastic attenuation produced by sedimentary basins except very near the basin edge or for basins with extreme aspect ratios. This explains why negative values of Q_{eff} are commonly observed in observational studies (e.g., Levshin et al., 2010). In the future, it is important to test the principal conclusions of this chapter with real data. This will include tests to observe strong lineations or amplification stripes downstream from sedimentary basins, and perhaps also the de-amplification and propagation deflection stripes that bracket the amplification. In addition, it is also important to test whether the observed features are predicted well with high quality velocity models. To achieve this, there are three major requirements that need to be satisfied. (1) A dense array with high quality seismometers is needed to record accurate spatially resolved amplitude information. The array should be located near to a large sedimentary basin. (2) Seismic events upstream from the basin are also needed with

magnitudes large enough to be recorded by the array. Ideally, they would also be small enough and far enough to be considered as point sources. (3) A high-resolution 3D model (or 2D phase velocity map) also should be available for the study region.

Chapter 3

A 3-D shear velocity model of the crust and uppermost mantle beneath Alaska including apparent radial anisotropy

3.1 Summary

This chapter presents a model of the 3-D shear velocity structure of the crust and uppermost mantle beneath Alaska and surroundings on a ~50 km grid, including crustal and mantle radial anisotropy, based on seismic data recorded at more than 500 broadband stations. The model derives from a Bayesian Monte Carlo inversion of Rayleigh wave group and phase speeds and Love wave phase speeds determined from ambient noise and earthquake data. Prominent features resolved in the model include: (1) Apparent crustal radial anisotropy is strongest across the parts of central and northern Alaska that were subject to significant extension during the Cretaceous, consistent with crustal anisotropy being caused by deformationally-aligned middle to lower crustal sheet silicates (micas) with shallowly dipping foliation planes beneath extensional domains. (2) Crustal thickness estimates are similar to those from receiver functions by Miller & Moresi (2018). (3) Very thick lithosphere underlies Arctic-Alaska, with high shear wave speeds that extend at least to 120 km depth, which may challenge rotational transport models for the evolution of the region. (4) Subducting lithosphere beneath Alaska is resolved, including what we call the “Barren Islands slab anomaly”, an “aseismic slab edge” north of the Denali Volcanic Gap, the “Wrangellia slab anomaly”, and Yakutat lithosphere subducting seaward of the Wrangell volcanic field. (5) The geometry of the Alaskan subduction zone generally agrees with the slab model Alaska_3D 1.0 of Jadamec & Billen (2010) except for the Yakutat “slab shoulder region”, which is newly imaged in our model.

3.2 Introduction

Alaska is a region composed of crustal fragments squeezed between the Siberian and Laurentian cratons. It is characterized by a particularly variable crust that was built by subduction, large block rotation in the north (e.g., Moore and Box, 2016), extensional tectonics (e.g., Johnston, 2001), and the successive accretion of terranes along both convergent and strike-slip fault systems in the south (e.g., Coney & Jones, 1985; Johnston, 2001). The active southern margin of Alaska is particularly complex, and tectonic growth is on-going due to the underthrusting of the Pacific plate in the Alaska-Aleutian subduction zone and the collisional orogeny produced by the Yakutat crustal block as shown in **Figure 3-1a**, which is intersecting and subducting beneath at least parts of central Alaska (e.g., Jadamec and Billen, 2010; Haynie and Jadamec, 2017). The Yakutat microplate (**Fig. 3-1b,** modified from Eberhart-Philips et al., 2006), is the most recent exotic terrane assimilated onto the North American continent. All parts of Alaska continue to move relative to stable North America and active seismicity is found across most of the state (Freymueller et al., 2008). The potential for damage caused by earthquakes, volcanic eruptions, and tsunamis is exceptionally high across a great deal of the state.

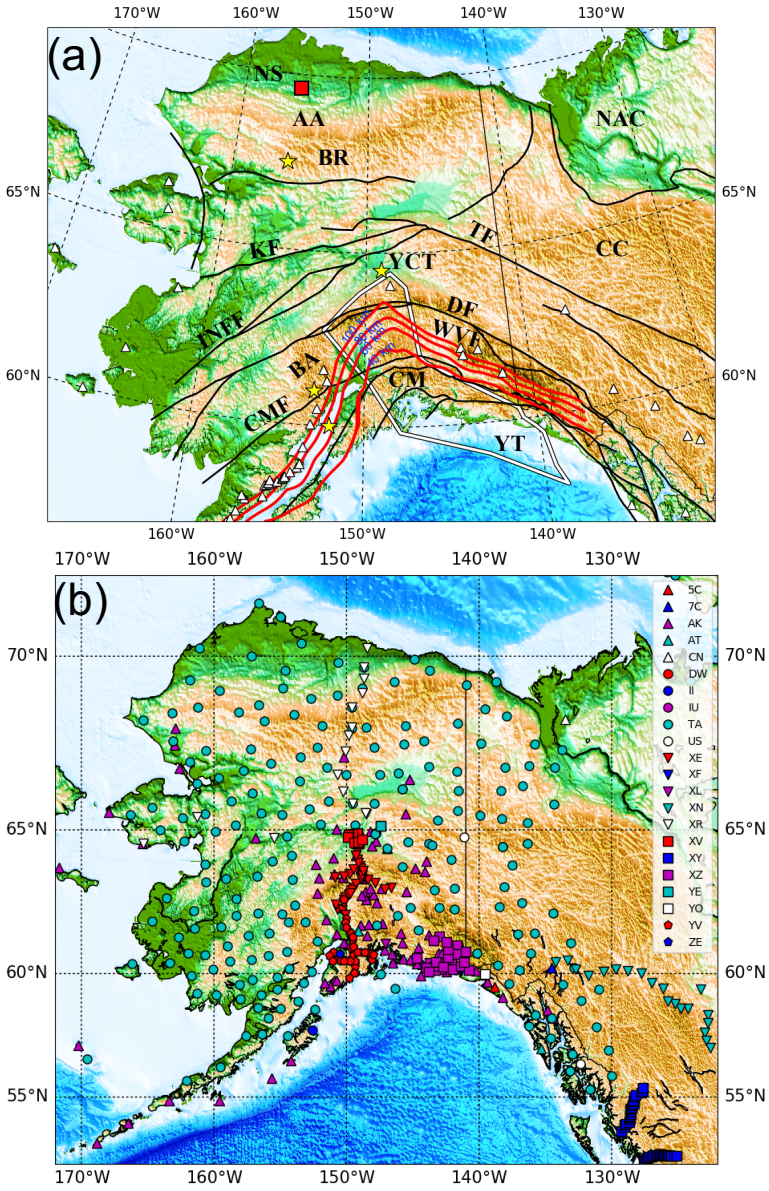

Figure 3-1 Geological and Station Distribution Maps

(a)Geologic and tectonic features and nomenclature. The black curves are major faults, and the four red curves are top edges of the subducting Alaskan-Aleutian slab at different depths: from south to north: 40 km, 60 km, 80 km and 100 km (Jadamec and Billen, 2010). The white polygon is the hypothesized Yakutat Terrane (Eberhart-Phillips et al., 2006). Structural and tectonic features are identified with abbreviations explained in Table 3-1. The four yellow stars indicate sample grid points located in the Brooks Range (BR), the Aleutian slab Back-Arc region, the Cook Inlet, and the Yukon Composite Terrane (YCT) used in Figures 3-2, 3-6, 3-7, 3-8, 3-10, and 3-16, and the red square is the location in the Colville Basin used in Figure 3-7. (b) Station distribution. There are 22 networks indicated with different symbols. The USArray Transportable Array and the Alaska Network are the largest networks, identified with green circles and purple triangles, respectively.

Table 3-1 Names of the structural features identified with abbreviations

Abbreviation	Name
AA	Arctic Alaska
BA	Back-Arc
BR	Brooks Range
CC	Canadian Cordillera
CMF	Castle Mountain Fault
CM	Chugach Mountains
DF	Denali Fault
INFF	Iditarod-Nixon Fork Fault
KF	Kaltag Fault
NAC	North American Craton
NS	North Slope
TF	Tintina Fault
WT	Wrangellia Terrane
WVF	Wrangell Volcanic Field
YCT	Yukon Composite Terrane
YT	Yakutat Terrane

Geological and tectonic interest in Alaska as well as the natural hazards, have motivated a rapid expansion of seismic instrumentation across the state, including the recently deployed EarthScope USArray Transportable Array (TA). These data now present the unprecedented opportunity to model the earth's crust and mantle beneath Alaska in much greater detail.

Existing studies of the crust and mantle beneath Alaska have been based on a variety of types of data and approaches, including seismic refraction and reflection profiling (e.g., Fuis et al., 1995, 2008), receiver function analyses (e.g., Ferris et al., 2003; Rondenay et al., 2010; O'Driscoll and Miller, 2015; Miller & Moresi, 2018; Miller et al., 2018; Zhang et al., 2019), body wave tomography for isotropic and anisotropic structures (e.g., Zhao et al;, 1995; Eberhart-Phillips et al., 2006; Tian and Zhao, 2012; Martin-Short et al., 2016; Gou et al., 2019), shear wave splitting studies (e.g., Yang & Fischer, 1995; Wiemer et al., 1999; Christensen & Abers, 2010; Hanna & Long, 2012), ambient noise tomography (e.g., Ward, 2015), and earthquake surface wave tomography (e.g., Wang & Tape, 2014). Some studies combined multiple datasets. For example,

Allam et al. (2017) used body wave double-difference tomography and receiver functions to infer crustal and mantle structures along the Denali fault system. Ward & Lin (2018) performed a joint inversion of ambient noise surface waves and receiver functions to constrain shear wave speeds beneath Alaska. Jiang et al. (2018) used the ambient noise measurements from Ward and Lin (2018) and introduced longer period measurements from earthquakes and S-wave travel time residuals to construct an isotropic Vs model of the crust and upper mantle. Similarly, Martin-Short et al. (2018) present results of a joint inversion of ambient noise, earthquake-based surface waves, P-S receiver functions, and teleseismic S-wave travel times.

The purpose of this study is to construct a 3-D model of apparent radial anisotropy of shear wave speeds (Vsv, Vsh) in the crust and upper mantle beneath Alaska using surface wave observations. The model is based on data recorded by the TA as well as other permanent and temporary networks in and around Alaska (**Fig. 3-1b**). To achieve this purpose, we perform surface wave ambient noise tomography across Alaska as well as earthquake tomography, which extends dispersion measurements to longer periods. The resulting Rayleigh wave dispersion curves run from 8 to 85 s period and Love wave curves from 8 to 50 s. The model may serve usefully as the basis for earthquake location and source characterization, and to predict other types of geophysical data (e.g., body wave travel times, gravity, perhaps mantle temperature). It may also serve as the basis for wavefield simulations (e.g., Feng and Ritzwoller, 2017), and radial anisotropy provides information about crustal and mantle deformation (e.g., Moschetti et al., 2010; Xie et al., 2013). It is also designed to provide a starting point for further studies that introduce complementary datasets (e.g., receiver functions, Rayleigh wave H/V ratio, Rayleigh wave azimuthal anisotropy, body waves, shear wave splitting, and so forth) to refine the model. Such refinements may result in better determination of shallower structures and internal interfaces within the Earth (e.g., Shen

& Ritzwoller, 2016), as well as estimates of the full depth-dependent elastic tensor in the crust and mantle (e.g., Xie et al., 2015, 2017). Within a Bayesian Monte Carlo framework (e.g., Shen et al., 2013), we strive to provide reliable information about model uncertainties across the region of study, which will help guide the future use of the model.

The principal novelty of this study lies in the simultaneous interpretation of Rayleigh and Love wave data. By measuring dispersion curves from both types of surface waves we are able to present the first model of Vsh as well as Vsv for the Alaskan crust and uppermost mantle. This results in the estimation of apparent radial anisotropy, about which we say more directly below. There are three other noteworthy characteristics of the study. (1) We include data through February 2019, which improves data coverage, particularly for the Brooks Range and the Alaska North Slope, and the model extends over a larger region than many earlier studies. (2) By employing earthquake data, the resulting surface wave data set is broad band, extending from 8 s up to 85 s period, which allows simultaneous constraints to be placed on structures in the mantle and in the shallow crust. (3) We estimate model uncertainties, which guides the assessment and interpretation of the resulting 3D model.

In discussing anisotropy using surface waves, it is useful to bear in mind two coordinate systems. The first is the frame defined by a symmetry axis (or foliation plane) of the medium of transport, in which “inherent” anisotropy is defined, and the second is the frame of the observations where “apparent” anisotropy is defined. We follow Xie et al. (2017) and refer to measurements of anisotropy and inferences drawn from them in the observational frame as “apparent”. Apparent S-wave radial anisotropy, also referred to as polarization anisotropy, is the difference in propagation speed between horizontally (Vsh) and vertically polarized (Vsv) S-waves, where Vsh and Vsv are properties of the medium defined in the observational frame. A common measure of the strength

of apparent S-wave radial anisotropy is the Thomsen parameter (Thomsen, 1986; Xie et al., 2017), γ, which is approximated by

$$\gamma = \frac{V_{sh} - V_{sv}}{V_{sv}}. \quad (1)$$

γ is inferred by simultaneously interpreting Rayleigh waves, which are dominantly sensitive to Vsv, and Love waves, which are exclusively sensitive to Vsh. Without introducing apparent radial anisotropy, Rayleigh and Love wave dispersion curves commonly cannot be fit simultaneously, a phenomenon often referred to as the "Rayleigh-Love discrepancy". Hereafter, whenever we refer to "radial anisotropy", we will mean apparent S-wave radial anisotropy.

Most studies of anisotropy, including this chapter, report measurements and models of particular aspects of apparent anisotropy. In contrast, Xie et al. (2015, 2017) present methods that use observations of apparent radial and azimuthal anisotropy to infer characteristics of the depth-dependent elastic tensor, which possesses information about inherent anisotropy. In this study, we do not present azimuthal anisotropy, therefore the inference of inherent anisotropy is beyond the scope of this chapter.

Strong radial anisotropy is a common mantle property (e.g., Montagner and Tanimoto, 1991; Ekstrom and Dziewonski, 1998; Shapiro and Ritzwoller, 2002; Marone et al., 2007; Kustowski et al., 2008; Nettles and Dziewonski, 2008; Yuan et al., 2011). This is often interpreted to result from the lattice preferred orientation (LPO) of olivine, which is approximately an orthorhombic mineral, and develops due to strain caused by plate motions. In a number of regions around the earth (e.g., Tibet, western US), strong crustal radial anisotropy has been found to coincide with extensional provinces (e.g., Moschetti et al., 2010; Xie et al., 2013), and this anisotropy is presumed to be caused by the LPO of crustal minerals, notably micas, whose foliation plane orients sub-

horizontally under significant horizontal strain. Thus, observations of apparent radial anisotropy provide qualitative information about the deformation state of the crust or upper mantle. In the long run, however, it may be worthwhile to consider observations of apparent radial anisotropy as a stepping stone to more complete estimates of the elastic tensor and inference of inherent anisotropy, as performed by Xie et al., (2015, 2017). In addition, we discuss radial anisotropy in the North Slope Foreland Basin, or Colville Basin (Bird and Molenaar, 1992), which is the largest basin in Alaska.

The chapter is organized as follows. In section 3.3 we present information about the data sets and the tomographic methods used in this study, including how we estimate uncertainties. Section 3.4 presents the 2-D phase and group speed maps along with corresponding uncertainties, and section 3.5 shows how the shear wave speed model (Vsv and Vsh) is produced by a Bayesian Monte Carlo inversion given dispersion data and uncertainties extracted from the tomographic maps. We present the features revealed by the model in section 3.6 and discuss them in section 3.7.

3.3 Data, Tomographic Methods, and Uncertainty Estimation

3.3.1 Data

This study utilizes seismic records from 22 permanent and temporary networks deployed across Alaska and northwest Canada between January 2001 and February 2019 (**Fig. 3-1b**). There are 537 seismic stations in total. Network names are listed in **Table 3-2**. Among those networks, the largest are the Transportable Array (TA) and the Alaska Regional Network (AK), which consist of 198 and 112 stations, respectively, and together compose nearly 60% of the stations used.

Table 3-2 Description of seismic networks used in this study.

Network	Description
5C	Dynamics of Lake-Calving Glaciers: Yakutat Glacier, Alaska
7C	The Mackenzie Mountains Transect: Active Deformation from Margin to Craton
AK	Alaska Regional Network
AT	National Tsunami Warning System
AV	Alaska Volcano Observatory
CN	Canadian National Seismograph Network
II	Global Seismograph Network (GSN - IRIS/IDA)
IU	Global Seismograph Network (GSN - IRIS/USGS)
PN	PEPP-Indiana
PO	Portable Observatories for Lithospheric Analysis and Research Investigating Seismicity
PP	Princeton Earth Physics Program
TA	USArray Transportable Array (NSF EarthScope Project)
US	United States National Seismic Network
XE	Broadband Experiment Across Alaskan Range
XN	Canadian Northwest Experiment
XR	Structure and Rotation of the Inner Core (ARCTIC)
XY	Batholith Broadband
XZ	STEEP: St. Elias Erosion and Tectonics Project
YE	Bench Glacier Seismic Network
YM	Denali Fault Aftershocks RAMP
YV	Multidisiplinary Observations of Subduction (MOOS)
ZE	Southern Alaska Lithosphere and Mantle Observation Network

We perform ambient noise data processing by following the procedures described by Bensen et al. (2007), Lin et al. (2008), and Ritzwoller and Feng (2019). The Rayleigh wave is retrieved from the vertical-vertical (ZZ) component of the noise correlations while the Love wave is obtained from the transverse-transverse (TT) component. We then measure Rayleigh wave phase and group speeds between 8 and 60 s period and Love wave phase speed between 8 and 50 s period across the entire study region using automated frequency-time analysis. Additionally, we obtain broadband waveforms from teleseismic earthquakes with Ms > 5.0 (about 1,500 events), from which we obtain Rayleigh wave phase speed measurements from 30 to 85 s period and Love wave

phase speed measurements from 30 to 50 s period to complement and augment the ambient noise data base.

3.3.2 Tomographic methods

Where the distribution of stations is relatively dense and regular, we are able to perform eikonal tomography (Lin et al., 2009), a geometrical ray theoretical method, to produce phase speed maps from ambient noise dispersion data. Eikonal tomography results in local observations of phase speed and uncertainty versus the azimuth of propagation, as exemplified by **Figure 3-2**. For each grid point and period where eikonal tomography is performed, phase speed measurements are averaged in 18-degree azimuthal bins, and the standard deviation of the mean, σ_i , is computed for the measurements in each azimuthal bin i. The isotropic phase speed measurement for the grid point is the weighted average of the bin-averages, where the weights are the reciprocals of the σ_i. The standard deviation of the isotropic phase speed is the mean of the bin standard deviations divided by the square root of the number of bins. Interpretation of the azimuthal variation of the measurements is beyond the scope of this chapter.

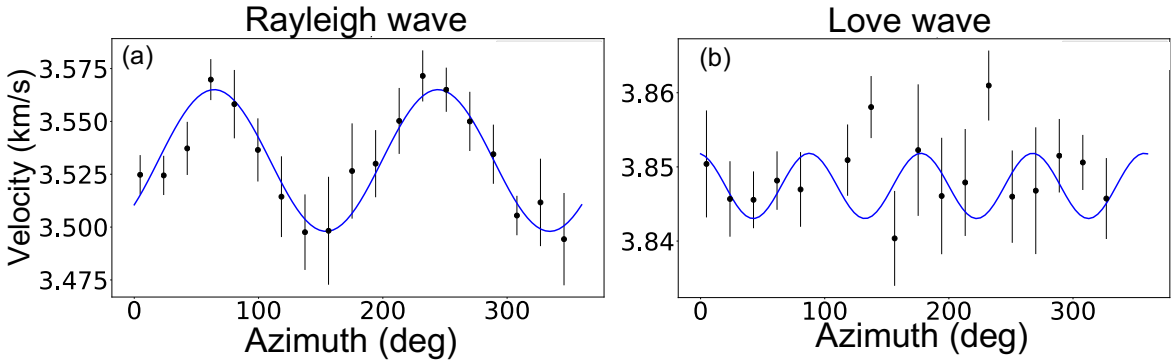

Figure 3-2 Azimuthal Phase Speed Measurements

Azimuthal bin-averaged phase velocity measurements and bin standard deviations plotted versus azimuth (θ) measured using the eikonal tomography method in the Yukon Composite Terrane at 20 s period. (a) For Rayleigh waves, we fit a 2θ curve to the bin averages, where θ is azimuth. (b) For Love waves, we fit a 4θ curve. Interpretation of the azimuthal variation of the measurements is beyond the scope of this chapter.

The region where eikonal tomography has been applied is encircled with black dashed lines in **Figures 3-3a, 3-3b and 3-3c** and **3-4a, 3-4b and 3-4c** for Rayleigh and Love wave phase speeds, respectively. Elsewhere, where eikonal tomography is inapplicable, we apply a great-circle (or straight-ray) tomographic method (Barmin et al., 2001), which extends the region of coverage substantially. The straight ray method is applied across the entire region of study to construct the Rayleigh wave group speed maps (**Fig. 3-3d, 3-3e and 3-3f**). The group speed measurements help to improve constraints on the shallower parts of the earth structure. We do not use Love wave group speed data because of lower quality. We also apply eikonal tomography to Rayleigh and Love wave earthquake travel time measurements to extend phase speed maps to longer periods. We find that the impact of Helmholtz tomography (Lin & Ritzwoller, 2011), which models finite frequency effects on the long period surface wave maps, is small compared with the uncertainties of the maps. Therefore, here we do not apply the finite frequency corrections.

Comparisons of straight ray tomographic to eikonal tomographic maps have been presented by Lin et al. (2009) and Shen et al. (2016). There is typically a small mean difference caused by the fact that eikonal tomography models off-great circle propagation, and maps constructed with that method are typically slightly slower than those based on great-circle rays. We see similar comparisons across Alaska. However, the two methods are consistent within the uncertainties of the maps, as long as the damping applied in the straight ray method is calibrated to match eikonal tomography in the region of overlap of the methods. Thus, straight ray tomography can be applied reliably to extend the coverage of the dispersion maps outside the zone of applicability of eikonal tomography.

In practice, we construct the finalized phase speed maps by combining the ambient noise and earthquake measurements rather than performing tomography for each data set separately and then

combining the dispersion maps. For Rayleigh waves, from 8 – 28 s only ambient noise measurements are used, but from 30 – 60 s the phase speed maps are constructed by averaging the ambient noise and earthquake measurements. Finally, for periods above 60 s, only earthquake measurements are used. For Love waves, from 8 – 28 s only the ambient noise data set is used, but from 30 – 50 s the phase speed maps are constructed using both ambient noise and earthquake measurements. The combination of the two types of measurements (ambient noise and earthquake travel times) enhances the quality of the tomographic maps when both types of measurements are available and is motivated by the fact that the maps produced from ambient noise or earthquake data alone are consistent, as illustrated by Ritzwoller et al. (2011).

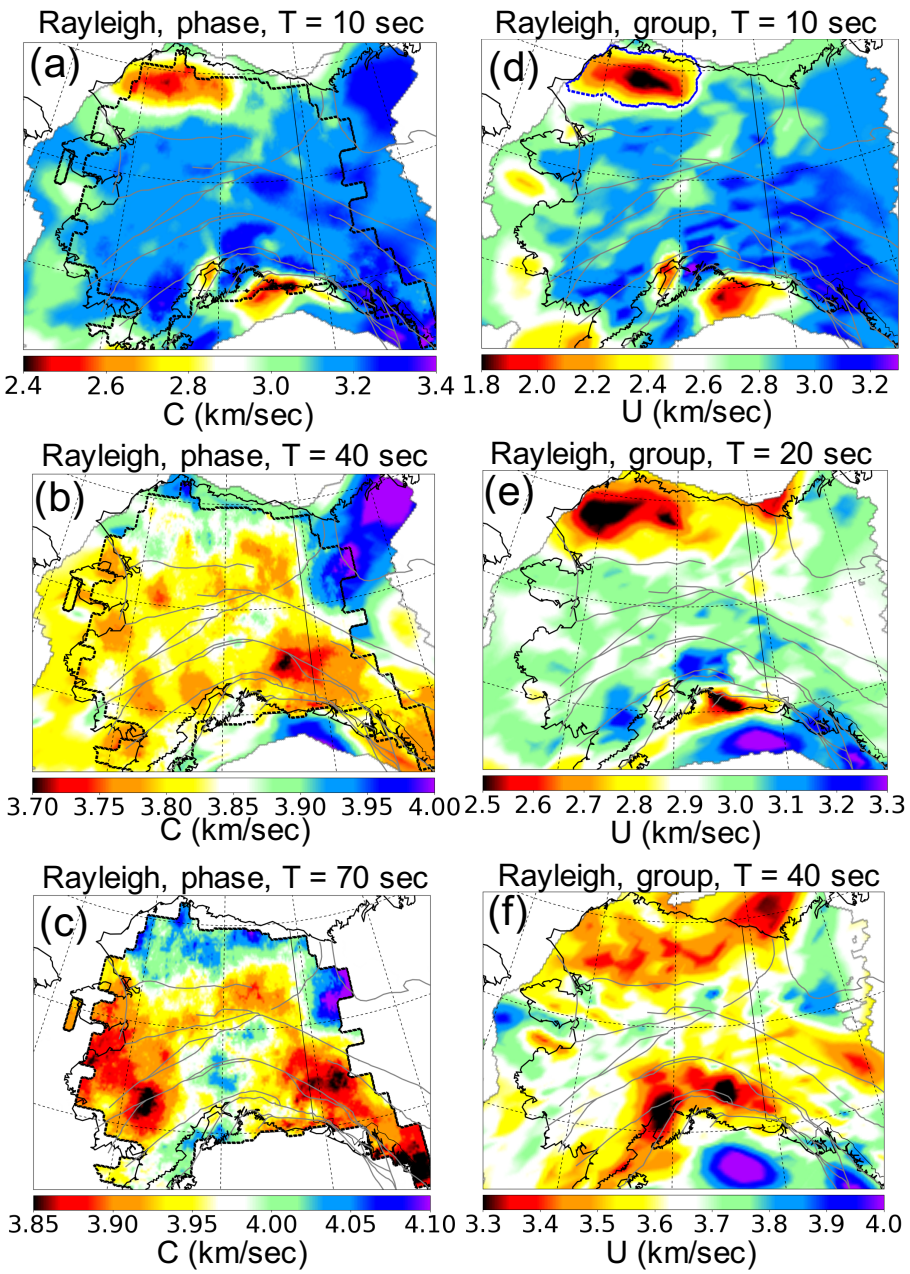

Figure 3-3 Rayleigh Wave Phase Speed Maps

(a) - (c) Rayleigh wave phase speed maps at periods of 10 s, 40 s, and 70 s. The 10 s map is constructed from ambient noise tomography (ANT), 40 s is from a combination of ambient noise and earthquake tomography (ET), and the 70 s map is from ET alone. (d) - (f) Rayleigh wave group speed maps for periods of 10 s, 20 s, and 40 s constructed with ANT. The black piece-wise linear contours in the left column enclose the regions where eikonal tomography is performed. Outside of these contours and for the maps in the right column ray theoretic tomography is performed (Barmin et al., 2001). The dark blue dotted contour in (d) indicates the location of the North Slope Foreland Basin (Colville Basin), where the 10 s Rayleigh wave group speed is less than 2.5 km/s.

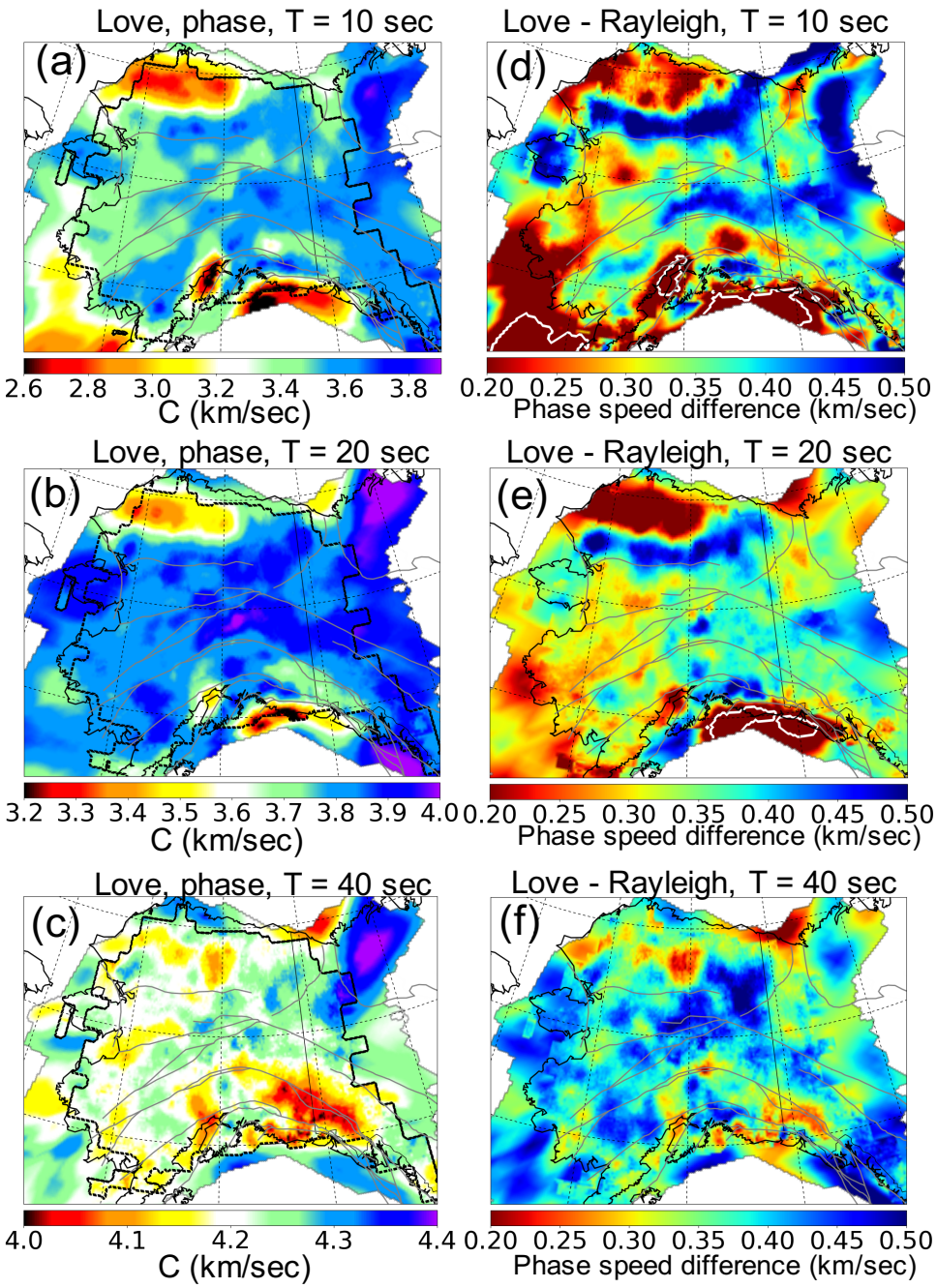

Figure 3-4 Love Wave Phase Speed Maps

(a) - (c) Love wave phase speed maps at periods of 10 s, 20 s, and 40 s, where the 10 s and 20 s maps are constructed using ambient noise tomography (ANT), and 40 s is from a combination of ANT and earthquake tomography. (d) - (f) Differences in phase speed between Love waves and Rayleigh waves at 10 s, 20 s, and 40 s, respectively. The black piece-wise linear contours in the left column enclose the regions where eikonal tomography is performed. Outside of these contours ray theoretic tomography is performed (Barmin et al., 2001). The white contours in (d) and (e) are regions where the Love wave is slower than the Rayleigh wave, which occurs in wet regions.

3.3.3 Uncertainty estimates

As discussed in section 3.3.2, eikonal tomography produces uncertainty estimates where it is performed for phase speed. This approach does not estimate systematic errors or account for the correlation of errors in different travel time measurements. Therefore, as suggested by Lin et al. (2009), we multiply the error estimate from eikonal tomography by a factor of 2.0, which provides a more realistic estimate of uncertainty at each point on a phase speed map.

In the peripheral parts of the study region, where eikonal tomography cannot be performed, the maps derive from straight ray tomography (Barmin et al., 2001), which does not produce estimates of uncertainty but does provide resolution estimates. Similar to Shen et al. (2016), we infer uncertainties in these regions from resolution by applying an empirical scaling relationship that transforms resolution (in km) to uncertainty (in m/s) using the following formula:

$$\sigma(\vec{r}) = kR(\vec{r}) \tag{2}$$

where $\sigma(\vec{r})$ is the uncertainty estimate at location $\vec{r}$ where eikonal tomography has not been performed, and $R(\vec{r})$ is the estimate of resolution, which is the standard deviation of the resolving kernel at the location (Barmin et al., 2001). We estimate the value of k in equation (2) for each period separately at the grid points where both the eikonal and straight ray tomographic results are available. Typical values of k are $\sim 0.2 \times 10^{-3}\ \mathrm{s}^{-1}$, so that a 50 km resolution produces an uncertainty estimate of about 10 m/s.

Because we construct group speed maps with straight ray tomography, we must scale resolution to uncertainty everywhere. Uncertainties for group speed maps are also computed from equation (2), but we multiply k (determined for phase speed at that period) by a factor of 2.0, which amplifies group speed uncertainties by a factor consistent with relative data misfit found in

constructing the dispersion maps. Absolute residuals for group speed measurements are typically about twice as large as phase speed residuals.

Spatially averaged uncertainties for Rayleigh and Love phase speeds, taken from the uncertainty maps, are shown in **Figure 3-5**. The spatial distribution of the uncertainties is quite homogeneous in the interior of the region of study, but degrades in a systematic way near the periphery. Rayleigh and Love wave phase speed uncertainties average about 20-30 m/s, but grow at the shorter and longer periods. Rayleigh wave group speed uncertainties tend to be about twice as large. The uncertainty in the difference between Love and Rayleigh wave speeds is about the square-root of 2 times larger than uncertainties in either wave type. Love wave phase speed uncertainties grow to be larger than the Rayleigh wave uncertainties above 30 s period where earthquake data are introduced because more earthquakes produce high-quality phase time measurements for Rayleigh waves than for Love waves.

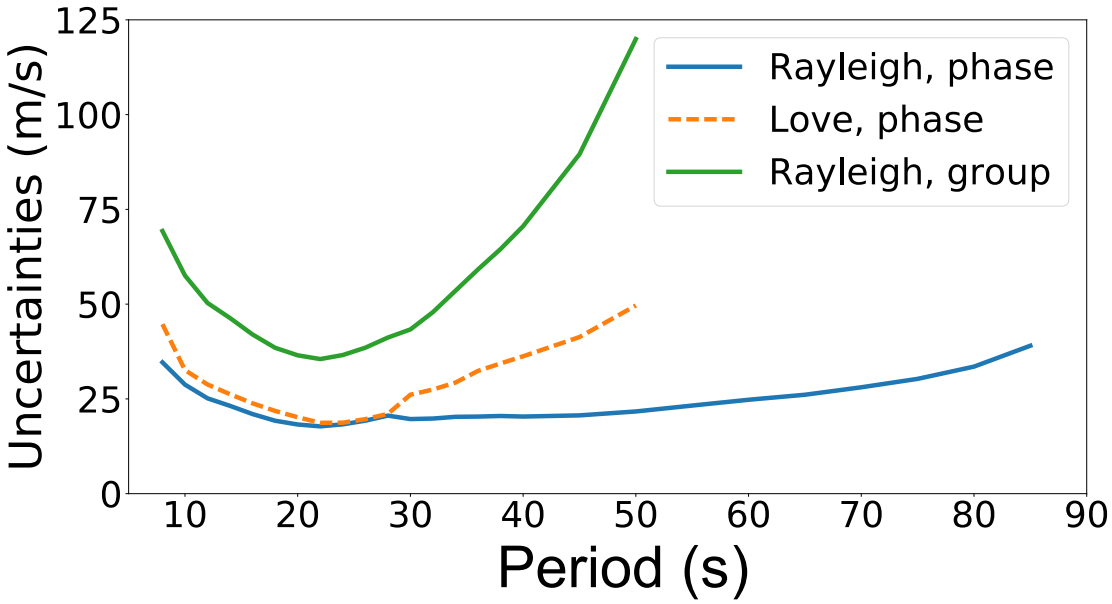

Figure 3-5 Uncertainties v.s. Periods

Estimated measurement uncertainties as a function of period averaged across the study region. The legend identifies the wave type for each curve. These uncertainties are twice the standard deviation of the mean of azimuthally binned standard deviations that result from eikonal tomography (e.g., Fig. 3-2).

3.4 Tomographic Maps

Examples of Rayleigh wave phase and group speed maps are presented in **Figure 3-3**. At 10 s period (**Fig. 3-3a,d**), the Rayleigh wave is most sensitive to the uppermost crust including sedimentary basins. Several sedimentary basins, including the North Slope foreland basin, which we call the Colville basin, as well as several smaller basins are captured in the group speed map. Because group speed at each period has a shallower sensitivity than phase speed, the 20 s group speed map (**Fig. 3-3e**) is qualitatively quite similar to the 10 s phase speed map (**Fig. 3-3a**). The black contour on the 10 s group speed map (**Fig. 3-3d**) identifies the Colville basin and is used later in the chapter. The 40 s group speed (**Fig. 3-3f**) strongly reflects changes in crustal thickness, where lower wave speeds indicate deeper crust. The high velocity anomaly located in the northeast corner of the 40 and 70 s period Rayleigh wave phase speed maps (**Fig. 3-3b, c**) identifies the North American craton. At 70 s, there are high velocity anomalies associated with the subducting Pacific slab and the Arctic Alaska craton.

Figure 3-4a, 3-4b and 3-4c presents examples of Love wave phase speed maps at periods of 10, 20 and 40 s. Love waves sample somewhat more shallowly than Rayleigh waves at the same period, so it is not surprising that the 20 s Love wave phase speed map is qualitatively similar to the Rayleigh wave map at 10 s period.

We also present the differences in phase speed between Love and Rayleigh waves in **Figure 3-4d, 3-4e and 3-4f**. The white contours identify the regions where the Love wave is slower than the Rayleigh wave, which is a consequence of the existence of a water layer and thick sediments. Fitting the difference between Rayleigh and Love wave velocities is one of the primary goals of a model of apparent radial anisotropy.

3.5 Constructing the 3-D Model

Local Rayleigh wave phase and group speed and Love phase speed curves with uncertainties are taken directly from the associated dispersion and uncertainty maps on a spatial grid with a 1.0° spacing in longitude and 0.5° spacing in latitude, resulting on average in about a 50 km grid spacing. Dispersion curves with uncertainties presented as error bars are shown for four example locations (Brooks Range, Yukon Composite Terrane, the Alaska subduction zone Back-Arc, and the Cook Inlet) in Alaska in **Figure 3-6**. These locations are identified with yellow stars in **Figure 3-1a**. Typically, Love wave phase speed is greater than Rayleigh wave phase speed at the same period, but there are exceptions in wet regions at short periods (e.g., Cook Inlet, **Fig. 3-6d**).

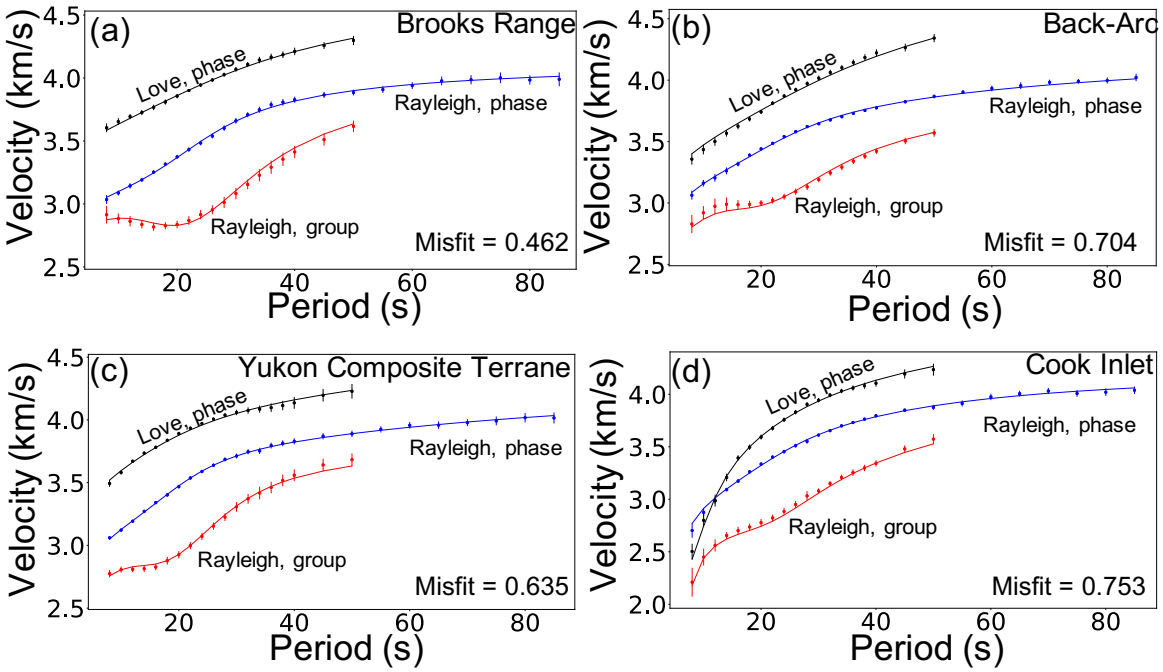

Figure 3-6 Examples of Dispersion Data

Examples of the Rayleigh wave phase and group speed curves and Love wave phase speed curves at four locations identified with yellow stars in Fig. 3-1: (a) Brooks Range, (b) Aleutian Back-Arc, (c) Yukon Composite Terrane, and (d) Cook Inlet. The error bars (blue: Rayleigh wave phase, red: Rayleigh wave group, black: Love wave phase) are observed dispersion measurements with one standard deviation uncertainties. Solid curves (blue: Rayleigh wave phase, red: Rayleigh wave group, black: Love wave phase) are predictions from the 3-D model, namely the mean of the posterior distribution of models at each depth including crustal and mantle anisotropy (Vsv, Vsh). Misfit is defined by equation (3).

The local surface wave dispersion curves are the input for the Bayesian Monte Carlo inversion that produces a posterior distribution of vertical shear wave speed (Vsv, Vsh) profiles that predict the dispersion data acceptably. We closely follow the inversion procedure described by Shen et al. (2016), which consists of three steps.

(1) The first step is to construct the prior distribution of models on the 50 km grid. The prior distribution is controlled by the model parametrization, the reference model, and constraints on each model parameter. The range of the model variables is typically broad enough that an ensemble of models with acceptable data fits can be found.

(2) The second step is the Monte Carlo sampling of model space and determining data misfit. Based on the Metropolis algorithm (Mosegaard & Tarantola, 1995), we perform a series of random walks in model space that select a chain of candidate models in the prior distribution. For each individual model selected in the random walk, theoretical Rayleigh wave phase and group speed and Love wave phase speed curves are computed using the transversely isotropic forward code of Robert Herrmann's Computer Programs in Seismology (Herrmann, 2013) with earth flattening, and the misfit to the data at each point is calculated. Data misfit is defined as follows:

$$\chi = \sqrt{\frac{1}{N}\sum_{i=1}^{N}\frac{(d_i - p_i)^2}{\sigma_i^2}} \tag{3}$$

where d_i is an observed datum (Rayleigh wave phase or group speed or Love wave phase speed), p_i is that data value predicted from a given model, and σ_i is the one standard deviation data uncertainty. The index i ranges over dispersion data, where N is the number of the data values. A chain of candidate models terminates when sufficient steps have been taken to reach an equilibrium in model space and misfit. Then, the inversion starts afresh at a random point in the prior distribution with a new chain and the procedure is repeated on the order of 300 times.

(3) The third step is to construct the posterior distribution. After the second step terminates at each grid point, the model with the best data fit is identified as the "best fitting model" with misfit $\chi_{\min}$ and the "mean model" ($\bar{m}$) is defined as the mean of the ensemble of accepted models at each depth and for each discontinuity. Examples of average models at two locations are shown in **Figure 3-7**. A model is accepted if the misfit is less than $\chi_{\min} + 0.5$, where $\chi_{\min}$ is the misfit value for the best fitting model.

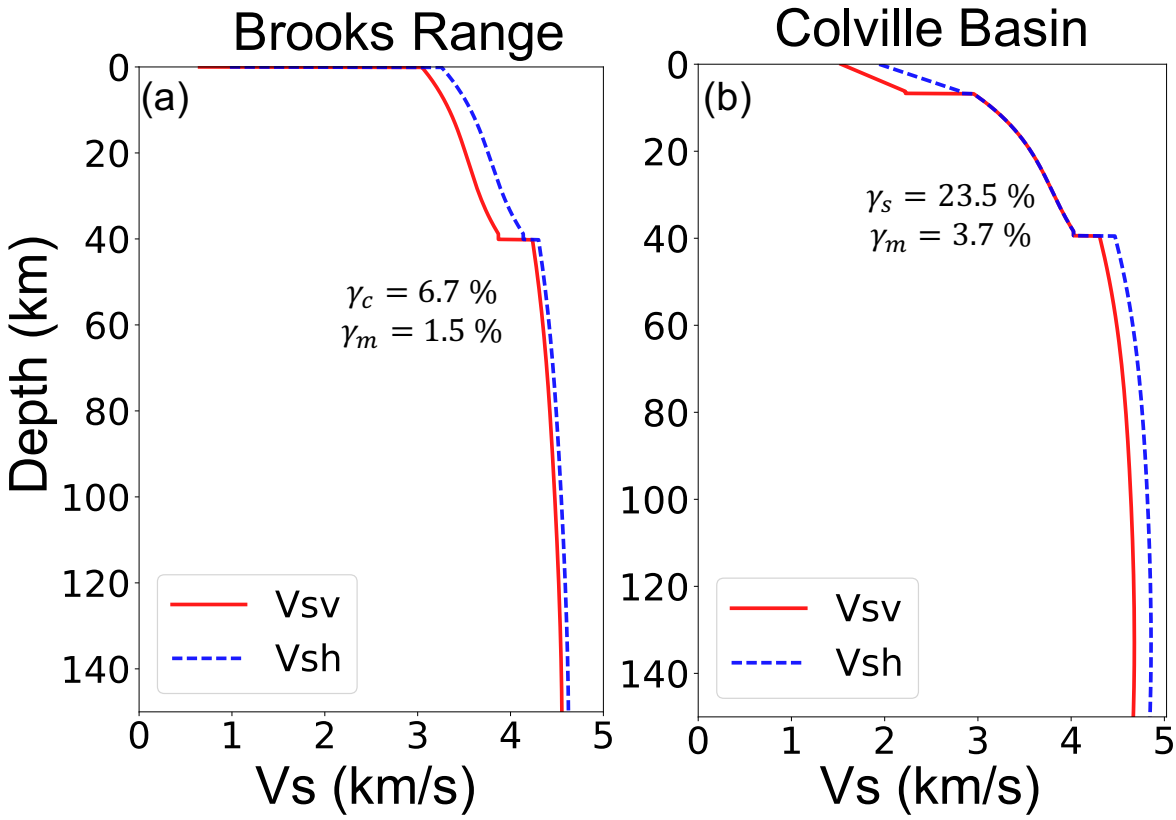

Figure 3-7 Sample Vsv/Vsh Profiles

Examples of the mean of the posterior distribution plotted versus depth. (a) Brooks Range (yellow star in Fig. 3-1a), Vsv and Vsh profiles with crustal and mantle anisotropy but no sedimentary anisotropy ($\gamma_s = 0, \gamma_c \neq 0 \neq \gamma_m$). (b) Colville Basin (red square in Fig. 3-1a), Vsv and Vsh profiles with sedimentary anisotropy and mantle anisotropy but no crustal anisotropy ($\gamma_c = 0, \gamma_s \neq 0 \neq \gamma_m$).

3.5.1 Model parametrization

The models we consider are essentially depth-dependent distributions of Vsv and Vsh, with Vp and density scaled to Vsv. Vsh and Vsv are related through equation (1), and we consider the shear wave speed part of the model specified by Vsv and γ, where $Vsh = (1+\gamma)Vsv$. We set Vph = Vpv and $\eta = 1$, which is physically unrealistic because Vs anisotropy would be accompanied by Vp anisotropy with $\eta \neq 1$ (e.g., Babuška and Cara, 1991; Erdman et al., 2013). However, as Xie et al. (2013) have shown, the effect of this assumption on estimates of Vs radial anisotropy is negligible.

Each vertical profile on the ~50 km spatial grid across the study region consists of a vertical stratification of three categories of structure: the sediments, the crystalline crust, and the upper mantle. The first category is the sedimentary basin, which is represented by three model parameters: thickness and Vsv at the top and bottom of the sediments. The Vsv values in the sediments increase linearly from the top to the bottom. We assume that the sediments are isotropic, so that Vsv=Vsh, except in the Colville Basin where it is necessary to introduce non-zero sedimentary anisotropy, γ_s. The second category is the crystalline crust, which is described by thickness (from the base of the sediments to Moho), four cubic B-splines with variable coefficients, and the intensity of crustal radial anisotropy, γ_c, which is non-zero outside the Colville Basin. The third category is the mantle. Vsv from the Moho to 200 km depth is determined with five cubic B-splines, while Vsh is found from γ_m which is constant with depth. For offshore locations, an additional water layer is added to the top of the model, with water layer thickness determined from the ETOPO-1 model (Amante & Eakins, 2009) and Vsv = Vsh = 0 km/s, Vp = 1.5 km/s, and density = 1.02 g/cm^3.

Once a Vsv model is constructed for testing, Vp is computed using Vp/Vsv = 2.0 in the sediments and Vp/Vsv = 1.75 in the crystalline crust and mantle. The density in the crust is determined from Vsv and Vp with the empirical relationship presented by Brocher (2005). In the mantle, however,

density is scaled from Vsv perturbations relative to 4.5 km/s with 10 kg/m^3 per 1 % velocity change following Hacker and Abers (2004).

We assume that radial anisotropy is vertically constant and non-zero in the mantle, γ_m. In the crust, our parameterization of anisotropy depends on sedimentary thickness because in regions with very thick sediments we are unable to estimate radial anisotropy reliably in the crystalline crust. The Colville Basin, identified by the dark blue contour in **Figure 3-3d**, is the region where the impact from the sediments on the estimation of crustal anisotropy is the most profound. Therefore, in the Colville Basin we allow there to be sedimentary anisotropy but no crustal anisotropy ($\gamma_s \neq 0, \gamma_c = 0$), and consider crustal anisotropy to be indeterminate. In regions outside the Colville Basin, we set sedimentary anisotropy to zero but allow anisotropy in the crystalline crust ($\gamma_s = 0, \gamma_c \neq 0$).

The result is that the anisotropic part of the model is fully described by two different values of γ everywhere, one for the crust (γ_s or γ_c) and the other for the mantle (γ_m). As we show in section 3.6.2.1, this simple parameterization in which the amplitude of radial anisotropy is constant either in the sediments or the crystalline crust and also in the upper mantle is sufficient to fit the data across the study region. However, this parameterization differs from the study of Xie et al. (2013), which found that substantial depth-variability of the strength of radial anisotropy was needed to fit the data in Tibet.

The shear Q values in the crust are fixed to the values in the ak135 model; namely, Q = 80 in the sediments and Q = 600 in the crystalline crust. With these values, there is little physical dispersion in the crustal shear modulus. Shear Q is fixed at 150 in the mantle for simplicity, which is similar to the choice by Shen & Ritzwoller (2016).

The resulting parameterization consists of 15 unknowns for each grid point: two for the sediments (Vsv), one for sediment thickness, four for the crystalline crust (Vsv), one for crustal thickness, five for the mantle (Vsv), and two for apparent radial anisotropy in order to find Vsh in the mantle and either the crystalline crust or sediments; i.e., either (γ_c, γ_m) or (γ_s, γ_m).

3.5.2 Prior distributions

The prior distribution used in the inversion involves variations around a reference model, which is a combination of the 1-D model ak135 (Kennett et al., 1995) with the 3-D CRUST-1.0 (Laske et al., 2013) model. The sedimentary and crustal thicknesses in the reference model are from CRUST-1.0, while the shear wave speeds in the crust and mantle are from ak135. The prior distribution defines a range of models around the reference model, where the range is determined from the parameterization of the model and the imposed constraints. The constraints we impose are of two types.

The first type of constraint is the allowed range of perturbations to the reference at each location, which prescribes the extent of model space explored in the Monte Carlo sampling. The allowed ranges on the 15 variables that define the 3-D model at each point are summarized in **Table 3-3**. For example, we allow there to be $\pm$ 50% perturbations around the reference model for crustal thickness, and $\pm$ 20% for the B-spline coefficients in the crust and mantle. We also allow sedimentary thickness to vary from 0 to twice the input thickness from CRUST-1.0, and large changes to Vsv in the sediments. Radial anisotropy in the crystalline crust, γ_c, and in the mantle, γ_m, range separately from $\pm$ 10%, although beneath the Colville Basin $\gamma_c = 0$. Sedimentary anisotropy, γ_s, beneath the Colville Basin can range from 0 to 25%, but is zero outside this basin.

The result is that there are very large bounds considered around the reference model for the location of interfaces, shear wave speeds, and values for apparent radial anisotropy.

Table 3-3 Specification of the prior distribution of models

Model parameters	Range
Sediment thickness	0-2 m_0 (km)
Crustal thickness	$m_0 \pm 0.5\ m_0$ (km)
Vs, top of sediment	0.2 – 2 (km/sec)
Vs, bottom of sediment	0.5 – 2.5 (km/sec)
B-spline coefficients, crust	$m_0 \pm 0.2\ m_0$ (km/sec)
Crustal anisotropy	± 10 %
B-spline coefficients, mantle	$m_0 \pm 0.2\ m_0$ (km/sec)
Mantle anisotropy	± 10 %

The second type of constraint involves explicit bounds imposed on aspects of each vertical model profile considered. There are eight prior constraints imposed in constructing candidate models allowed in the prior distribution. If a model profile is constructed that violates one of these constraints, it is rejected prior to computing data fit. (1) At jump continuities (base of the sediments, Moho), the jump is positive with depth for both Vsv and Vsh. (2) Both Vsv and Vsh in the crust are less than 4.3 km/sec at all depths. (3) Both Vsv and Vsh increase monotonically with depth in the crust, which we refer to this as the "monotonicity constraint". (4) At the top of the mantle, Vsv and Vsh are both less than 4.6 km/sec and greater than 4.0 km/sec. (5) At the bottom of the model, i.e., at 200 km depth, Vsv and Vsh both are greater than 4.3 km/sec. (6) Both Vsv and Vsh at all depths (0 – 200 km) are less than 4.9 km/sec. (7) Vsv and Vsh are both greater than 4.0 km/sec for depths below 80 km. (8) The difference at internal maxima and minima in Vsv in the mantle is less than 10 m/s. Together these constraints act to discourage vertical oscillations in the crust and mantle, as well as large non-physical excursions, and are hypotheses that we are testing. We should only infer a more complicated model if we cannot fit the data with these constraints in place.

Examples of prior distributions for several locations are shown with white histograms in **Figure 3-8**. The prior distributions of crustal and mantle radial anisotropy are nearly uniform, because there are no additional constraints applied to the them. The prior distributions for crustal thickness have a slight preference for smaller values, due to the monotonicity constraint (which ensures larger values of Vs deeper in the crust). The monotonicity constraint also tends to skew the prior distributions for Vsv and Vsh at 15 km and 100 km.

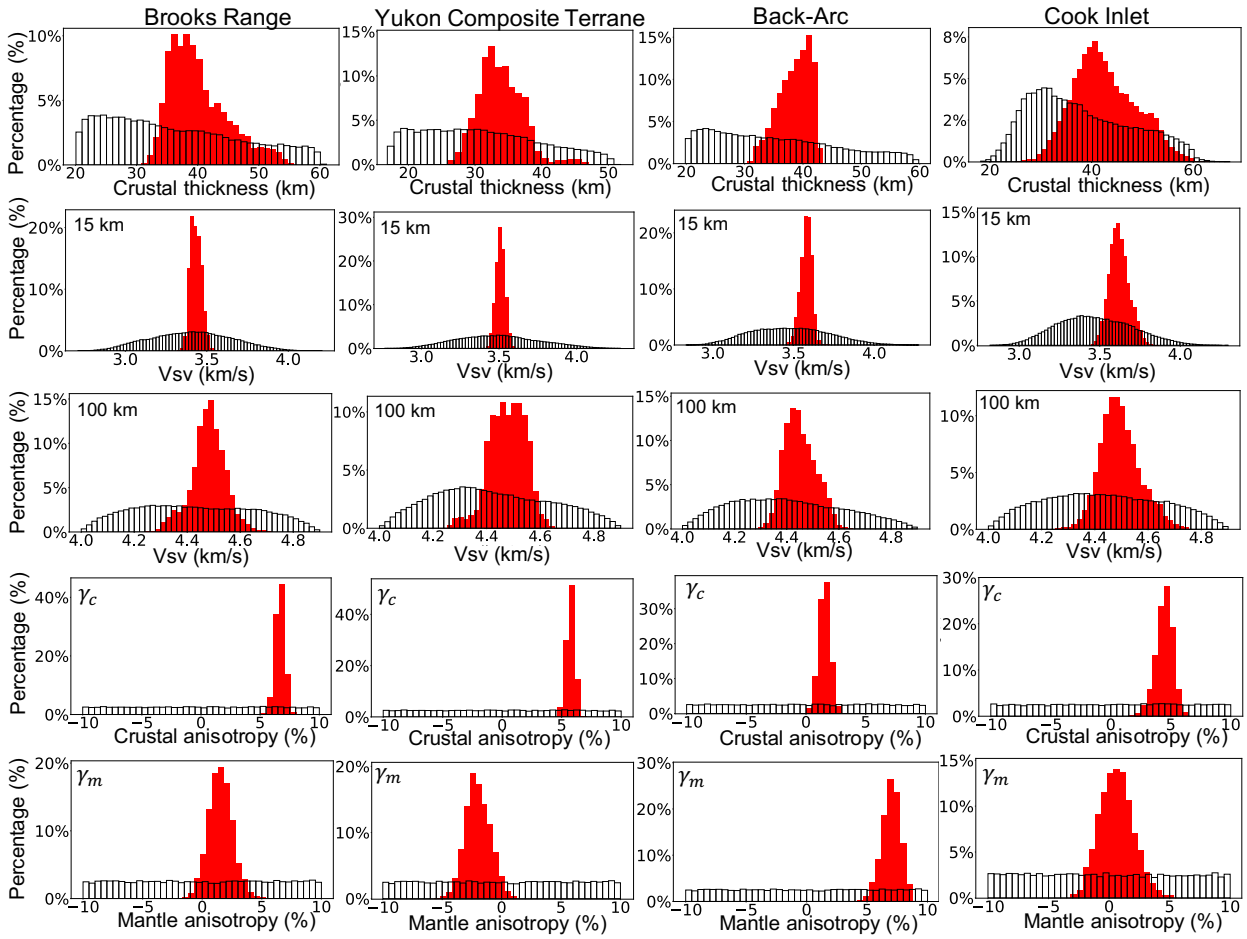

Figure 3-8 Examples of Prior and Posterior Distributions

Examples of the prior and posterior marginal distributions for five model variables: crustal thickness, Vsv at depths of 15 km and 100 km, and crustal and mantle anisotropy (γ_c,γ_m) for the four locations identified with yellow stars in Fig. 3-1 (Brooks Range, Yukon Composite Terrane, Aleutian Back-Arc, Cook Inlet). The prior distributions are shown with white histograms whereas the red histograms indicate the posterior distributions.

3.5.3 Posterior distributions

Posterior distributions of models are constructed based on data fit by the models chosen in the Monte Carlo sampling of model space, and reflect how well model characteristics are constrained by the data. As discussed earlier, a model is accepted into the posterior distribution if its misfit χ is less than $\chi_{\min} + 0.5$, where $\chi_{\min}$ is the misfit value for the best fitting model. The mean and standard deviation of the posterior distribution define the 3-D model (termed the mean model, $\bar{m}$) and the uncertainty estimates (σ_m). As argued by Shen and Ritzwoller (2016), σ_m is too large to provide a reasonable estimate of uncertainty, but does reflect relative uncertainty, which is useful to assess how well shear wave speeds and topography on internal interfaces are constrained by the data set.

Figure 3-7 shows examples of the mean model at two locations: beneath the Brooks Range where crustal anisotropy is non-zero and beneath the Colville Basin where sedimentary anisotropy is non-zero. These profiles illustrate that the resulting models are smooth in the crust and mantle, are monotonically increasing in the crust, have positive jumps in both Vsv and Vsh at the two discontinuities, and have depth-variable apparent radial anisotropy which is, however, constant in the mantle and sediments or crystalline crust.

Examples of marginal posterior distributions for the same four grid locations shown for the prior distributions are presented with the red histograms in **Figure 3-8**. These posterior distributions reveal that Vsv in the interior of the crust and mantle are relatively well constrained. In contrast, near the boundaries of the crust the posterior distribution widens. This is illustrated in **Figure 3-9**, which shows the standard deviation of the posterior distribution averaged over the study region as a function of depth. In the interior of the crust and in the mantle between depths of about 50 and 100 km, the standard deviation of the posterior distribution is about 50 m/s. Near the boundaries

in the crust the value more than doubles, and then it grows slowly at depths greater than 100 km. For this reason, we truncate the model and discuss its properties only to a depth of 120 km. **Figure 3-8** also shows that the posterior marginal distribution for crustal thickness is quite wide. Indeed, with surface wave data alone, internal interfaces in the Earth are typically poorly determined (e.g., Shen et al., 2016). The posterior distributions also indicate that crustal radial anisotropy, γ_c, tends to be better constrained than mantle radial anisotropy, γ_m.

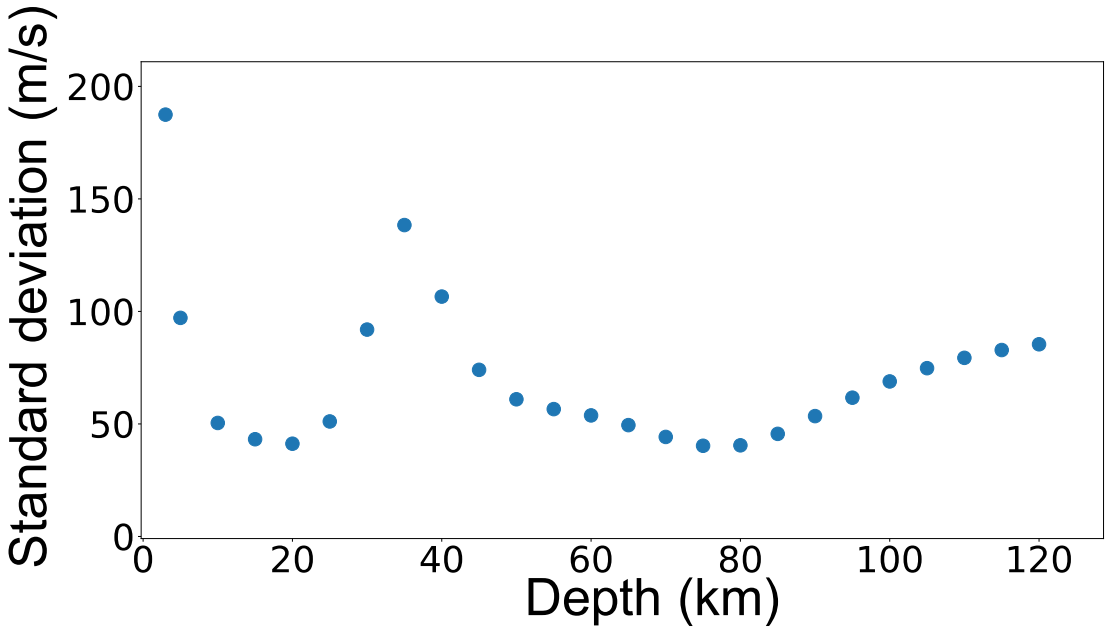

Figure 3-9 Standard Deviation vs. Depth

The standard deviation of the posterior distribution of Vsv presented as a function of depth averaged over the region of study.

Similar to Moschetti et al. (2010), we find that there is a trade-off between the values of radial anisotropy in the crust and mantle. As **Figure 3-10** illustrates, mantle radial anisotropy changes appreciably with changes in crustal radial anisotropy. At some locations, mantle radial anisotropy may not be required to fit the data, as illustrated by the points for the Brooks Range and the Cook Inlet in the marginal distributions of **Figure 3-8**, but at most locations crustal or sedimentary anisotropy is needed. We discuss this further in section 3.7.

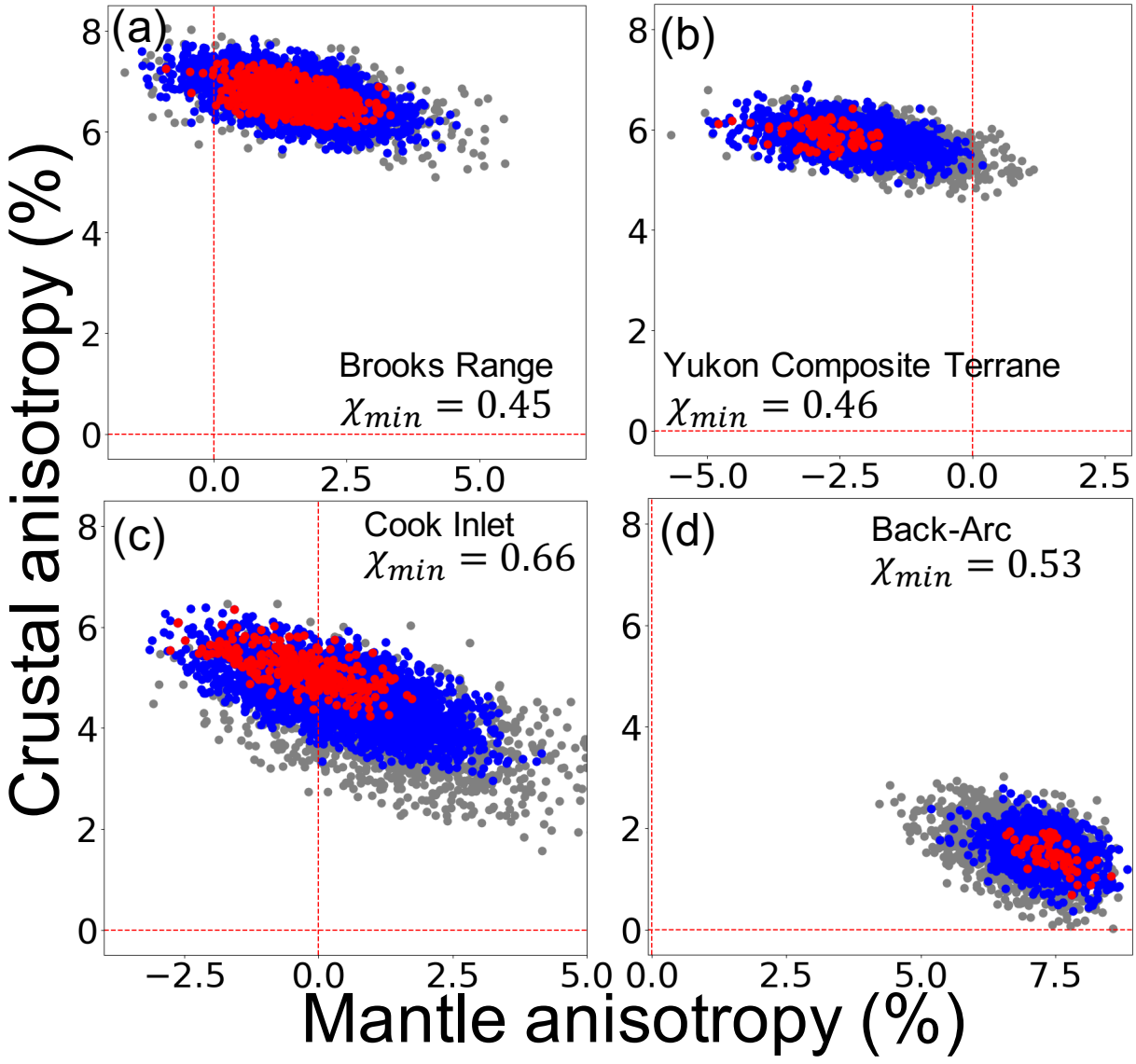

Figure 3-10 Crustal and Mantle Anisotropy Trade-offs

Trade-offs between crustal and mantle anisotropy (γ_c, γ_m) at the four locations identified with yellow stars in Fig. 3-1: (a) Brooks Range, (b) Yukon Composite Terrane, (c) Cook Inlet, and (d) Aleutian Back-Arc. Symbol color indicates misfit χ from each of the accepted models, defined by equation (3). Red: $\chi < \chi_{\min} + 0.2$, Blue: $\chi_{\min} + 0.2 \le \chi < \chi_{\min} + 0.3$, Grey: $\chi_{\min} + 0.3 \le \chi < \chi_{\min} + 0.5$, where $\chi_{\min}$ is the misfit from the best-fitting model at each location, which is labeled on each panel.

3.6 Results

As described above, the mean model at each grid point ($\bar{m}$) as a function of depth and for the depth to each interface is mean of the posterior distribution, which defines the 3-D Vsv model as

well as the amplitude of radial anisotropy in the crust (γ_c) or sediments (γ_s) and the mantle (γ_m). The standard deviation of the posterior distribution (σ_m) provides a conservative estimate of uncertainty (e.g., Shen and Ritzwoller, 2016). Here, we discuss the characteristics of the 3-D model for isotropic structure and radial anisotropy.

3.6.1 3-D isotropic model: Vsv

Figure 3-11a shows the sedimentary thickness estimates of the mean model. Clearly, the Colville Basin in the Alaskan north slope region is the most significant basin, but other basins are also resolved in the model and are labeled with numbers in **Figure 3-11a** and identified in **Table 3-4.** Sedimentary thickness is quite uncertain due to the trade-off with upper crustal shear-wave speeds. Shear wave speed at the top of the crystalline crust is also affected by this trade-off, as the uncertainties in **Figure 3-9** illustrate.

The shear wave speed distribution (Vsv) averaged from the surface of the Earth to a depth of 6 km is presented in **Figure 3-11b**. This depth-range also displays the imprint of the basins where they exist, but where basins do not exist it provides an estimate of crustal wave speed in the upper crystalline crust. This figure and those at other depths present slices over a similar depth range ($\pm$ 3 km).

In the middle crust, near 20 km depth (**Fig. 3-11c**), the model is better determined than nearer to the surface, due to fewer trade-offs away from interfaces. However, uncertainty increases dramatically when Moho depth approaches 20 km, which it does near the southern edge of the study region. There is a prominent low velocity lineation running near the major faults bounding the Brooks Range. A low velocity anomaly at this depth also appears near the Chugach-Prince William terrane, in the middle of the Yakutat microplate which is identified by the white polygon

in the figure, and near the Wrangell volcanic field. High velocity anomalies are observed in the crust above the subducting Alaska-Aleutian slab and beneath the North American craton.

Near the bottom of the crust (**Fig. 3-11d**), the lateral variability of Vsv is weaker, except for small regions off-shore where the crust is thinner than on the continent. Lowest velocities (3.70 – 3.75 km/s) onshore run near the major faults bounding the Brooks Range, as they do at 20 km depth, and in the Wrangell volcanic field. The highest velocities (above 3.95 km/s) are found in the interior of the state and in Arctic-Alaska and the North American craton in northern Canada. Uncertainty increases in the lowermost crust because of trade-offs with Moho depth, as **Figure 3-9** shows.

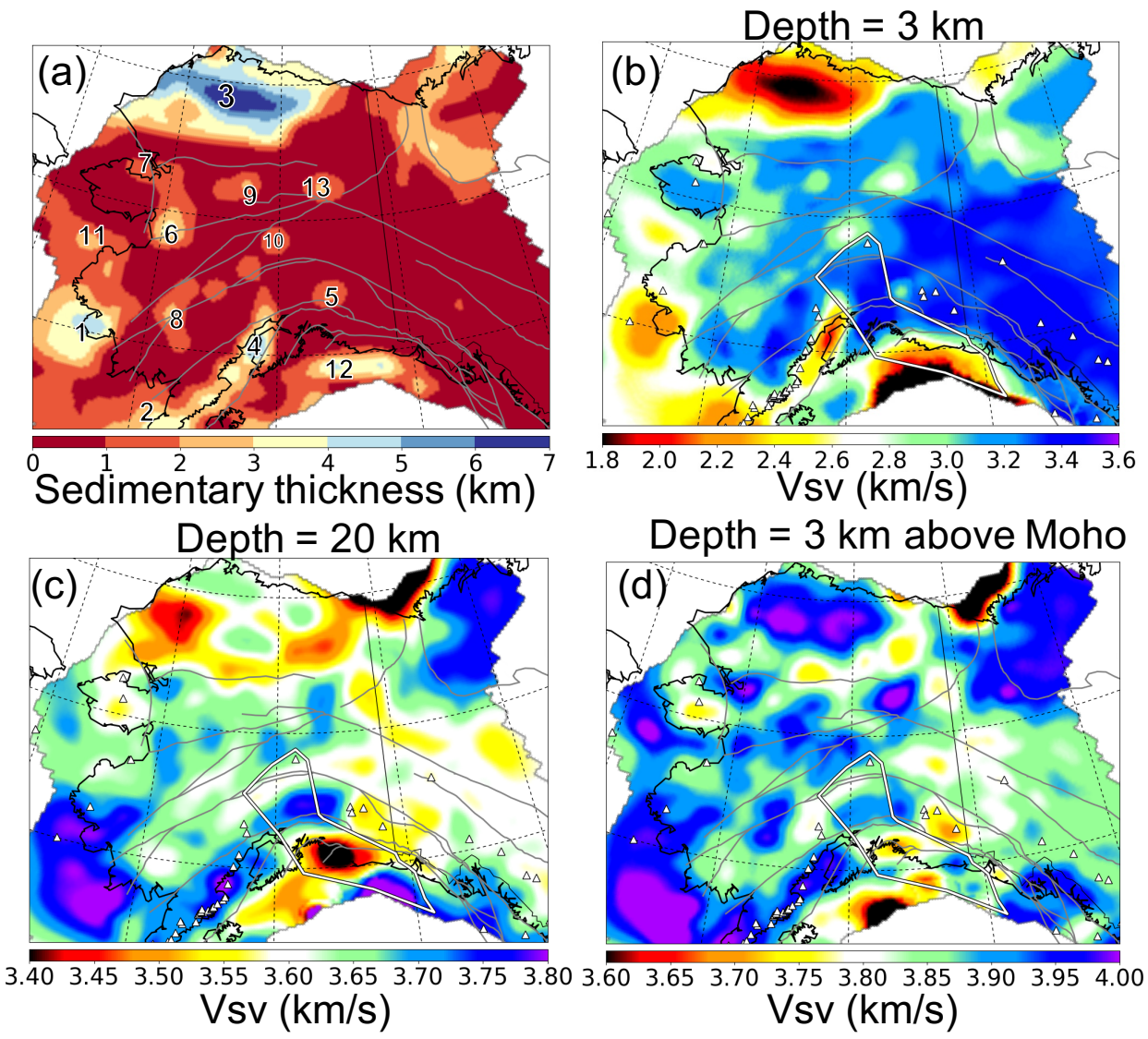

Figure 3-11 Crustal Structure Maps

(a) Sedimentary thickness constructed with the mean of the posterior distribution of models, where the numbers and Table 3-4 identify basin names. (b) – (d) The mean of the posterior distribution of Vsv for three depth ranges in the crust (central-depth ± 3 km) with central-depths of: (b) 3-km, (c) 20-km and (d) 3 km above Moho. Grey lines are major faults, the white polygon outlines the hypothesized Yakutat terrane, and triangles indicate volcanoes.

Table 3-4 Names of sedimentary basins identified with numbers

Index	Name of the sedimentary basin
1	Bethel Basin
2	Bristol Bay Basin
3	Colville Basin
4	Cook Inlet Basin
5	Copper River Basin
6	Galena Basin
7	Hope Basin & Kotzbue Basin
8	Holtina Basin
9	Kobuk-Koyuku Basin
10	Nenana Basin
11	Norton Basin
12	Yakutat Basin
13	Yukon Flats Basin

Crustal thickness estimates are presented in **Figure 3-12a** and one standard deviation of the posterior distribution in **Figure 3-12b**. Crustal thickness is typically poorly constrained by surface wave dispersion data alone, and uncertainties are fairly uniform geographically, averaging about 4 – 5 km. Nevertheless, our crustal thickness estimates differ substantially from the reference model (**Fig. 3-12c),** but are similar to those of Miller & Moresi (2018) based on receiver functions (**Fig. 3-12d)**. Details differ but the large-scale features are similar. Notably, and unsurprisingly, the crust is thicker beneath the Brooks Range and the Alaska Range while it is thinner in the interior of Alaska; e.g., the Yukon Composite Terrane. **Figure 3-13** shows a histogram of differences between our model and that of Miller & Moresi (2018), where the mean difference is about 1.5 km (Moho in our model is on average a bit shallower) and the standard deviation of differences is about 3.4 km. Thus, the mean difference between the models is within one standard deviation of the posterior distribution, presented in **Figure 3-12b.**

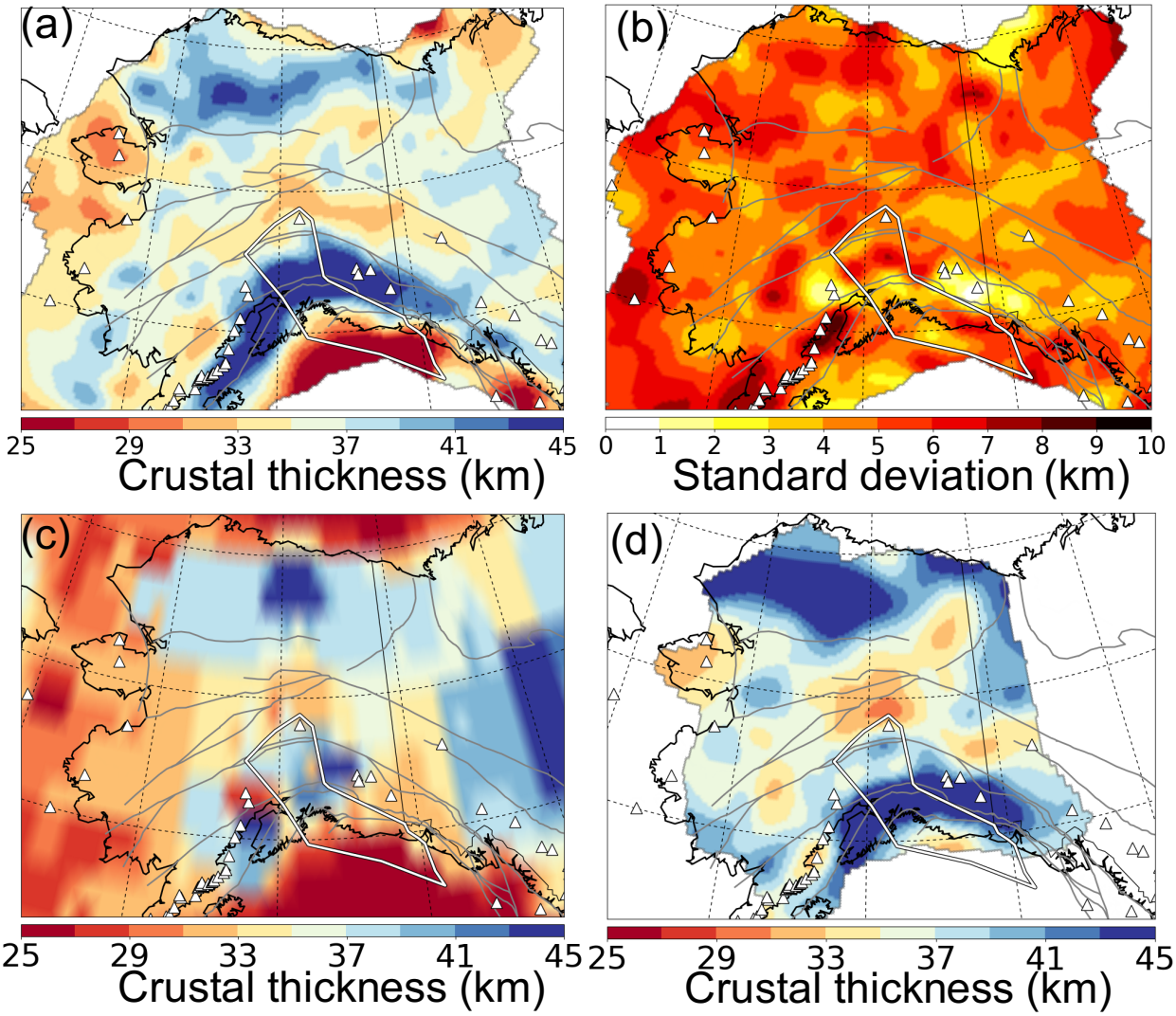

Figure 3-12 Crustal Thickness Maps

(a) Crustal thickness map constructed from the mean of the posterior distribution of models at each point. (b) Corresponding uncertainties of crustal thickness: standard deviation of the posterior distribution. (c) Crustal thickness from the Crust-1.0 model (Laske et al., 2013), which is part of the reference model used to define the prior distribution. (d) Crustal thickness estimated by Miller & Moresi (2018) using receiver functions, downloaded from https://github.com/lmoresi/miller-moho-binder .

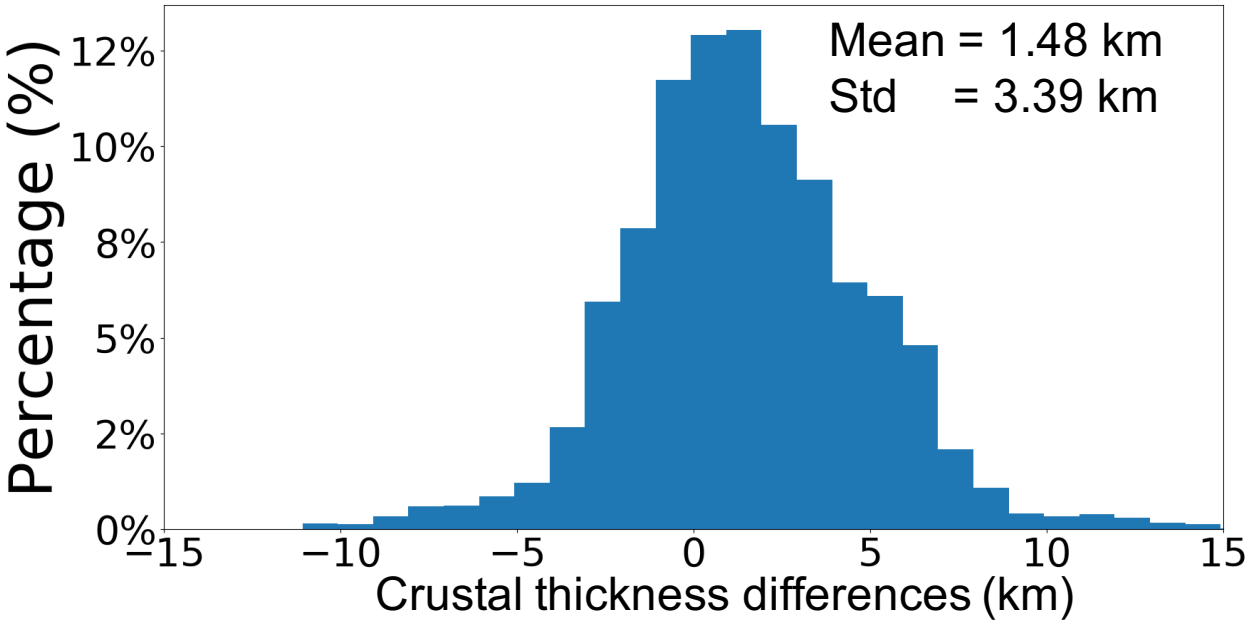

Figure 3-13 Differences in Crustal Thickness

Histogram of differences in crustal thickness between our model and that of Miller & Moresi (2018), taken at grid-points where both models exist. The mean difference and standard deviation of the differences are listed.

Two horizontal Vsv slices of the mean model are shown in **Figure 3-14** at depths of 60 km and at 100 km in the mantle. The most prominent positive anomalies are the cratonic roots beneath Artic-Alaska and the North American craton. The edge of the velocity anomaly in Canada forms the so-called Cordillera-Craton boundary. In the interior of Alaska, the mantle is mostly a broad relative low velocity zone. High topography of the Brooks Range, the Alaska Range, and other ranges are not underlain uniformly by low velocity uppermost mantle, which has implications for the nature and depth extent of isostasy (e.g., Levandowski et al., 2014). The Wrangell volcanic field at 60 km is underlain by low velocities in the mantle, particularly offset north of the volcanoes. The back-arc area northwest of the Alaska-Aleutian subduction zone displays low velocity features in the supra-slab wedge that encompass the volcanoes at 60 km depth but which is offset further to the northwest at greater depths. Subducting lithosphere is imaged clearly at 100 km, but at 60 km

it is mainly offshore along the Alaska-Aleutian subduction zone and not as well resolved. The nature of subducting lithosphere in the 3-D model is discussed in greater detail in section 3.7.

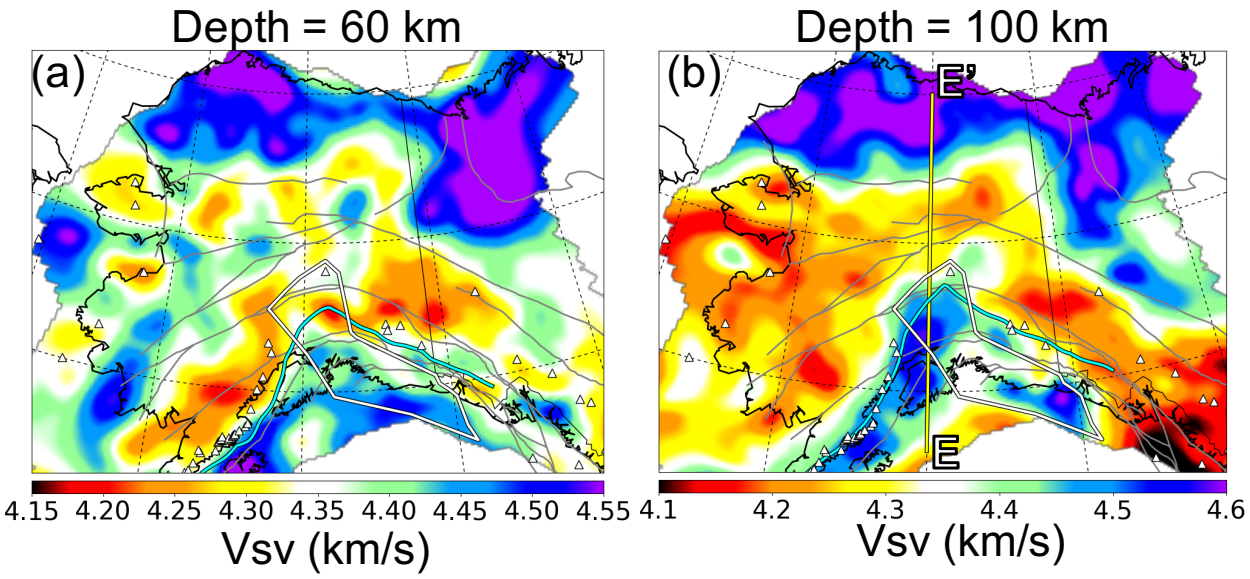

Figure 3-14 Mantle Structure Maps

The mean of the posterior distribution of Vsv models at two depth ranges in the mantle (central-depth ± 3 km) with central-depths of: (a) 60-km and (b) 100-km. Symbols are similar to Fig. 3-11, but additionally the cyan curve is the top edge of the subducting slab at each map depth from the slab model of Jadamec & Billen (2010) and the lines E-E' identifies the vertical profile shown in Fig. 3-21.

3.6.2 3D model of radial anisotropy: γ_c, γ_m

3.6.2.1 Data fit as a function of model parameterization

Data misfit, defined by equation (3), for various models is shown in **Figure 3-15**. For the data to be considered fit well, a value of misfit below about 2.0 should be achieved. **Figure 3-15a** shows the misfit for the isotropic model, in which Vsh = Vsv so that $\gamma_s = \gamma_c = \gamma_m = 0$. This map reveals the Rayleigh-Love discrepancy. Across most of Alaska the Rayleigh and Love wave dispersion data cannot be fit simultaneously with an isotropic model, and average misfit (eqn. (3)) is 2.41.

As discussed in section 3.5.3, there is a substantial trade-off between crustal and mantle anisotropy that broadens the posterior distribution for both γ_c and γ_m, but reliable simultaneous estimates of

these variables are possible in most places. However, due to the exceptionally large anisotropy, γ_s, in the Colville Basin we cannot estimate γ_c reliably. In this basin, we allow anisotropy in the sediments and mantle but not in the crystalline crust (i.e., $\gamma_c = 0, \gamma_s \neq 0 \neq \gamma_m$), but outside the basin the model includes anisotropy in the crystalline crust and mantle but not the sediments (i.e., $\gamma_s = 0, \gamma_c \neq 0 \neq \gamma_m$). The resulting data misfit is shown in **Figure 3-15b**. With the model including mantle and crustal (or sedimentary) radial anisotropy, the data can be fit across the entire region of study with an average misfit of 0.78.

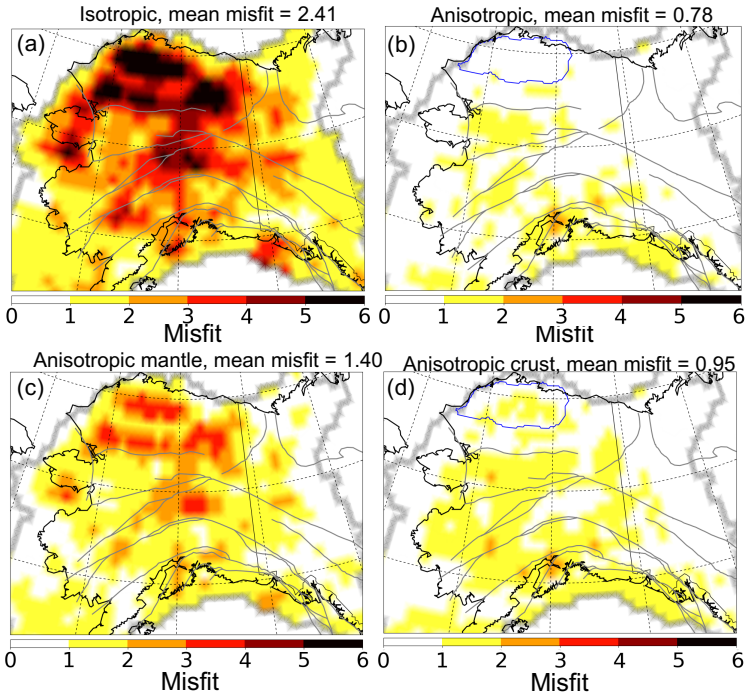

Figure 3-15 Misfit Maps

Misfit (defined by eqn. (3)) for the mean of posterior distribution of accepted models for different specifications of apparent radial anisotropy. (a) Isotropic model ($\gamma_s = \gamma_c = \gamma_m = 0$); inversion is performed using Rayleigh wave data alone. (b) Our final model based on both Rayleigh and Love wave data, including crustal and mantle anisotropy outside of the Colville Basin ($\gamma_s = 0, \gamma_c \neq 0 \neq \gamma_m$) and sedimentary and mantle anisotropy inside the Colville Basin ($\gamma_c = 0, \gamma_s \neq 0 \neq \gamma_m$). The Colville Basin is outlined in Fig. 3-3d. (c) The model is based on both Rayleigh and Love wave data and includes mantle anisotropy but no sedimentary or crustal anisotropy ($\gamma_s = 0 = \gamma_c, \gamma_m \neq 0$). (d) The model is based on both Rayleigh and Love wave data and includes crustal or sedimentary anisotropy but no mantle crustal anisotropy ($\gamma_m = 0, \gamma_c \neq 0$ or $\gamma_s \neq 0$). The mean of the misfit across each map is labeled at the top of each panel.

Without sedimentary or crystalline crustal anisotropy but including mantle anisotropy ($\gamma_s = \gamma_c = 0, \gamma_m \neq 0$), the misfit is shown in **Figure 3-15c**. The average misfit is 1.40, and across much of Alaska there is a large residual misfit, particularly in the parts of the state north of the Denali fault. This includes the Colville basin, as well as the area along the Brooks Range and the region between the Denali and Tintina faults focused broadly on the Yukon Composite Terrane. Thus, to achieve acceptable data fit, crustal anisotropy must be introduced in the crystalline crust or the sediments of the Colville Basin. **Figure 3-15d** presents the misfit from the inversion that includes sedimentary or crustal anisotropy but not mantle anisotropy (i.e., $\gamma_m = 0, \gamma_s \neq 0$ or $\gamma_c \neq 0$). The misfit value drops dramatically when introducing crustal anisotropy (from 1.40 to 0.78) and increases only moderately when turning off mantle anisotropy (from 0.78 to 0.95). Thus, the primary factor that determines data fit is actually crustal anisotropy (and in Colville Basin sedimentary anisotropy). Mantle anisotropy can be determined reliably even though its effect on the Rayleigh-Love discrepancy is weaker.

Figure 3-16 illustrates in greater detail the improvement in fitting the Rayleigh-Love discrepancy. The error bars in this figure are for differences in observed Love wave phase speed and Rayleigh wave phase speed at four locations for our final model ($\gamma_m \neq 0, \gamma_c \neq 0$ or $\gamma_s \neq 0$). The dashed line indicates the fit to this difference based on the isotropic model at each location, where Vsv = Vsh ($\gamma_s = \gamma_c = \gamma_m = 0$). There are large period-dependent discrepancies between the line predicted by the isotropic model and the observations. Beneath the Brooks Range and Cook Inlet, the discrepancy is approximately constant across period, implying that radial anisotropy is probably about the same in both the crust and mantle. In contrast, in the Aleutian Back-Arc region the discrepancy is larger at longer periods so that mantle anisotropy is probably stronger than crustal anisotropy, and in the Yukon Composite Terrane the discrepancy is greater at shorter periods

indicating that crustal anisotropy is probably larger than mantle anisotropy there. In each of these cases, introducing radial anisotropy that is constant with depth separately in the crust and mantle, allows the data to be fit well.

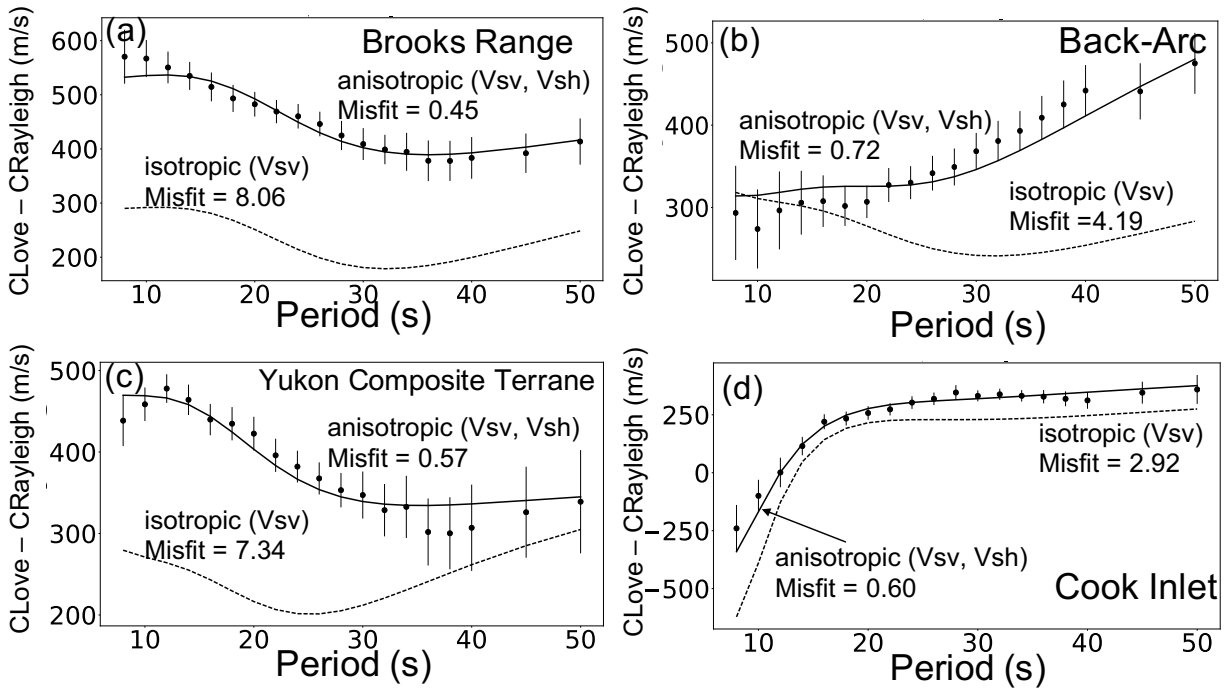

Figure 3-16 Sample Love-Rayleigh Difference Curves

Examples of differences in phase speed between Love and Rayleigh waves at four locations identified with yellow stars in Fig. 3-1: (a) Brooks Range, (b) Aleutian Back-Arc, (c) Yukon Composite Terrane, and (d) Cook Inlet. The error bars are standard deviation uncertainties of the differences between Love and Rayleigh wave phase speeds. The solid lines are the predictions from the mean of the posterior distribution of our final radially anisotropic model ($\gamma_m \neq 0, \gamma_s \neq 0$ or $\gamma_c \neq 0$) and the black dashed lines are from the isotropic Vsv model ($\gamma_s = \gamma_c = \gamma_m = 0$). Misfit values from the isotropic and anisotropic models, defined by eqn. (3), are indicated on each panel.

3.6.2.2 The model of apparent radial anisotropy

The resulting estimates of crustal and mantle anisotropy are shown in **Figure 3-17**. We consider estimates of γ_c to be indeterminate if the standard deviation of the posterior distribution for γ_c is greater than 1.0% or in the Colville Basin where we estimate γ_s rather than γ_c. Estimates of γ_m

are considered indeterminate if the standard deviation of the posterior distribution is greater than 1.5%. γ_m has a weaker impact on the Rayleigh-Love discrepancy than γ_c, so we make the tolerance broader for mantle anisotropy than for crustal anisotropy.

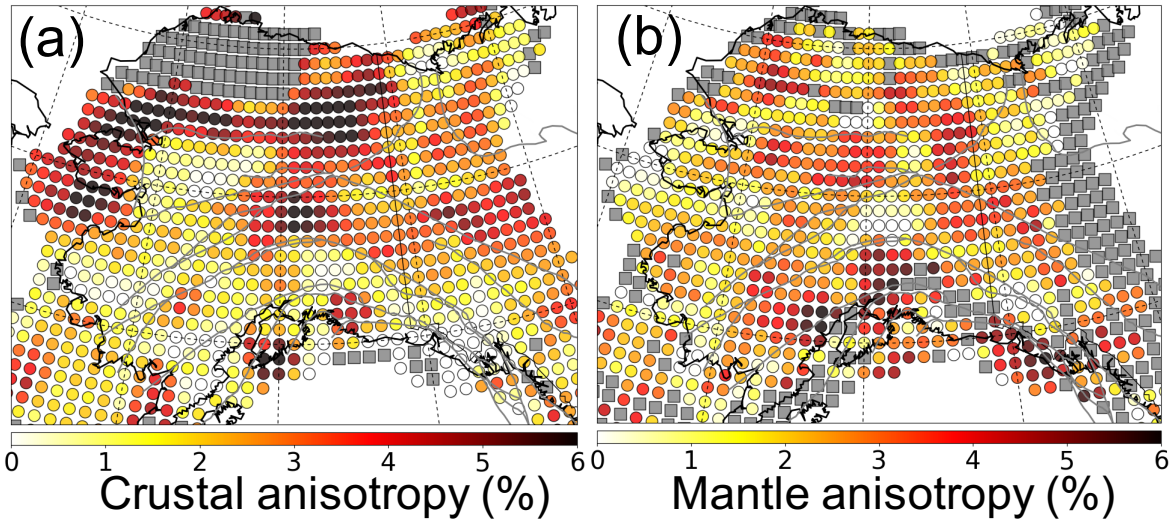

Figure 3-17 Apparent Radial Anisotropy Maps

Apparent (a) crustal (γ_c) and (b) mantle (γ_m) radial anisotropy determined from the mean of the posterior distribution using both Rayleigh and Love wave data. The grey squares are grid nodes where we are not confident in the estimate of anisotropy. This includes the whole of the Colville Basin for crustal anisotropy.

Crustal anisotropy is on average stronger than mantle anisotropy and more geographically variable. Mantle anisotropy is somewhat more homogeneous than crustal anisotropy, and the patterns of crustal and mantle anisotropy are generally complementary. In this latter respect, crustal and mantle anisotropy may have formed in response to different episodes of tectonic strain. In particular, the geographical distribution of crustal anisotropy corresponds in part to areas of significant crustal extension, as discussed further in section 3.7.3.

3.7 Discussion

3.7.1 Radial anisotropy of the Colville Basin

The North Slope foreland basin, or the Colville Basin or trough, is a late Mesozoic and Cenozoic basin that runs from the Brooks Range in the south to the edge of the Beaufort Sea in the north (e.g., Bird and Molenaar, 1992). The basin is about 1000 km long and 50 to 350 km wide, and is by far the largest basin in the region of study. We approximate its extent with the 2.5 km/s contour on the 10 s Rayleigh wave group speed map (**Fig. 3-3d**).

As indicated by the Vsv and Vsh profiles shown for a point in the Colville Basin in **Figure 3-7b**, the radial anisotropy in the sediments of the basin is much stronger than across the crystalline crust. Values of sedimentary apparent radial anisotropy average in excess of 20 % throughout the basin, similar to the large values reported by Xie et al. (2013) for the Sichuan Basin. The stratification and layering found in sedimentary basins probably generate this strong radial anisotropy. Our model cannot provide information about the layering of structures in basins, but we are confident that the anisotropy (γ_s) in the Colville Basin is exceptionally strong, much stronger than either crustal or mantle radial anisotropy (γ_c, γ_m). Additional data, such as receiver functions or Rayleigh wave H/V ratio, which are more sensitive the shallowest parts of the Earth and also provide better constraints on sediment thickness, may help to improve sedimentary structures, helping to provide better information about sedimentary anisotropy.

3.7.2 Resolved subducted lithosphere

Resolving subducted lithosphere including accurately capturing the geometry of the subducting slab, its thickness, and the amplitude of velocities in the slab is very challenging for inversions based on surface wave data alone for the following reasons. (1) Surface waves in general have better depth resolution than horizontal resolution. Consequently, the ability to determine

lithospheric thickness varies with the dip angle of the slab. Slab thickness is better constrained when the lithosphere is horizontal, but as the dip angle increases the ability to determine slab thickness degrades appreciably. (2) A particular complication for our study is that a significant part of the Alaskan subduction zone is located at the southern edge of our model, which is offshore with poor path coverage for ambient noise data and no data coverage for earthquakes. Therefore, at least offshore, we lack dispersion measurements at the longer periods (indicated in **Fig. 3-3**), which reduces confidence in structures deeper than about 100 km. Shorter period dispersion measurements are also affected by reduced data coverage, which makes it harder to recover the amplitude of velocity anomalies correctly. Despite these issues, aspects of the subducting lithosphere at depths above about 100 km can be resolved reliably. In particular, we are able to resolve the top of the subducting slab above 100 km depth and its areal extent, especially in on-shore regions. **Figure 3-18** indicates some of these features.

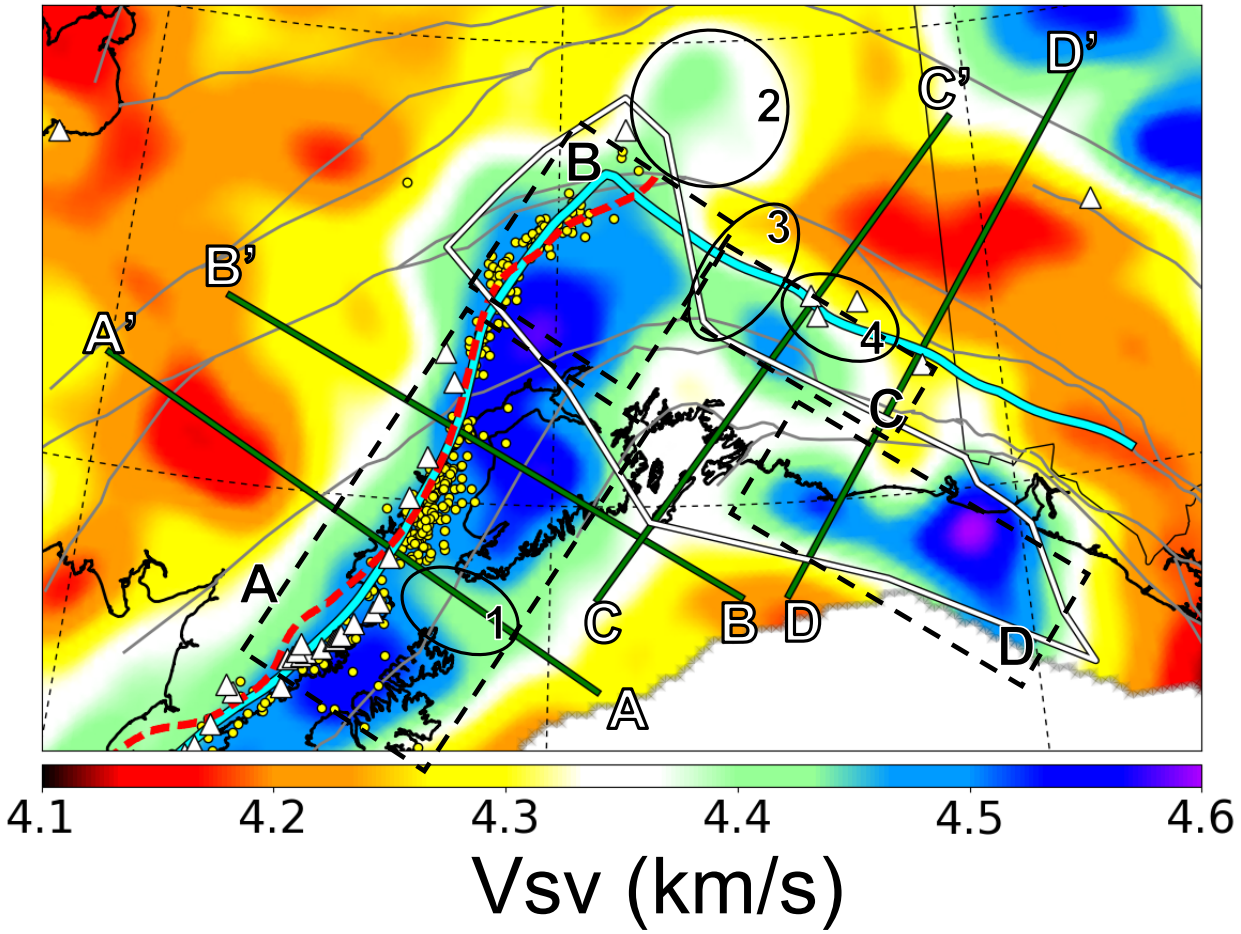

Figure 3-18 Blow up of Vsv Slice at 100 km

Blow up of the Vsv slice at 100 km with labels indicating different features of the subduction zone. Grey lines are major faults and the white contour outlines the hypothesized Yakutat Terrane. The cyan curve is the location of the edge of the subducting slab at 100 km depth from the slab model of Jadamec & Billen (2010) and the red dashed line delineates 100 km depth contour from the model Slab 1.0 (Hayes et al., 2012). The yellow dots indicate the locations of earthquakes from 1991 Jan to 2015 Oct (from ISC catalog) at depths from 95 – 105 km. Several tectonic features are identified with letters and numbers: A – Aleutian subduction zone; B – Alaskan subduction zone and slab kink which includes the Denali volcanic gap, C – Yakutat subduction zone, D – Yakutat slab shoulder. The numbered ovals indicate: 1 – the Barren Islands slab anomaly 2 – the aseismic slab edge, 3 – the Wrangellia slab anomaly and 4 – the Wrangell volcanic field. Vertical profiles A-A', B-B', C-C', and D-D' are shown in Fig. 3-19.

To illuminate the well resolved features, we begin by comparing our 3-D Vsv model (mean of the posterior distribution) with two prominent slab models that delineate Alaskan subduction zones: Slab1.0 by Hayes et al. (2012) and the Alaska_3D 1.0 model by Jadamec & Billen (2010). These

two models are generally consistent in depicting the Alaska-Aleutian subduction zone comprising dashed boxes A and B in **Figure 3-18**, which we call Blocks A and B. Slab edges from these model at 100 km depth are presented in this figure with the dashed red and solid cyan curves. However, unlike Slab1.0, the Alaska_3D 1.0 model also includes a slab kink near the Denali fault and the northern-most edge of the Denali volcanic gap, and the slab extends into what we refer to as the Yakutat subduction zone in Block C and beyond. Because our 3-D model also includes the slab kink (**Fig. 3-18**) near the Denali fault (Block B) and the subducting Yakutat slab (Block C) we will concentrate comparison of our model with Alaska_3D 1.0.

Following the cyan slab edge curve at 100 km depth from the west to the east in **Figure 3-18**, we divide the Alaskan subduction zone into four structurally distinct blocks: Blocks A - D. They are identified with letters in **Figure 3-18** as (A) the Aleutian subduction zone, (B) the Alaskan subduction zone and slab-edge or kink, which includes the Denali volcanic gap, (C) the Yakutat subduction zone, and (D) the Yakutat slab shoulder.

In the Aleutian subduction zone (Block A), the edge of the high velocity Pacific slab is consistent with the slab edge curves of both the Slab 1.0 and Alaska_3D 1.0 model. The location of the slab in our model also generally matches the locations of the Aleutian volcanic arc (white triangles) and earthquakes in the depth range near 100 km (yellow dots). We also note that there is an anomaly in slab structure (identified as Oval 1 in **Fig. 3-18**) located near the Barren Islands in the strait between the Kenai Peninsula and Kodiak Island. This is what we call the “Barren Islands slab anomaly”, which is a notable reduction in shear wave speed at 100 km depth and occurs in a region of heightened seismicity at this depth. Profile A-A’ in **Figure 3-19** extends across the Barren Islands anomaly and shows the anomaly in cross-section (black oval labeled with the number 1 in the A-A’ cross-section) as a reduction in shear wave speed in a confined depth range

that occurs adjacent to very slow velocity supra-slab wedge in the back-arc. In contrast, profile B-B' in **Figure 3-19** extends through a more normal section of the subducting lithosphere, in which no low velocity anomaly appears and the back-arc is not as slow. Yang & Gao (2019) also report a low velocity region in the uppermost mantle near the Barren Islands and refer to it as a "slab gap" characteristic of horizontal slab segmentation and perhaps a slab tear. In contrast, we image this as a vertically confined anomaly, so we do not refer to it as a gap and do not image a structure that is consistent with slab segmentation or a tear that extends across a significant depth range. Consequently, we hypothesize that the Barren Islands slab anomaly reflects slab heating caused by higher temperatures and perhaps fluid or melt in the back-arc region localized near 100 km depth. However, the Barren Islands slab anomaly may result from failing to recover the full amplitude of the positive anomaly within the slab. Further efforts are warranted to improve the vertical and horizontal resolution of this intriguing lithospheric feature in order to clarify its physical cause.

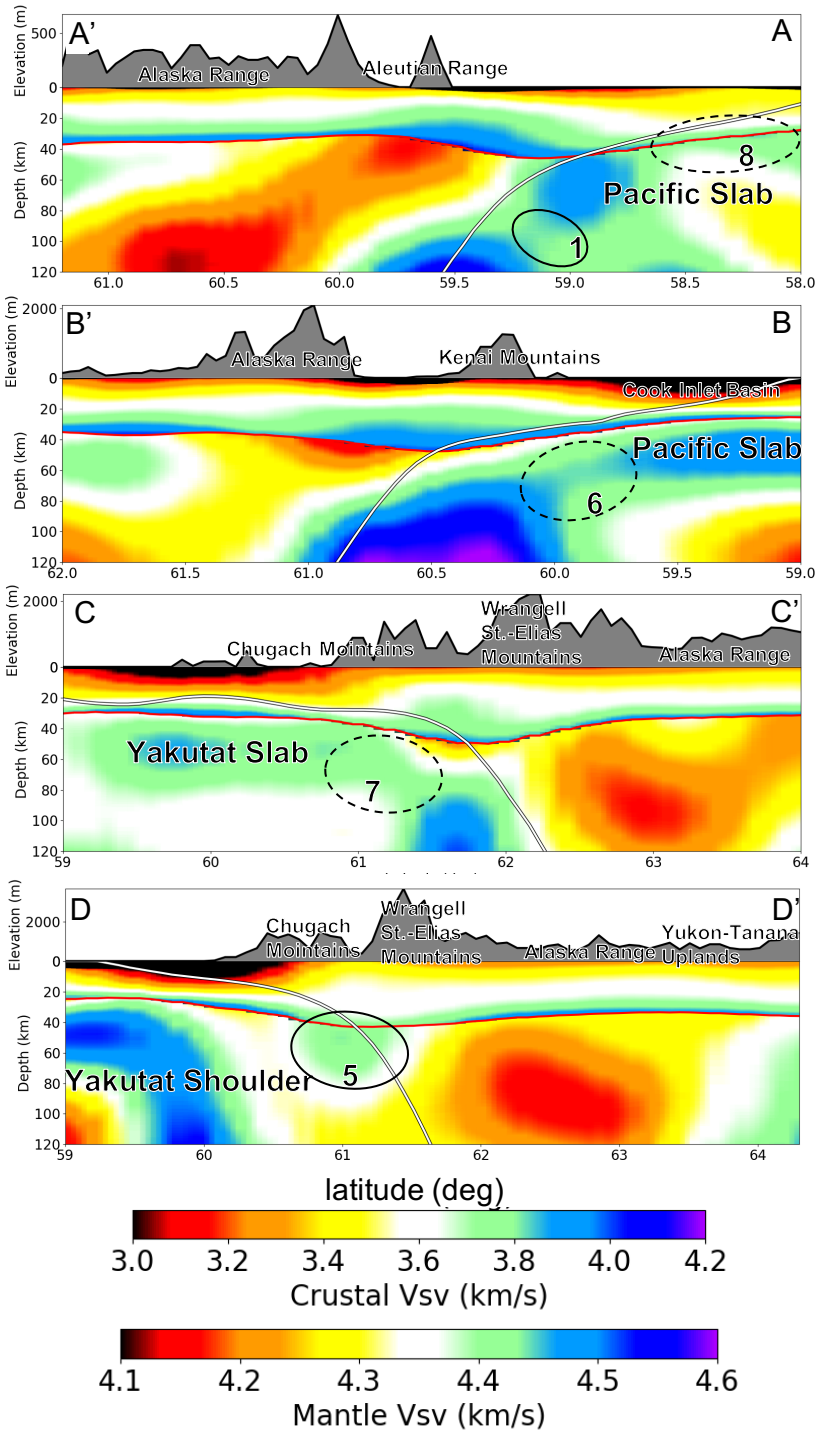

Figure 3-19 Vertical Cross Sections

Vertical cross sections A-A', B-B', C-C' and D-D' identified in Fig. 3-18. The white lines in the cross-sections identify the upper edge of the subducting lithosphere in the model of Jadamec and Billen (2010). The black oval numbered 1 in profile A-A' is the Barren Islands slab anomaly and other ovals are defined in the text. Dashed oval identify features we do not interpret and the solid ovals are features we do interpret.

The Alaskan subduction zone ends northward to a slab edge or kink, which is identified as the edge of Block B in **Figure 3-18**. Rondenay et al. (2010) propose that the Denali Volcanic Gap is caused by the cooling effect of the Yakutat slab, which essentially reduces melt production and hinders magma ascent to the surface. We observe high shear wave speed lithosphere beneath the Denali Volcanic Gap region, consistent with Jiang et al. (2018) and Martin-Short et al. (2018). Others have argued that the kink structure may result in toroidal mantle flow around it, and the flow pattern predicted by the geodynamical model of Jadamec & Billen (2010) is consistent with SKS splitting studies (e.g., Christensen & Abers, 2010; Hanna & Long, 2012; Perttu et al., 2014).

Oval 2 located northeast of Block B in **Figure 3-18** is a high velocity extension to the slab edge, which was suggested to be an aseismic slab edge by Gou et al. (2019). This aseismic slab edge has also been imaged by Jiang et al. (2018).

Moving eastward along the slab edge from the slab kink to the Yakutat subduction zone, Block C in **Figure 3-18**, there is another relative low velocity anomaly (Oval 3) located northwest of the Wrangell Volcanic Field (Oval 4). This "Wrangellia slab anomaly", as we call it, is also captured by the Vp model of Gou et al. (2019) at a similar depth range. The vertical cross section C-C' in **Figure 3-19** shows that the high-speed anomaly in Block C appears to be part of the subducting Yakutat slab and occurs at the location of the slab in model Alaska_3D 1.0. Jiang et al. (2018) suggest that this part of the slab is sinking vertically because the subduction is slowed down by the Yakutat collision. The presence of this high-speed subducted lithosphere at a similar location is also reported by Martin-Short et al. (2018) and Gou et al. (2019).

As illustrated in **Figure 3-18**, there is an increasing mismatch in slab geometry between our model and Alaska_3D 1.0 as the edge of Yakutat slab extends southeastward into what we refer to as the

"Yakutat slab shoulder" region (Block D). The corresponding vertical cross-section D-D' in **Figure 3-19** shows a high-speed anomaly seaward of the Chugach Mountains rather than near the slab edge predicted by the model Alaska_3D 1.0. This anomaly is separated from another high-speed anomaly identified by Oval 5 in D-D', which is in the slab shoulder region of the Yakutat slab. It is not clear whether this detachment indicates thickened lithosphere of the Yakutat terrane or the onset of subduction further south of what the Alaska_3D 1.0 model predicts. This high-speed Yakutat slab shoulder has not been reported in previous studies.

In closing, we note several features that appear in the vertical cross-sections that we do not feel justified interpreting. (1) The amplitudes of the high-speed anomalies weaken where the slab begins to subduct in cross-sections B-B' and C-C', marked with Ovals 6 and 7. This may be due to the difficulty in recovering amplitudes correctly due to poor data coverage at those locations, which reduces our confidence in these features. (2) The slab thickens and the slab edge increasingly mismatches the Alaska_3D 1.0 model below 100 km depth on vertical cross-sections A-A' and particularly B-B', which we believe are artifacts caused by degradation in resolution with depth. Introducing body wave datasets may potentially help better resolving the deeper part (>100 km) of the subduction zone, which is beyond the scope of this study. (3) Oval 8 in profile A-A' is an off-shore region where we are unable to resolve uppermost mantle structure reliably.

3.7.3 Extensional provinces and radial anisotropy

Crustal radial anisotropy (γ_c) averages about 2.6% in our 3-D model (**Fig. 3-17a**). It is strongest (> 2.6%) across a broad swath of central and northern Alaska, including the Seward Peninsula, the southern parts of Brooks Range, the Ruby Terrane, and the Yukon Composite Terrane, as shown in **Figure 3-20b**. Miller & Hudson (1991) identified regions in Alaska that were subjected to significant Cretaceous ductile extension, which they refer to as the "hinterland" of the Brooks

Range fold and thrust belt. The regions they believe constitute the basement during the extensional episodes are shown schematically in **Figure 3-20a**. These extensional regimes are nearly coincident with the areas of strong crustal radial anisotropy that we image.

Crustal radial anisotropy also has been observed in other regions that have or are undergoing extensional deformation, including in Tibet (Shapiro et al., 2004; Xie et al., 2013) and the Basin and Range province of the western United States (Moschetti et al., 2010). The results we present here support the hypothesis developed in these earlier studies that deformation in the crystalline crust dominantly controls the formation of apparent radial anisotropy, and conversely that apparent radial anisotropy is a marker for crustal extension. Such anisotropy may result from the formation of middle to lower crustal sheet silicates (micas) with shallowly dipping foliation planes beneath extensional domains (e.g., Hacker et al., 2014). Xie et al. (2017) propose that the depth range of the deformation that is causing apparent radial anisotropy lies in the middle to lower crust, but we do not have the depth resolution to test this hypothesis.

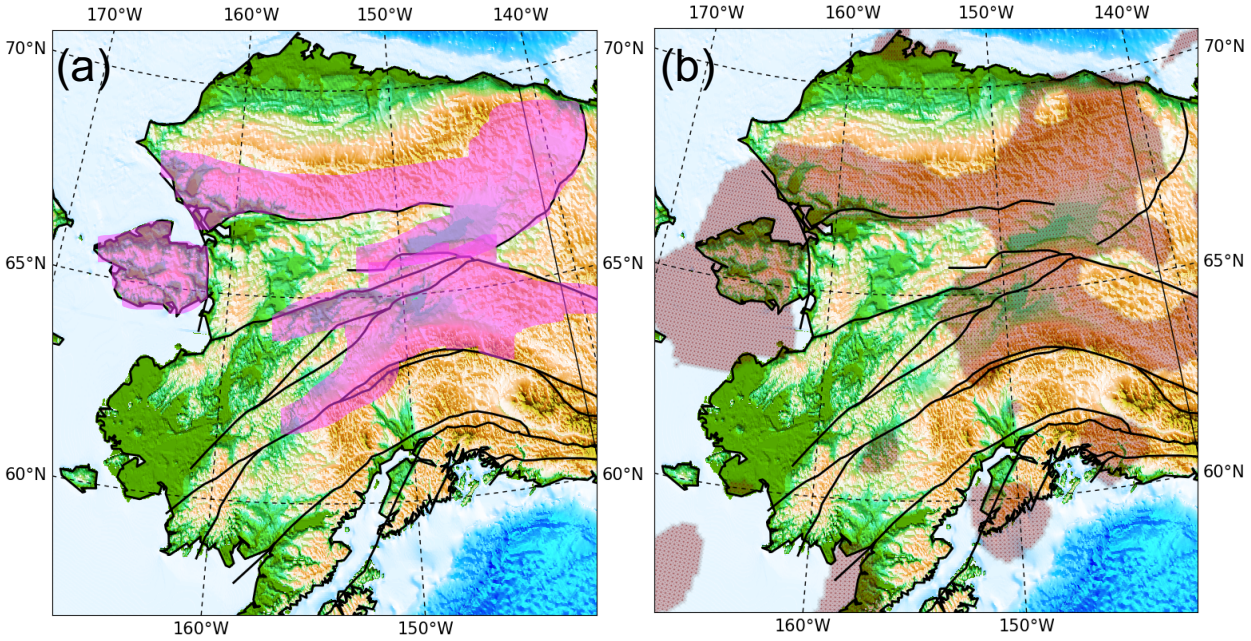

Figure 3-20 Mid-Cretaceous Extensional Domains

(a) Regions (colored in pink) identified by Miller & Hudson (1991) that have been subjected to significant mid-Cretaceous extension. (b) Regions (colored in brown) where we have confidence that the crustal anisotropy in the final model is considered to be stronger than average (γ_c>2.6 %).

3.7.4 Cratons and thickened lithosphere

The horizontal profiles of **Figure 3-14** illustrate similarity between the uppermost mantle beneath Arctic-Alaska and the North American (or Laurentian) craton to the east. Both appear as very high velocity features that extend at least to 120 km depth (e.g., **Fig. 3-21**, profile E-E') and presumably deeper, although we are unable to resolve features reliably below 120 km. Thus, the seismic evidence is quite clear that Arctic-Alaska appears to be underlain by very thick lithosphere that is possibly cratonic in nature.

Moore and Box (2016) describe several prominent models for the tectonic origin of Arctic-Alaska and the arrangement of terranes. These models include those in which Arctic-Alaska has maintained a fixed position relative to North America throughout Phanerozoic time and those they describe as more popular models that involve a large-scale counter-clockwise rotation and

transport of Arctic-Alaska as part of the rotational opening of the Canada Basin in the Early Cretaceous. Kinematic models of the tectonic formation of Arctic-Alaska should consider that this region is underlain by very thick lithosphere that could inhibit large-scale transport or rotation. Other regions with fast and thick lithosphere situated in the presence of significant continental deformation, such as the Tarim Basin (e.g., Molnar & Tapponnier, 1981), the Sichuan Basin (e.g., Klemperer et al., 2006), and the Ordos Block in Asia, appear to impede crustal flow and not participate in the surrounding deformational processes except near their margins. Thus, the thick lithosphere of Arctic-Alaska challenges rotational transport models and may be more consistent with fixist models of the evolution of the region. Alternately, the high mantle velocities could result from lithosphere that subducted during the formation of the Brooks Range and foundered afterwards. Attempting to resolve this dichotomy is beyond the scope of this chapter.

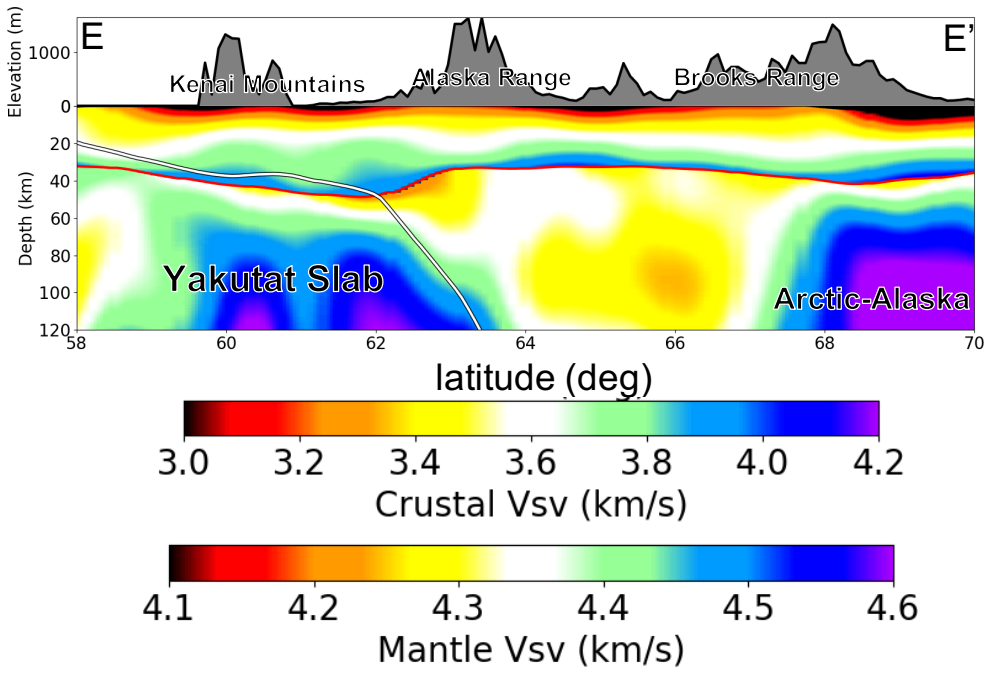

Figure 3-21 Vertical Cross Sections

Vertical cross section E-E' identified in Fig. 3-14b. The white lines in the cross-sections identify the upper edge of the subducting lithosphere in the model of Jadamec and Billen (2010).

Close inspection of **Figures 3-14a** and **3-14b** reveals that the high velocity anomalies beneath Arctic-Alaska extend under the Brooks Range and move southward with increasing depth. This can be seen more clearly in vertical profile E-E' shown in **Figure 3-21**, where it appears that the upper mantle underlying the region underthrusts the Brooks Range. The geometry of the thick lithosphere relative to the location of the Brooks Range provides additional information for tectonic reconstructions of the region. Jiang et al. (2018) also image high velocities in the mantle beneath Arctic-Alaska, which appear to extend further southward at greater depths.

3.8 Conclusions

We present a radially anisotropic 3-D model of Vsv and Vsh for the crust and uppermost mantle to a depth of 120 km beneath Alaska and surroundings using Rayleigh wave group and phase speed and Love wave phase speed measurements. We acquire waveforms from all broad-band seismic stations across the study region openly available from January 2001 to February 2019, totaling more than 500 stations taken from 22 networks (Transportable Array, Alaska Networks, etc.), to perform both ambient noise and earthquake tomography. Rayleigh wave phase speed maps extend from 8 to 85 s period whereas the group speed maps and the Love wave phase speed maps range from 8 to 50 s. These data and corresponding uncertainties are the basis for the inversion for the 3-D model across the study region.

The 3-D model derives from a Bayesian Monte Carlo procedure applied on a grid spacing of approximately 50 km. The prior distribution spans broad bounds around the reference model, in which the sedimentary characteristics and Moho depth come from CRUST-1.0 and crustal and mantle wave speeds come from 1-D model ak135. Constraints limit the accepted models to be vertically smooth between interfaces and relatively simple, which is a hypothesis that is tested in the inversion. The inversion results in a posterior distribution of models beneath each grid point,

which we summarize at each point and depth with the mean ($\bar{m}$), which we refer to as the "mean model", and standard deviation (σ_m), which we refer to as "uncertainty". Shen and Ritzwoller (2016) argue that σ_m is not an ideal estimate of absolute model uncertainty, as it overestimates nonsystematic error and does not explicitly quantify systematic error, but it does provide information about relative uncertainty. We find that we can constrain the shear wave structures relatively well in the middle of the crust and mantle. but internal interfaces are not determined as accurately.

For the vast majority of the region of study, the average model fits the dispersion data well with misfit χ (eqn. (3)) smaller than 2.0 for our final mean model. The data cannot be fit without introducing apparent radial anisotropy, but a very simple parameterization in which mantle and crustal radial anisotropy are spatially variable but respectively constant with depth at each point suffices to fit the data. Crustal anisotropy is represented either with a depth-constant value in the crystalline crust (γ_c) or sediments (γ_c) depending on sedimentary thickness. Typically, $\gamma_s \gg \gamma_c > \gamma_m$, with values of γ_s (determined only in the Colville Basin) being greater than 20%, and values of γ_c and γ_m running up to 8% depending on location. With the current data set we are not justified in inferring a model that possesses more vertical variability of apparent radial anisotropy.

Many structural features are determined reliably in the final 3-D model, and we mention a few in this chapter. (1) Apparent crustal radial anisotropy is strongest across a broad swath of central and northern Alaska, coincident with areas identified by Miller & Hudson (1991) that were subjected to significant Cretaceous extensional deformation. (2) Apparent radial anisotropy in the sediments of the Colville basin is very strong, presumably caused by sedimentary stratification and layering.

(3) Crustal thickness estimates are similar to those based on receiver functions by Miller & Moresi (2018). (4) The uppermost mantle beneath Arctic-Alaska is a high velocity feature that extends at least to 120 km depth, which may be more consistent with fixist models for the evolution of the region than more popular rotational transport models. (5) The slab geometry of the Alaskan subduction zone that we image is largely consistent with the Alaska_3D 1.0 model of Jadamec & Billen (2010), with the principal exception being what we call the Yakutat "slab shoulder region". Our model also confirms the existence of structural features that have been reported by recent studies, including what we call the "Barren Islands slab anomaly" which is a relative low velocity anomaly in the upper mantle that was also observed by Yang & Gao (2019), the "Alaskan aseismic slab edge" that was also observed by Jiang et al. (2018) and Gou et al. (2019), the "Wrangellia slab anomaly" that was also imaged by Gou et al. (2019), and subducting Yakutat lithosphere seaward of the Wrangell volcanic field (Martin-Short et al., 2018; Jiang et al., 2018; Gou et al., 2019). The "Yakutat slab shoulder region" is a high-speed anomaly in our model in the upper mantle, which has not been reported in previous studies.

The 3-D model presented here should be a useful reference for a variety of purposes, including for earthquake location and predicting other types of geophysical data. However, future work is needed to continue to improve both the Vsv and Vsh parts of the model. For example, observations of the Rayleigh wave H/V ratio would help to improve the shallowest parts of the model and receiver functions may be added to help refine internal interfaces. However, receiver functions in Alaska are often complicated and strongly spatially variable, similar in many respects to those in Tibet even though the Tibetan crust is much thicker. The multi-station common Moho conversion point (CMCP) stacking method (e.g. Deng et al., 2015) may yield better information than single-station based stacking or harmonic stripping methods such as those applied across the lower 48

states by Shen and Ritzwoller (2016), for example. There are many other fertile directions to pursue in order to improve and extend the model, but we mention only one more. Once Rayleigh wave azimuthal anisotropy is estimated, those measurements can be added to the data presented here to invert for an integrated model of inherent anisotropy represented by the depth-dependent tilted elastic tensor, as described by Xie et al., (2015, 2017).

Chapter 4

A shear wave azimuthally anisotropic model of the crust and uppermost mantle beneath Alaska revealed by surface waves

4.1 Summary

This chapter presents a shear wave azimuthally anisotropic model of the crust and uppermost mantle beneath Alaska and surroundings, based on seismic data recorded from more than 500 broadband stations. The study is essentially a hypothesis test to determine if a simple two-layer model of anisotropy can reliably predict the azimuthal variation observed in Rayleigh wave phase speed measurements. The model we consider is a two-layer model with anisotropy confined to the brittle upper crust and also the uppermost mantle.

We find that such a simple two-layer model passes the hypothesis test for most of the region of study, from which we draw two conclusions. (a) The data are consistent with crustal azimuthal anisotropy being dominantly controlled by deformationally-aligned cracks and fractures in the upper crust undergoing brittle deformation. (b) The data are also consistent with the uppermost mantle beneath Alaska and surroundings experiencing vertically coherent deformation. There are two exceptions to the latter conclusion, for the Alexander Terrane and Koyukuk Terrane where two anisotropic layers in the mantle are required to fit the data.

The model resolves several prominent features. (1) In the upper crust, fast direction alignment is largely associated with the orientation of major fault lines. (2) In the upper mantle, fast directions are regionalized such that the fast axes are aligned with the compressional direction in compressional domains and oriented parallel to the tensional direction in tensional domains. (3) The mantle fast directions located near the Alaska-Aleutian subduction zone and the surrounding

back-arc area compose a toroidal pattern that is consistent with mantle flow directions predicted by geodynamical modelling (Jadamec & Billen, 2010).

4.2 Introduction

Alaska is a region composed of complex tectonic features including a large subduction zone, the major rotational province of Arctic Alaska (e.g., Moore and Box, 2016), regions of extensional tectonics (e.g., Johnston, 2001), and the successive accretion of terranes along both convergent and strike-slip fault zones in the south (e.g., Coney & Jones, 1985; Johnston, 2001). The active Alaska-Aleutian subduction zone in the southern margin of Alaska is particularly complicated with on-going subduction of the Pacific plate and collisional processes produced by the Yakutat microplate (Eberhart-Philips et al., 2006). At present, different parts of Alaska continue to move relative to the stable North America plate and significant seismicity is found across most of the region of study (Freymueller et al., 2008). The seismic data collected by the recently deployed EarthScope USArray Transportable Array (TA) and other local networks (**Figure 4-1**) provides the unprecedented opportunity to model and understand interior structures and dynamical processes beneath Alaska in much greater detail.

Previous studies of the crust and mantle structures beneath Alaska have been based on a variety of types of data and techniques; however, most of them focused on the inference of isotropic structures (e.g., Jiang et al., 2018; Martin-Short et al., 2018; Ward & Lin, 2018). Existing studies of anisotropy are mostly based on shear wave splitting measurements (e.g., Yang & Fischer, 1995; Wiemer et al., 1999; Christensen & Abers, 2010; Hanna & Long, 2012; Venereau et al., 2019), although a few used seismic tomography based on surface waves (e.g., Wang & Tape, 2014; Feng & Ritzwoller, 2019) or body waves (e.g., Gou et al., 2019). Compared with isotropic structures, seismic anisotropy is a second-order feature that is more difficult to observe. However, it is

important because it is associated with crustal and mantle deformation processes (e.g., Crampin, 1984; Babuska and Cara, 1991; Savage, 1994; Silver, 1996; Long & Silver, 2008), and thus can provide complementary information about the past and present-day deformation to isotropic structures.

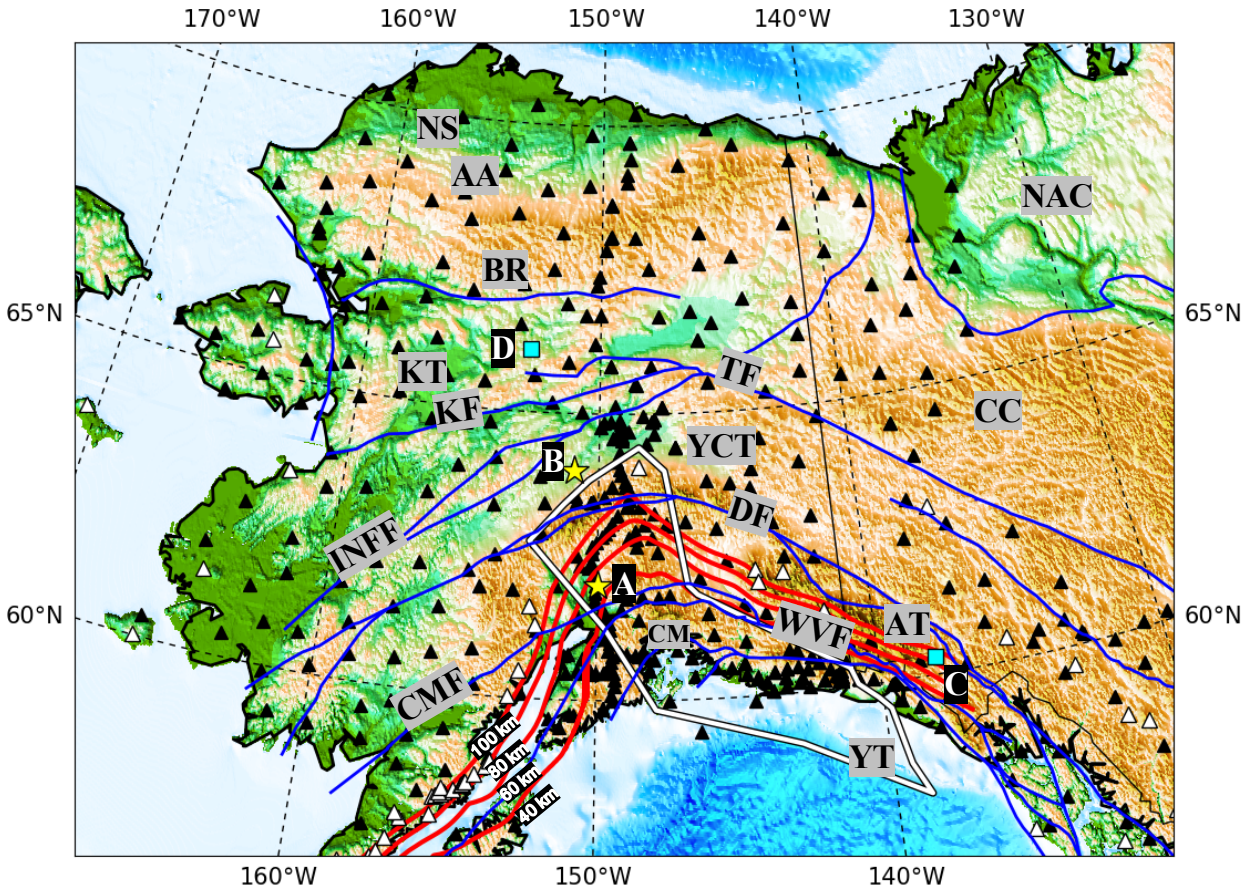

Figure 4-1 Station Distribution Map

Geologic and tectonic features and nomenclature along with seismic station distribution. The blue curves are major faults, and the four red curves are top edges of the subducting Alaskan-Aleutian slab at different depths: from south to north: 40 km, 60 km, 80 km and 100 km (Jadamec and Billen, 2010). The white polygon is the hypothesized Yakutat Terrane (Eberhart-Phillips et al., 2006). Structural and tectonic features are identified with abbreviations explained in Table 4-1. The two yellow stars indicate sample grid points located in the south of Denali (A) and the north of Denali (B) used in Figures 4-3 and 4-6 and the two cyan squares identify sample grid points used in Figure. 4-12 located in the Alexander Terrane (C) and the Koyukuk Terrane (D) where three azimuthal anisotropic layers are required to fit the data. Stations are identified with black triangles and the volcanoes are indicated with white triangles.

Table 4-1 Names of the tectonic features identified with abbreviations

Abbreviation	Name
AA	Arctic Alaska
AT	Alexander Terrane
BR	Brooks Range
CC	Canadian Cordillera
CMF	Castle Mountain Fault
CM	Chugach Mountains
DF	Denali Fault
INFF	Iditarod-Nixon Fork Fault
KF	Kaltag Fault
KT	Koyukuk Terrane
NAC	North American Craton
NS	North Slope
TF	Tintina Fault
WVF	Wrangell Volcanic Field
YCT	Yukon Composite Terrane
YT	Yakutat Terrane

Among recent surface wave studies of anisotropy beneath Alaska, Feng & Ritzwoller (2019) (Ch. 3 of this thesis) constructed a 3-D model with apparent radial anisotropy of shear wave speed (Vsv, Vsh) in the crust and uppermost mantle beneath Alaska. The inferred apparent crustal radial anisotropy is strongest across the parts of central and northern Alaska that were subject to large magnitude mid-Cretaceous extension, consistent with crustal radial anisotropy being caused by deformationally-oriented middle to lower crustal sheet silicates (micas) with shallowly dipping foliation planes beneath extensional domains (e.g., Shapiro et al., 2004; Moschetti et al., 2010). This chapter is a complementary study to Feng & Ritzwoller (2019). Based on data recorded by the TA as well as other permanent and temporary networks in and around Alaska (**Fig. 4-1**), we present a two-layer azimuthally anisotropic model with anisotropy confined in the upper crust and uppermost mantle, derived from the azimuthal variation of Rayleigh wave phase speed measurements from 10 to 80 s.

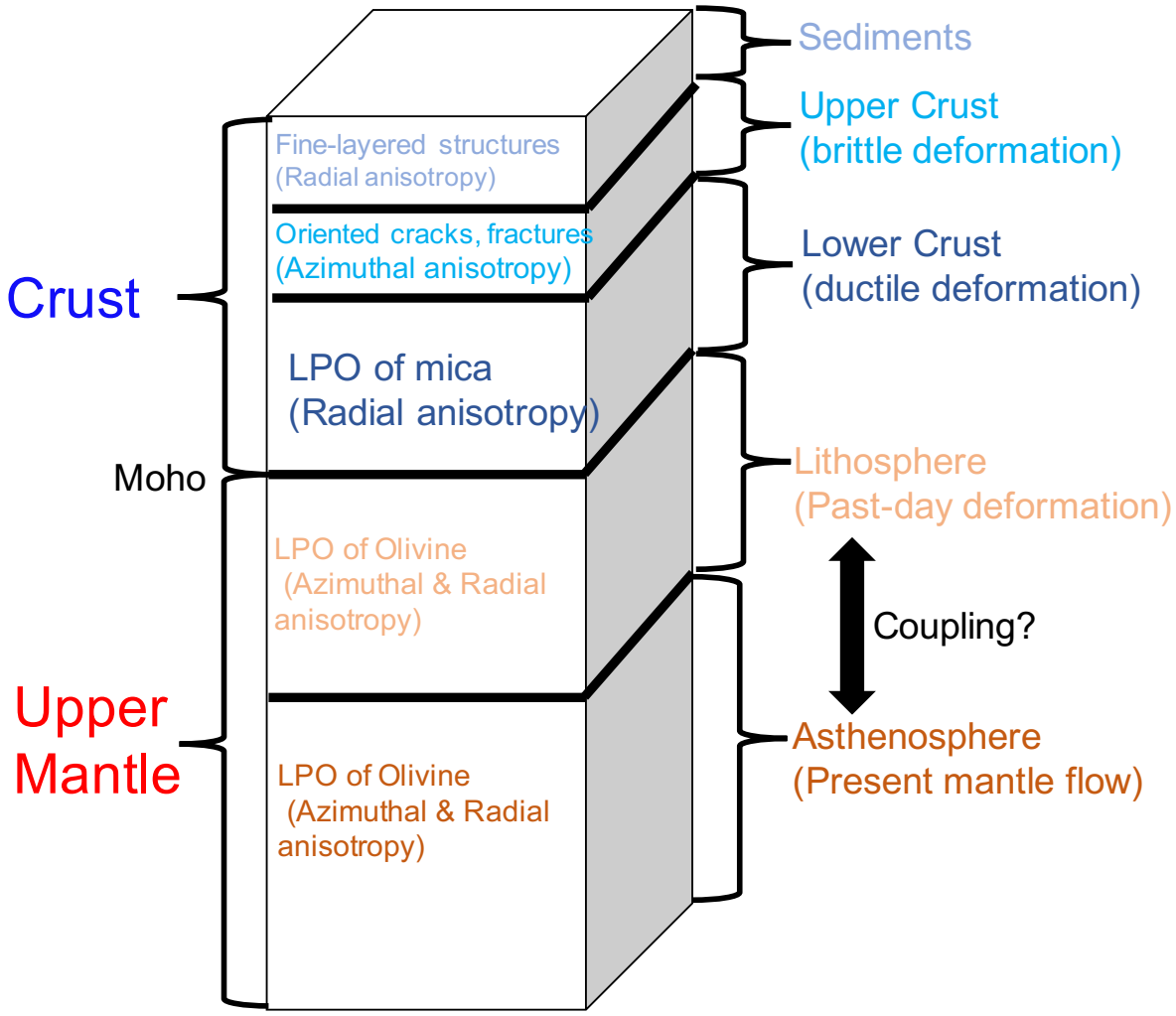

Figure 4-2 Major Causes of Anisotropy

An illustrative figure indicating the hypothetical major causes of seismic anisotropy in the crust and upper mantle.

This chapter presents the results of a hypothesis test to verify if such a two-layer model can fit new observations of azimuthal anisotropy across Alaska reliably, consistent with beliefs in the dominant physical causes of seismic anisotropy in the crust and uppermost mantle derived elsewhere in the world. These beliefs are based on previous studies of seismic anisotropy using surface waves in the US, Tibet, and Alaska (e.g., Shapiro et al., 2004; Moschetti et al., 2010; Lin

et al., 2011; Xie et al., 2015, 2017; Feng & Ritzwoller, 2019). This hypothesized model of anisotropy is illustrated in **Figure 4-2** and is summarized in the following three points.

(1) In the sediments, the fine-layered, largely horizontally deposited structures result in an effective transversely isotropic (TI) medium (Backus, 1962). Strong radial anisotropy is produced when the layers are horizontal while significant azimuthal anisotropy will be generated when the laminated structures are steeply tilted. The Colville Basin is the largest basin across the region of study and produces strong anisotropy. Because Feng & Ritzwoller (2019) reported the existence of extraordinarily strong sedimentary radial anisotropy (> 20 %) in the Colville Basin, it is unlikely that strong azimuthal anisotropy is produced for the same location. Other basins across Alaska are much smaller and thinner than the Colville Basin and thus they cannot contribute significantly to crustal radial and azimuthal anisotropy. In summary, we believe that finely-layered sedimentary structures contribute weakly to azimuthal anisotropy across the region of study. For this reason, we do not implement azimuthal anisotropy in the sediments for the inversion in this study.

(2) The physical causes of anisotropy are different in the upper crust and lower crust. In the upper crust, deformationally-aligned cracks and fractures in the brittle deformation zone typically produce strong azimuthal anisotropy but relatively weak radial anisotropy (e.g., Crampin, 1984; Xie et al., 2015, 2017). In contrast, the lattice-preferred orientation (LPO) of crustal sheet silicates (micas) with shallowly dipping foliation planes controlled by ductile extensional deformation, contribute in the middle to lower crust often resulting in strong radial anisotropy but much weaker crustal azimuthal anisotropy (e.g., Hacker et al., 2014; Xie et al., 2015, 2017). Consequently, in this study we confine azimuthal anisotropy

to the brittly deforming upper crust (< 15 km). We also test other candidate distributions of crustal azimuthal anisotropy, as discussed below in the section 4.7.1.

(3) The seismic anisotropy in the upper mantle is dominantly caused by the lattice-preferred orientation (LPO) of olivine fabrics whose orientation is controlled by deformation processes, which can produce both nonnegligible radial and azimuthal anisotropy. Strong mantle azimuthal anisotropy is often observed with surface waves (e.g., Trampert & van Heijst, 2002; Smith et al., 2004; Ekström, 2011) and shear wave splitting measurements (e.g., Savage, 1994; Long & Silver, 2008; Long, 2013). It has been hypothesized that frozen-in anisotropy, reflecting past episodes of deformation, is generated in the continental lithosphere and oceanic lithosphere (e.g., Smith et al., 2004). In the asthenosphere, however, anisotropy is believed to be caused by present-day mantle flow processes (e.g., Silver & Chan, 1988; Savage et al., 1990; Vinnik et al., 1992; Savage & Silver, 1994; Silver, 1996; Heintz & Kennett, 2005). Therefore, lithospheric and asthenospheric anisotropy may be quite different from one another. However, in this study, we hypothesize that anisotropy is uniformly distributed throughout the uppermost mantle. The uniformly distributed anisotropy, if confirmed by being able to fit data, would indicate vertically coherent deformation in the mantle. The vertical coherence may be inferred to extend to greater depths (below the bottom of our model, namely, 200 km) by comparing fast directions and the amplitude of shear wave splitting from our model with SKS splitting results (e.g., Venereau et al., 2019).

The results we present in this chapter are consistent with the hypotheses about the major physical causes of azimuthal anisotropy in the crust and uppermost mantle. The anisotropic model may help improve understanding of crustal and mantle deformation and associated mantle flow pattern in

the Alaskan-Aleutian subduction zone. The model is also designed to serve as a starting point for further studies, such as estimating the full depth-dependent elastic tensor in the crust and mantle (e.g., Xie et al., 2015, 2017). In this context, we strive to provide reliable information about model uncertainties across the region of study, which will help guide the future use of the model.

As discussed by Feng & Ritzwoller (2019), when inferring anisotropy using surface waves, it is useful to bear in mind two coordinate systems. The first is the frame defined by a symmetry axis (or foliation plane) of the medium of transport, in which "inherent" anisotropy is defined, and the second is the frame of the observations where "apparent" anisotropy is defined. We follow Xie et al. (2017) and refer to measurements of anisotropy and inferences drawn from them in the observational frame as "apparent". Apparent shear wave azimuthal anisotropy, refers to the fact that propagation speed depends on propagation azimuth. A common measure of the apparent shear wave azimuthal anisotropy is the fast azimuth φ_{SV} and amplitude A_{SV} of anisotropy, where the subscript "SV" means that anisotropy is in Vsv. The fast azimuth φ_{SV} defines the direction in which the Rayleigh wave propagates with fastest speed and the anisotropy amplitude A_{SV} depicts the strength of the anisotropy.

Most studies of anisotropy, including this paper and Feng & Ritzwoller (2019), report measurements and models of particular aspects of apparent anisotropy. In contrast, Xie et al. (2015, 2017) present methods that use observations of apparent radial and azimuthal anisotropy to infer characteristics of the depth-dependent elastic tensor, which possesses information about inherent anisotropy. In the long run, it is worthwhile to apply the approach of Xie et al. (2015, 2017), which may improve the determination of the depth distribution of seismic anisotropy, especially in the crust. The inference of inherent anisotropy is beyond the scope of this chapter, however.

The chapter is organized as follows. In section 4.3 we present information about the data sets and the tomographic method used in the study, including how we estimate uncertainties in the Rayleigh wave phase speed measurements and the quantities inferred from them (e.g., A_{SV}, φ_{SV}). Section 4.4 presents examples of the 2-D Rayleigh wave azimuthally anisotropic phase speed maps along with corresponding uncertainties, and section 4.5 shows how the azimuthally anisotropic model is produced by using the first order perturbation method of Montagner & Nataf (1986) to fit the azimuthal variation of dispersion data and uncertainties extracted from the tomographic maps. We present the features revealed by the model in section 4.6 and discuss them in section 4.7.

4.3 Data, Tomographic Method and Uncertainty Estimation

4.3.1 Data

This study utilizes the Rayleigh wave phase speed dispersion measurements (10 to 80 s) produced by Feng & Ritzwoller (2019), Chapter 3, which derive from both ambient noise cross-correlation and earthquake waveforms. The seismic records are extracted from 22 permanent and temporary networks deployed across Alaska and northwest Canada between January 2001 and February 2019 (**Fig. 4-1**). There are 537 seismic stations in total. More detailed information of the seismic arrays and data processing procedures can be found in Feng & Ritzwoller (2019), Chapter 3.

4.3.2 Tomographic method

We perform eikonal tomography (Lin et al., 2009), a geometrical ray theoretical method, to produce azimuthal phase speed estimates from ambient noise and earthquake dispersion data. Eikonal tomography results in local observations of phase speed and uncertainty versus the azimuth of propagation. Phase speed information is on a grid spacing of about 20 km. To enhance the azimuthal coverage of the phase speed measurements and reduce the scatter in the

measurements, we stack all phase speed information on a grid with a spacing about 200 km. This improves the quality of information about anisotropy, but at the expense of reducing spatial resolution. **Figure 4-3** presents the determination of azimuthal anisotropy for two sample grid points on the 200 km grid (A and B), identified in **Figure 4-1**. The phase speed measurements shown in the subpanels in **Figure 4-3** are averaged in 18-degree azimuthal bins.

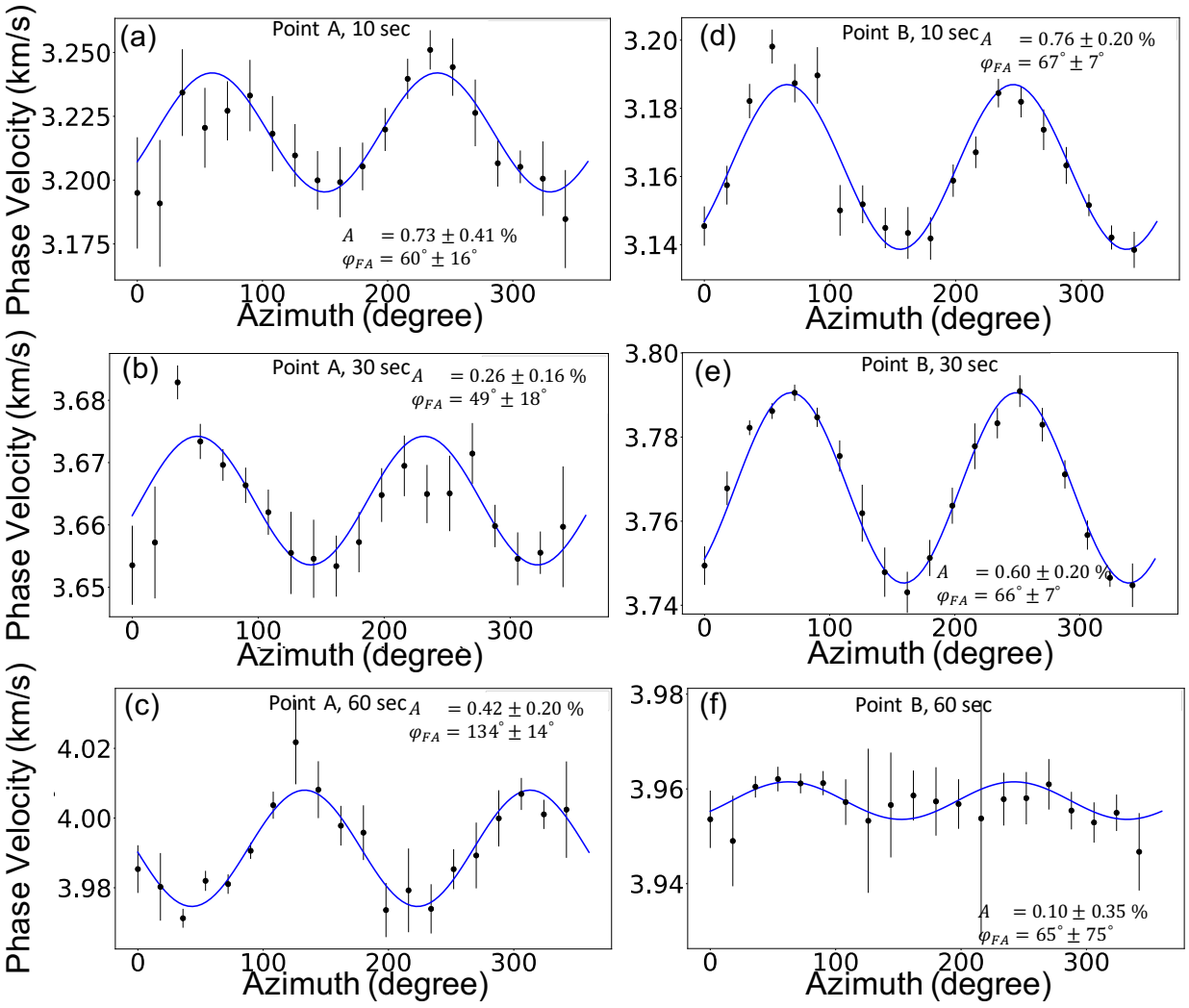

Figure 4-3 Azimuthal Variation of Phase Speed

Azimuthal bin-averaged phase velocity measurements and bin standard deviations for T = 10 , 30 and 60 second periods plotted versus azimuth (ψ) measured using the eikonal tomography method at the sample point A and B identified in Fig. 4-1. (a) – (c): Point A; (d) – (f): Point B.

For weakly anisotropic media, the azimuthally binned Rayleigh wave phase speed measurements typically exhibit a sinusoidal pattern. The observations can be fitted with a function (Smith and Dahlen, 1973) including a sinusoidal term indicating the so-called 2-ψ azimuthal variation:

$$C(\omega,\psi) = C_{iso}(\omega)\{1 + A(\omega)\cos[2(\psi - \varphi_{FA}(\omega))]\} \quad (1)$$

where ψ is the azimuth, ω is the angular frequency, C_{iso} is the isotropic phase speed, $\varphi_{FA}(\omega)$ is the fast azimuth of "$2-\psi$" anisotropy, and $A(\omega)$ is the amplitude of $2-\psi$ anisotropy. Period-dependent values of $\varphi_{FA}(\omega)$ and $A(\omega)$ and their corresponding uncertainties can be determined based on the azimuthally binned phase speed measurements.

Lin & Ritzwoller (2011) reported that a 1-ψ pattern in the phase speed measurements can be observed for long period surface waves near strong structural gradients in isotropic structure. This effect may contaminate the estimates of $\varphi_{FA}(\omega)$ and $A(\omega)$ of the 2-ψ anisotropy. They studied the 1-ψ component and found that it is caused by a backscattering effect in heterogeneous isotropic structures, and concluded that strong 1-ψ patterns could be produced for long period (>50 s) surface waves near strong isotropic phase speed contrasts. Because we also observe strong 1-ψ patterns at long periods in some places, we actually simultaneously estimate the 2-ψ components along with the 1-ψ components, as advocated by Lin & Ritzwoller (2011).

We test the robustness and reliability of our estimates of azimuthal anisotropy by comparison with the azimuthal anisotropic parameters determined from two independent datasets; namely, ambient noise and earthquake datasets. As shown in **Fig. 4-4**, we compare the azimuthal anisotropy maps at T = 30 s period determined from ambient noise tomography (ANT) and earthquake tomography (ET). The fast azimuth yielded by ANT and ET are largely consistent (**Fig. 4-4a** and **Fig. 4-4b**). Indeed, **Fig. 4-4c** shows the angle differences in fast azimuth, and the corresponding histogram

(**Fig. 4-4d**) indicates that more than 80 % of the data points have an angle difference smaller than 30°. Large differences in fast azimuth are located in the North and South parts of the region of study, where the strength of anisotropy is weak. Similar comparison was done for Western United States by Lin et al. (2011).

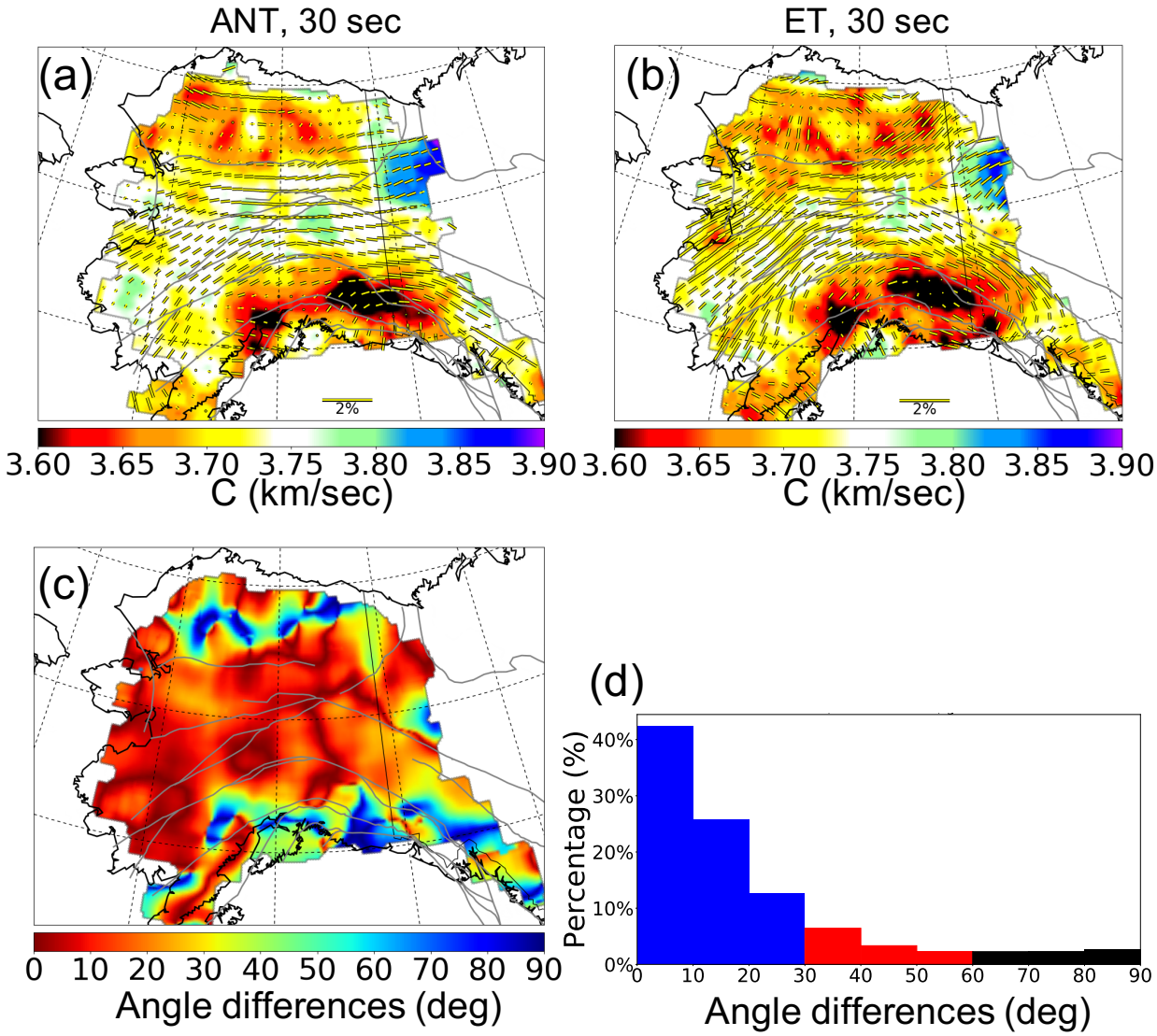

Figure 4-4 Comparison between ANT and ET

(a) Rayleigh wave phase speed maps at period of 30 s along with fast axis directions for azimuthal anisotropy constructed by ANT (Ambient Noise Tomography). (b) Similar to (a) but constructed by ET (Earthquake Tomography). (c) The fast axis angle differences between ANT and ET. (d) Corresponding histogram of (c). More than 80 % of the data points have an angle difference smaller than 30°.

The consistency between the two datasets motivates us to construct the finalized fast axis and anisotropy amplitude maps by combining the ambient noise and earthquake measurements rather than performing tomography for each data set separately and then combining the azimuthal anisotropy maps. From 10 – 18 s, only ambient noise measurements are used, but from 20 – 60 s the fast axis and anisotropy amplitude maps are constructed by averaging the ambient noise and earthquake measurements. Finally, for periods above 60 s, only earthquake measurements are used. The combination of the two types of measurements (ambient noise and earthquake travel times) significantly improves the azimuthal coverage of the phase speed measurements and thus enhances the quality of the estimates of azimuthal anisotropy.

4.3.3 Uncertainty Estimation

Eikonal tomography naturally yields estimates of uncertainties, but Lin et al. (2009) argued that the uncertainties of isotropic phase speed are underestimated because eikonal tomography does not estimate systematic errors or account for the correlation of errors in different travel time measurements. For similar reasons, we find that uncertainties in fast azimuth and anisotropy amplitude determined by eikonal tomography are probably too small. Therefore, we need to scale up the uncertainty estimates to reasonable values.

We estimate the scaling factors by comparing the anisotropic parameters determined by ambient noise (ANT) and earthquake tomography (ET). If an uncertainty map (either fast azimuth or anisotropy amplitude) is properly scaled up, about 68 % of the uncertainty values should be larger or equal to the values taken from the map showing the differences in the anisotropic parameter (either fast azimuth or anisotropy amplitude) determined from ANT and ET. With this approach, we find that the best scaling factors (α) for uncertainty in fast azimuth is $\alpha = 3.5$, and $\alpha = 4.0$ for

uncertainty in anisotropy amplitude. These up-scaled values are reflected in the uncertainty maps of **Figure 4-6**.

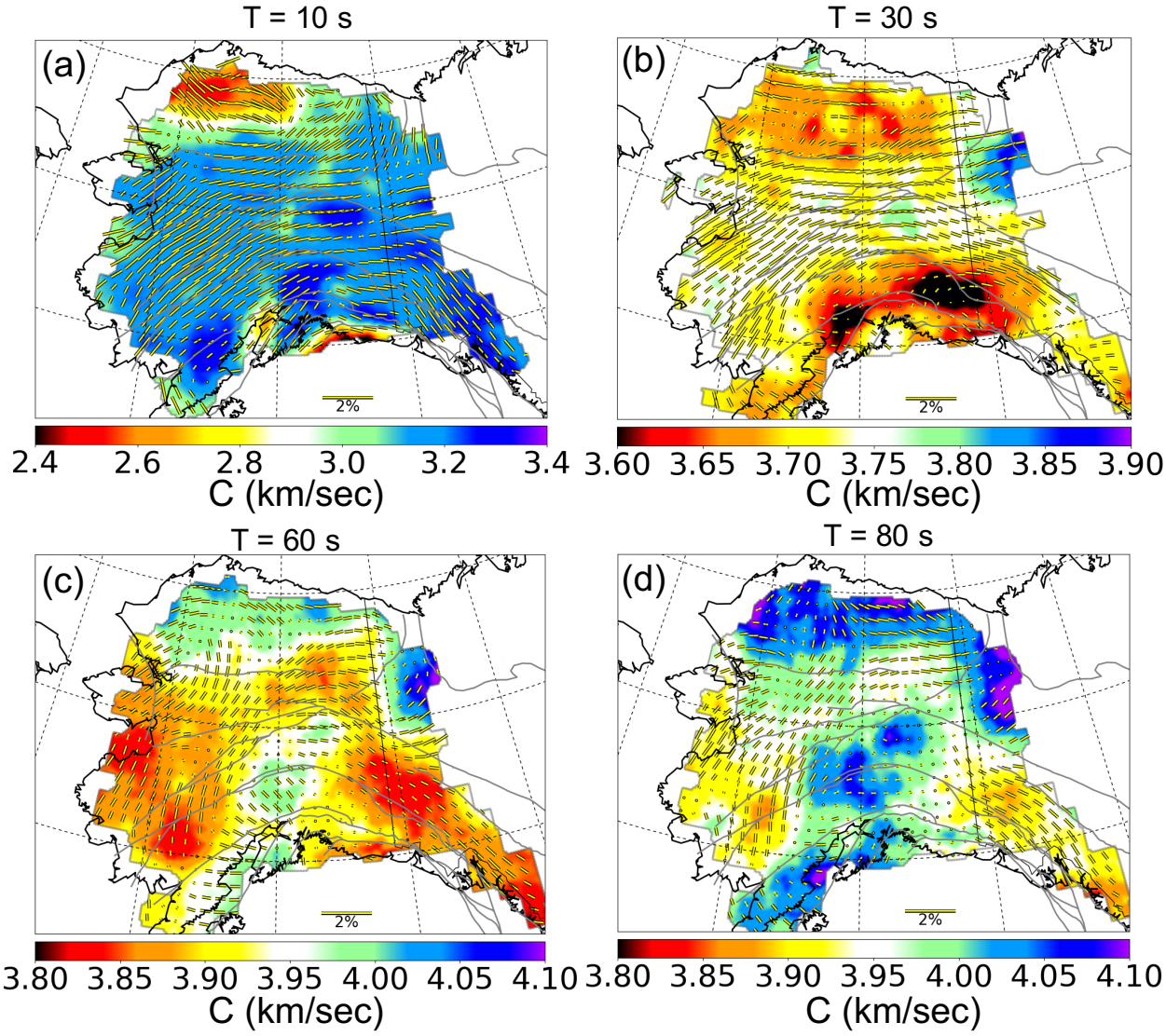

Figure 4-5 Azimuthal Anisotropy Maps

Example azimuthal anisotropy maps. (a) 10 s period. (b) 30 s period. (c) 60 s period. (d) 80 s period.

4.4 Azimuthal Anisotropy Phase Speed Maps

Examples of observations of Rayleigh wave azimuthal anisotropy are presented in **Figure 4-5** at four periods, where the length of each yellow bar is the amplitude of the 2-ψ anisotropy, and the

orientation of each yellow bar is the fast axis direction. The 10 s period (**Fig. 4-5a**) and 30 s period (**Fig. 4-5b**) maps show similar patterns of the fast directions in the interior region of Alaska and they are largely associated to the orientation of major fault lines. This indicates that the crustal azimuthal anisotropy is related to the deformation processes in the fault zones, and may further imply that the anisotropy may be produced by deformationally-oriented cracks and fractures. At 60 s (**Fig. 4-5c**), in contrast, there is a rotational pattern in the fast axis distribution that is associated with the subducting Pacific slab. Together with the high-speed slab, this rotational pattern moves to the north at 80 second period (**Fig. 4-5d**). Patterns of fast directions similar to this have been reported by previous SKS splitting studies (e.g., Christensen & Abers, 2010; Hanna & Long, 2012; Perttu et al., 2014; Venereau et al., 2019).

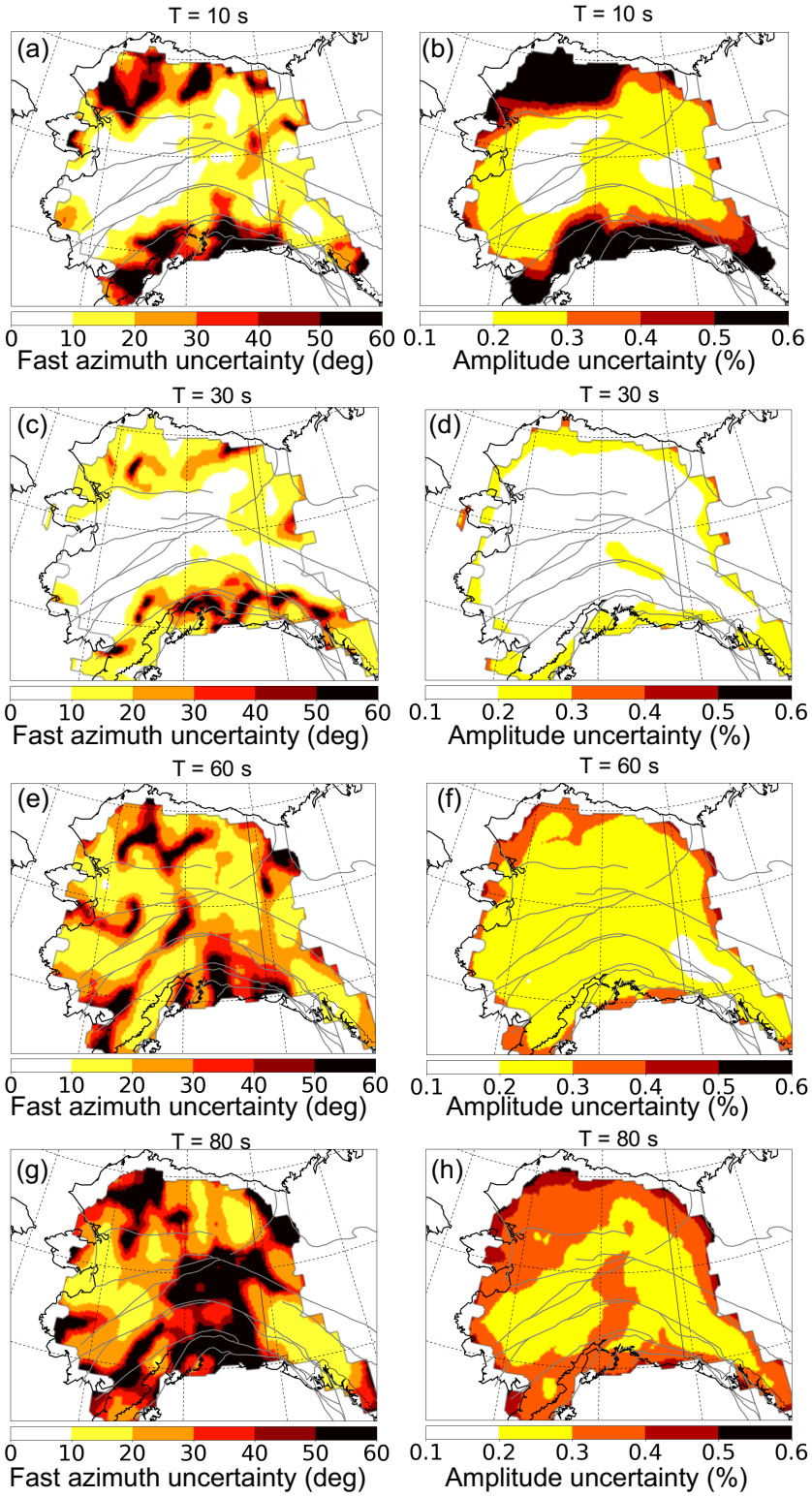

Figure 4-6 Uncertainty Maps

Example maps of uncertainties in fast azimuth and anisotropy amplitude. (a)-(b) 10 s period. (c)-(d) 30 s period. (e)-(f) 60 s period. (g)-(h) 80 s period.

Estimates of uncertainties in fast azimuth and the amplitude of anisotropy for the same sample periods are presented in **Figure 4-6**. The uncertainties in amplitude are the smallest at 30 s period among all the periods, which implies that the quality of the data is probably optimal around this period. This is similar to the isotropic case in Feng & Ritzwoller (2019). The fast azimuth uncertainty maps typically yield large values where the anisotropy amplitudes are small.

Based on the 2D Rayleigh wave azimuthal anisotropy maps, we extract local azimuthal anisotropy dispersion curves on a 200 km grid across the study region, which forms the basis for our inference shear wave azimuthal anisotropy in the crust and mantle. Example azimuthal anisotropy dispersion curves along with corresponding uncertainties for the sample points A and B identified in **Figure 4-1** are shown in **Figure 4-7**.

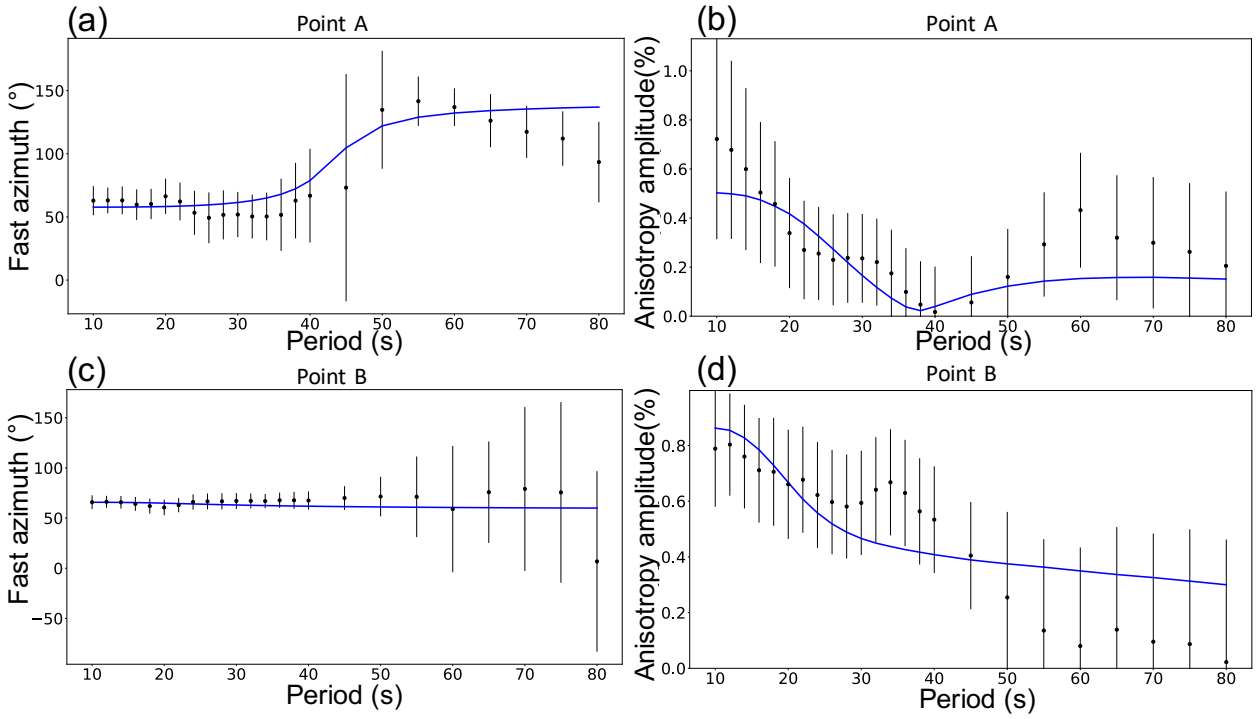

Figure 4-7 Sample Azimuthal Anisotropic Dispersion Curves

Anisotropy dispersion curves of fast azimuth and anisotropy amplitude for the sample points A and B identified in Fig. 4-1. The black dots with error bars are observed data and the blue lines are predictions from the azimuthally anisotropic model. (a) - (b) point A; (c) – (d): Point B.

4.5 Inversion for a Model of Azimuthal Anisotropy in the Crust and Uppermost Mantle

Local Rayleigh wave fast azimuth and anisotropy amplitude with uncertainties are taken directly from the azimuthal anisotropy and uncertainty maps (e.g., **Figs. 4-5** and **4-6**.). Fast azimuth and anisotropy amplitude with uncertainties presented as error bars are shown for two example locations A and B in **Figure 4-7**. These locations are identified as yellow stars in **Figure 4-1**. The local azimuthal anisotropy dispersion curves are the input for the inversion that determines azimuthally anisotropic parameters at different depths within the Earth. The inversion procedure is similar to Lin et al. (2011), and consists of two steps.

(1) Given the reference Vsv velocity model, constructed by Feng & Ritzwoller (2019) and described in Ch. 3 of this thesis, we use the transversely isotropic forward code of Robert Herrmann's Computer Programs in Seismology (Herrmann, 2013) with earth flattening to compute corresponding sensitivity kernels for the elastic parameters (A, C, F, L, N) that describe the TI medium (Xie et al., 2015). The sensitivity kernels are the basis for the inversion for shear wave azimuthal anisotropy, as stated below in section 4.5.2.

(2) We estimate the fast azimuth φ_{SV} and anisotropy amplitude A_{SV} using the first order perturbation theory that predicts azimuthally anisotropic behavior of Rayleigh waves (Montagner & Nataf, 1986). Here we use φ_{SV} and A_{SV} for fast azimuth and anisotropy amplitude, indicating the shear wave azimuthally anisotropic model parameters based on a reference Vsv model. Note that those two symbols are different from the symbols representing frequency-dependent fast azimuth and anisotropy amplitude of Rayleigh waves, namely $\varphi_{FA}(\omega)$ and $A(\omega)$.

4.5.1 Model parametrization

As illustrated in **Figure 4-8**, our model parameterization consists of two anisotropic layers. The upper layer is the upper part of the crust (<15 km), which indicates the region where azimuthal anisotropy is dominantly produced by brittly deforming crust, with oriented cracks and fractures (e.g., Crampin, 1984). The lower layer is in the mantle and extends from the Moho to the bottom of the model at a depth of 200 km. In this layer, mantle anisotropy could be caused by lattice-preferred orientation (LPO) of olivine fabrics that are associated with large scale deformation and mantle flow directions. As discussed in the Introduction, we do not implement azimuthal anisotropy in the sediments or in the lower crust, where we hypothesize that azimuthal anisotropy is relatively weak across the region of study and anisotropy is largely radial.

In summary, the model that we infer is composed of two sets of fast azimuth φ_{SV} and anisotropy amplitude A_{SV}, namely, $(\varphi_{SV}^{(1)}, A_{SV}^{(1)})$ in the upper crust and $(\varphi_{SV}^{(2)}, A_{SV}^{(2)})$ in the mantle. The model parameterization is designed as a hypothesis test to determine if Rayleigh wave azimuthally anisotropic measurements can be fit with such simple model parameterization, which seen as adding weight to our understanding of seismic anisotropy determined elsewhere in the world and also test for the vertical coherence in mantle deformation.

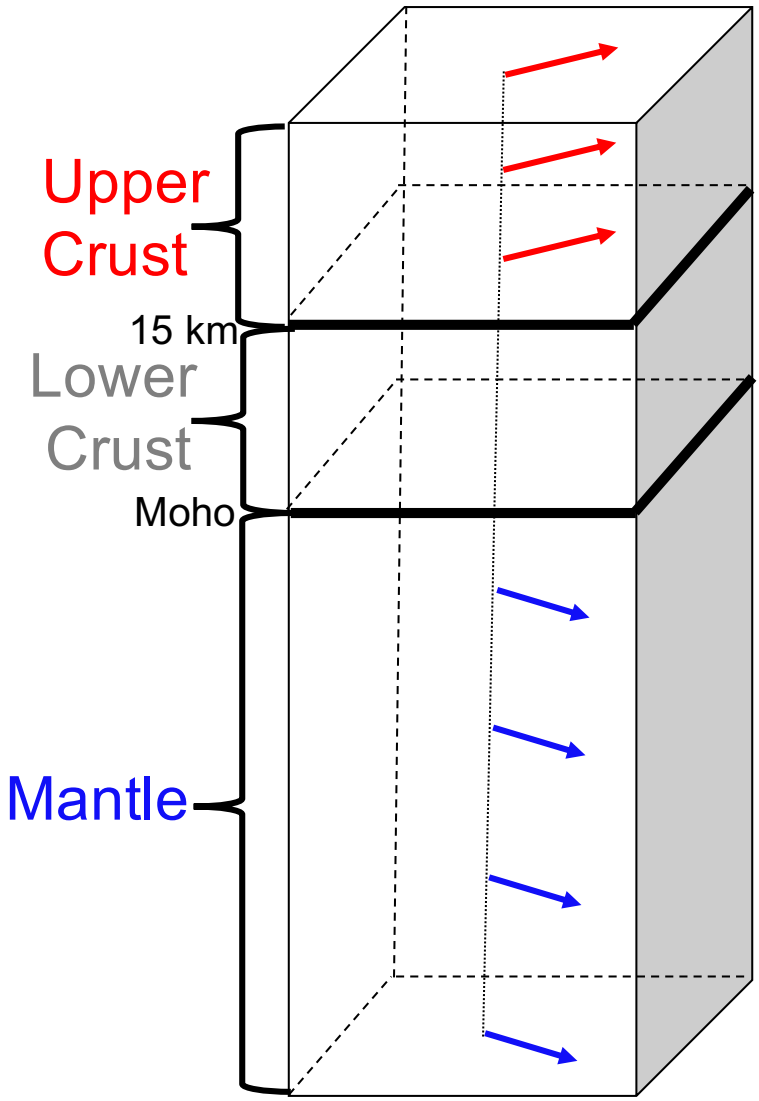

Figure 4-8 Model Parameterization

An illustrative cartoon of the two-layer model that is inverted for in this study. Uniform distribution of anisotropy is implemented in the upper crust and mantle respectively.

4.5.2 Inversion Scheme

Our inversion scheme is based on first order perturbation theory proposed by Montagner & Nataf (1986), which describes the azimuthal variation of Rayleigh wave phase speed as:

$$\delta C_R(\omega,\psi) = \int_0^H \{(B_c \cos 2\psi + B_s \sin 2\psi)\frac{\partial C_R}{\partial A}|_0 + (G_c \cos 2\psi + G_s \sin 2\psi)\frac{\partial C_R}{\partial L}|_0$$

$$+(H_c \cos 2\psi + H_s \sin 2\psi)\frac{\partial C_R}{\partial F}|_0\}dz \qquad (2)$$

In eq. (2), B_c, B_s, G_c, G_s, H_c and H_s are linear combinations of the components of the azimuthally variable parts of the elastic modulus matrix and $\frac{\partial C_R}{\partial A}|_0$, $\frac{\partial C_R}{\partial L}|_0$ and $\frac{\partial C_R}{\partial F}|_0$ are the sensitivity kernels for three of the elastic parameters (A, C, F, L, N) that describe a TI media. We omit the H_c and H_s terms because their impact on Rayleigh wave phase speed are small based on empirical mineralogical models (Montagner & Nataf, 1986). Similar to Lin et al. (2011) and based on studies of olivine (Montagner & Nataf, 1986) as well as mica and amphibole in crustal rocks (Barruol & Kern, 1996), we assume that $B_{c,s}/A = G_{c,s}/L$. Thus, eq. (2) can be simplified as:

$$\delta C_R(\omega, \psi) = \int_0^H \{G_c \cos 2\psi \left(\frac{A}{L}\frac{\partial C_R}{\partial A}|_0 + \frac{\partial C_R}{\partial L}|_0 \right) + G_s \sin 2\psi \left(\frac{A}{L}\frac{\partial C_R}{\partial A}|_0 + \frac{\partial C_R}{\partial L}|_0 \right)\} dz \quad (3)$$

The fast azimuth φ_{SV} and anisotropy amplitude A_{SV} can be determined from moduli G_c and G_s as:

$$\varphi_{SV} = \frac{1}{2}\tan^{-1}\left(\frac{G_s}{G_c}\right) \quad (4)$$

and

$$A_{SV} = \frac{1}{2L}\sqrt{G_c^2 + G_s^2} \quad (5)$$

Given observed azimuthal anisotropy dispersion curves, we estimate $(G_c^{(1)}, G_s^{(1)})$ and $(G_c^{(2)}, G_s^{(2)})$ in the upper crust and mantle simultaneously. Corresponding uncertainties are determined from the estimated model covariance matrix (Tarantola, 2005). Finally, the fast azimuth and anisotropy amplitude can be determined from eqs. (4) and (5).

4.6 Results

The estimated two sets of fast azimuth and anisotropy amplitude, namely, $(\varphi_{SV}^{(1)}, A_{SV}^{(1)})$ in the upper crust and $(\varphi_{SV}^{(2)}, A_{SV}^{(2)})$ in the mantle, compose our model of shear wave azimuthal anisotropy,

illustrated in **Figure 4-9**. The upper crustal fast directions are mostly aligned with the major faults, which indicates that the azimuthal anisotropy in the upper crust may be produced by deformationally-aligned cracks and fractures. The distribution of mantle fast directions depicts a toroidal flow pattern associated with the slab edge of the Alaskan-Aleutian subduction zone (e.g., Feng & Ritzwoller, 2019). Similar patterns of corner flow have been reported by SKS splitting studies (e.g., Christensen & Abers, 2010; Hanna & Long, 2012; Perttu et al., 2014; Venereau et al., 2019) and predicted by geodynamical modelling (e.g., Jadamec & Billen, 2010).

Maps of the misfit of observations of fast azimuth and anisotropy amplitude by the resulting two-layer model are shown in **Figure 4-10**. We define the misfit as follows:

$$\chi = \sqrt{\frac{1}{\mathrm{N}}\sum_{\mathrm{i}=1}^{\mathrm{N}} \frac{(\Delta d_i)^2}{\sigma_{\mathrm{i}}^2}} \tag{6}$$

where Δd_i is the differences between an observed datum (fast azimuth or anisotropy amplitude) and the data value predicted from the model, and σ_{i} is the one standard deviation data uncertainty. The index i ranges over dispersion data, where N is the number of the data values. Δd_i for fast azimuth is defined as:

$$\Delta d_i = \begin{cases} \left|\varphi_i^{obs} - \varphi_i^{pre}\right|, & if\ \left|\varphi_i^{obs} - \varphi_i^{pre}\right| \leq 90° \\ 180° - \left|\varphi_i^{obs} - \varphi_i^{pre}\right|, & if\ \left|\varphi_i^{obs} - \varphi_i^{pre}\right| > 90° \end{cases} \tag{7}$$

where φ_i^{obs} is the observed fast azimuth and φ_i^{pre} represents the predicted value. For anisotropy amplitude, Δd_i is defined as follows:

$$\Delta d_i = A_i^{obs} - A_i^{pre} \tag{8}$$

where A_i^{obs} is the observed anisotropy amplitude and A_i^{pre} indicates the predicted value.

Our hypothesized model with azimuthal anisotropy confined to the uppermost crust to a depth of 15 km and with a single layer in the mantle can reasonably predict data in most parts of the region of study. This result is consistent with our beliefs about the major causes of azimuthal anisotropy

in the crust and uppermost mantle, but also provides support for the vertical coherence of deformation in mantle above a depth of 200 km, which is the bottom of the model. However, the misfit values in fast azimuth (**Fig. 4-10a**) are large in Alexander Terrane and Koyukuk Terrane (identified as AT and KT in **Fig. 4-1**), where an additional mantle layer is required to fit the data. We discuss this in more detail in the following Discussion section.

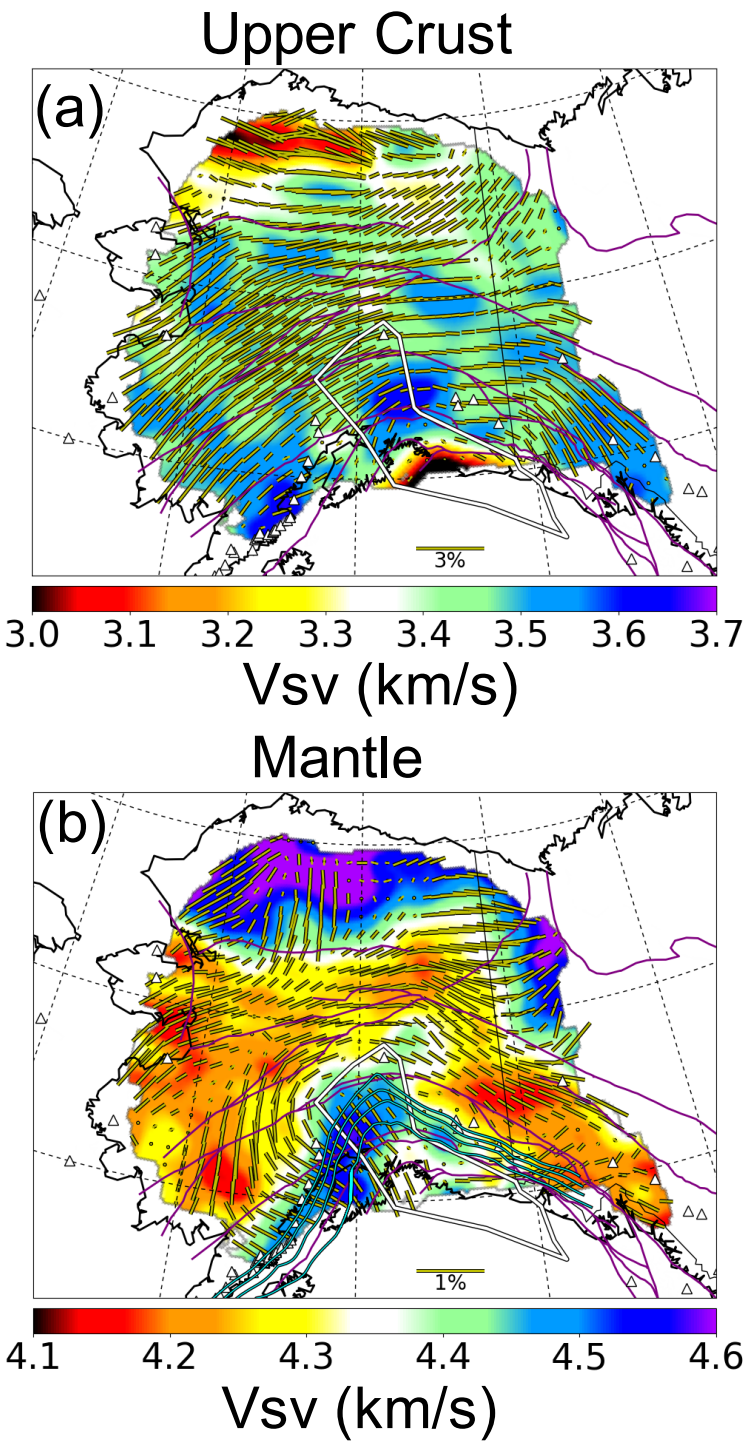

Figure 4-9 Azimuthal Anisotropy Model

Azimuthal anisotropy model. (a) Upper crustal azimuthal anisotropy, the background color indicates the Vsv structure at the depth of 10 km. (b) Mantle azimuthal anisotropy, the background color indicates the Vsv structure at the depth of 100 km. The purple lines indicate major fault and the white polygon outlines the hypothesized Yakutat terrane. Cyan lines in (b) identify the edge of slab at the depth of 40 ~ 100 km.

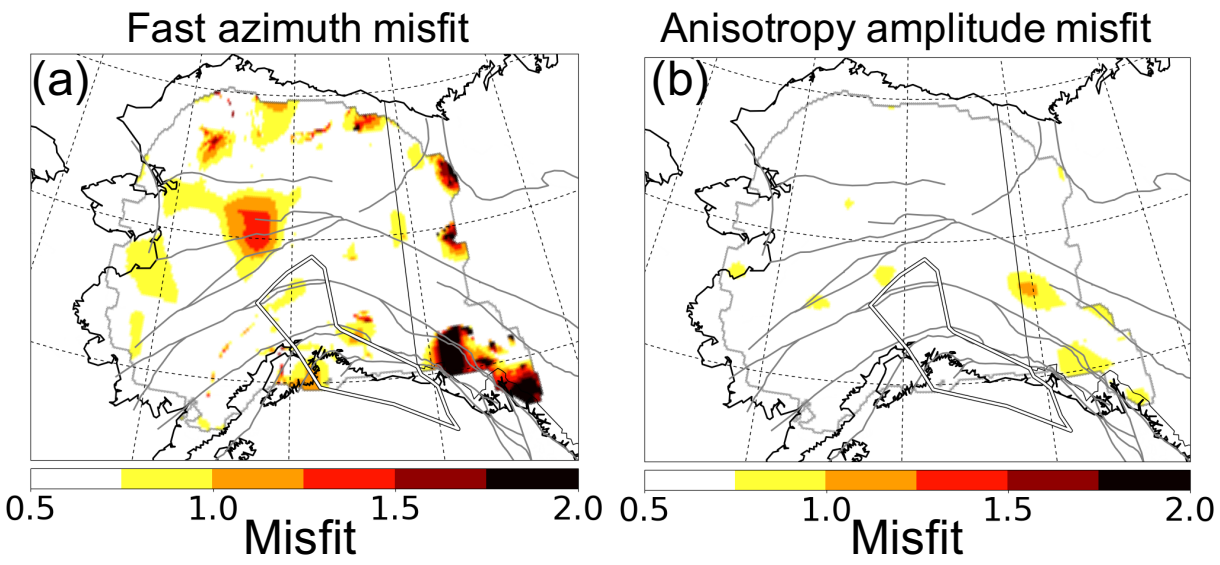

Figure 4-10 Misfit Maps

(a) Misfit values computed for fast azimuth. (b) Misfit values for anisotropy amplitude.

4.7 Discussion

4.7.1 Crustal Anisotropy

The hypothesized model has crustal anisotropy confined in the upper crust; however, it is instructive to determine how the data fit would change if anisotropy is implemented in different depth ranges of the crystalline crust. We consider four candidate models with different parameterizations of crustal azimuthal anisotropy;, namely, implementing anisotropy in different parts of the crust. (1) Upper crustal anisotropy: Azimuthal anisotropy is only allowed in the upper crust, namely, from the bottom of the sediments to a depth of 15 km. This is the preferred hypothesized model described above. (2) Lower crustal anisotropy: Azimuthal anisotropy is confined in the lower crust; namely, from a depth of 15 km to the Moho. (3) Whole crustal anisotropy: a uniform distribution of azimuthal anisotropy is implemented from the bottom of

sediments to the Moho. (4) Two-layer crustal anisotropy: The upper crust and lower crust have completely different azimuthal anisotropy, namely, different values of φ_{SV} and A_{SV}.

We perform four separate inversions to construct these candidate models . The misfit maps of Model (1) for fast azimuth and anisotropy amplitude are illustrated in **Figure 4-10**. We also find that the misfit values of Models (2) and (3) (maps not shown here) are almost identical to Model (1). In addition, compared with Model (1), there is very little improvement in the data fit predicted using Model (4) (map not shown here). Note that in **Fig. 4-10a**, the regions with large fast azimuth misfit require additional layer(s) in the mantle but not the crust, which will be discussed further in below. The similarity in misfit values among the candidate models underscores the difficulty in constraining the depth distribution of azimuthal anisotropy in the crust with our dataset.

Consequently, given the misfit values, there is no preference between the four candidate distributions of crustal anisotropy with depth. However, previous studies (e.g., Shapiro et al., 2004; Moschetti et al., 2010; Lin et al., 2011; Xie et al., 2015, 2017; Feng & Ritzwoller, 2019) have given rise to crustal azimuthal anisotropy present in Model (1), which is why we have chosen this model as the basis for our parameterization rather than the other candidates.

In summary, our physically preferred model based on earlier studies passes the hypothesis test, which is consistent with the understanding that crustal azimuthal anisotropy is dominantly produced by deformationally-aligned cracks and fractures in the upper crust undergoing brittle deformation. In the future, it may prove to be advantageous to apply methods developed by Xie et al. (2015, 2017) to estimate the depth-dependent elastic tensor by interpreting Rayleigh wave azimuthal anisotropy simultaneously in combination with Love wave data (radial anisotropy), which may improve constraints on the depth distribution of crustal anisotropy.

4.7.2 Mantle Anisotropy

A typical layerization of the upper mantle above the 410 km discontinuity would include at least two distinct layer; namely, the lithosphere and the asthenosphere. The layering can be more complicated in subduction zones where one plate is under-thrusting another one, which is the case for the Alaska-Aleutian subduction zone. However, our dataset does not provide good vertical resolution of the depth-dependent distribution of mantle azimuthal anisotropy. Therefore, instead of trying to infer the layering of the azimuthal anisotropy in the mantle, we present a hypothesized model with a uniform distribution of azimuthal anisotropy from the Moho to the bottom of the model (200 km) and see if this allows the data to be fit.

The hypothesis test for the simple one-mantle-layer model is designed to infer a dominant factor controlling mantle azimuthal anisotropy and also test whether there is vertically coherent mantle deformation across the region of study. Understanding the vertical coherence of deformation may provide insight into the relation between lithospheric deformation and asthenospheric flow.

As indicated in **Figure 4-10**, the hypothesized model with one azimuthally anisotropic layer in the mantle can reasonably predict data for most of the study region, providing evidence for the vertical coherence of azimuthal anisotropy in the uppermost mantle across most of the region of study. The only two exceptions are located in the Alexander Terrane and Koyukuk Terrane (identified as AT and KT in **Fig. 4-1**). In the following three subsections, we discuss the fast direction patterns, the vertical coherence of mantle deformation and the possible existence of multiple mantle anisotropic layers in the Alexander Terrane and Koyukuk Terrane.

4.7.2.1 Fast Direction Patterns

In this subsection, we discuss the fast directions in the mantle presented by our model (**Fig. 4-9b**). The fast directions vary regionally and exhibit different patterns associated with isotropic

structures. The large-scale high isotropic velocity anomalies in **Fig. 4-9b** identify the compressional regions of the mantle, which include Arctic Alaska, North American Craton and the Pacific subduction zone. Fast directions are generally oriented along the compressional direction in these regions. Broadly speaking, the low speed region in the interior of Alaska undergoes tensional deformation (e.g., Redfield, 2007) and the fast directions are mostly aligned with the directions of tensional deformation.

We also note that the fast directions in the slab region and back-arc area are related to the slab geometry. As indicated in **Fig. 4-9b**, the fast directions are slab-perpendicular in the subduction zone and they shift to a slab-surrounding pattern in the back-arc region. Together, this transition in fast directions composes a toroidal pattern around the slab edge. This is consistent with the toroidal mantle flow directions around Alaskan slab edge predicted by geodynamical modelling (Jadamec & Billen, 2010).

In addition, the fast directions of the model are mostly consistent with SKS splitting results (Venereau et al., 2019), as shown in **Figure 4-11**. For the comparison, we discard outliners with fast azimuth uncertainty larger than 30°. The yellow bars in **Figure 4-11** indicate the orientation of fast directions of the mantle anisotropy from our model and the blue, green and red bars represent orientation of SKS splitting fast axes. Blue bars also identify the data points which the differences between our results and SKS splitting observations are smaller than 30°.The black bars identify the locations of the sample points where we perform inversion with an additional mantle layer, which is discussed in 4.7.2.3. The histogram in **Figure 4-11b** indicates that more than 80% of the data points have an angle differences smaller than 30°. Accordingly, we suggest that azimuthal anisotropy in the back-arc areas is dominantly controlled by mantle flow surrounding the slab edge.

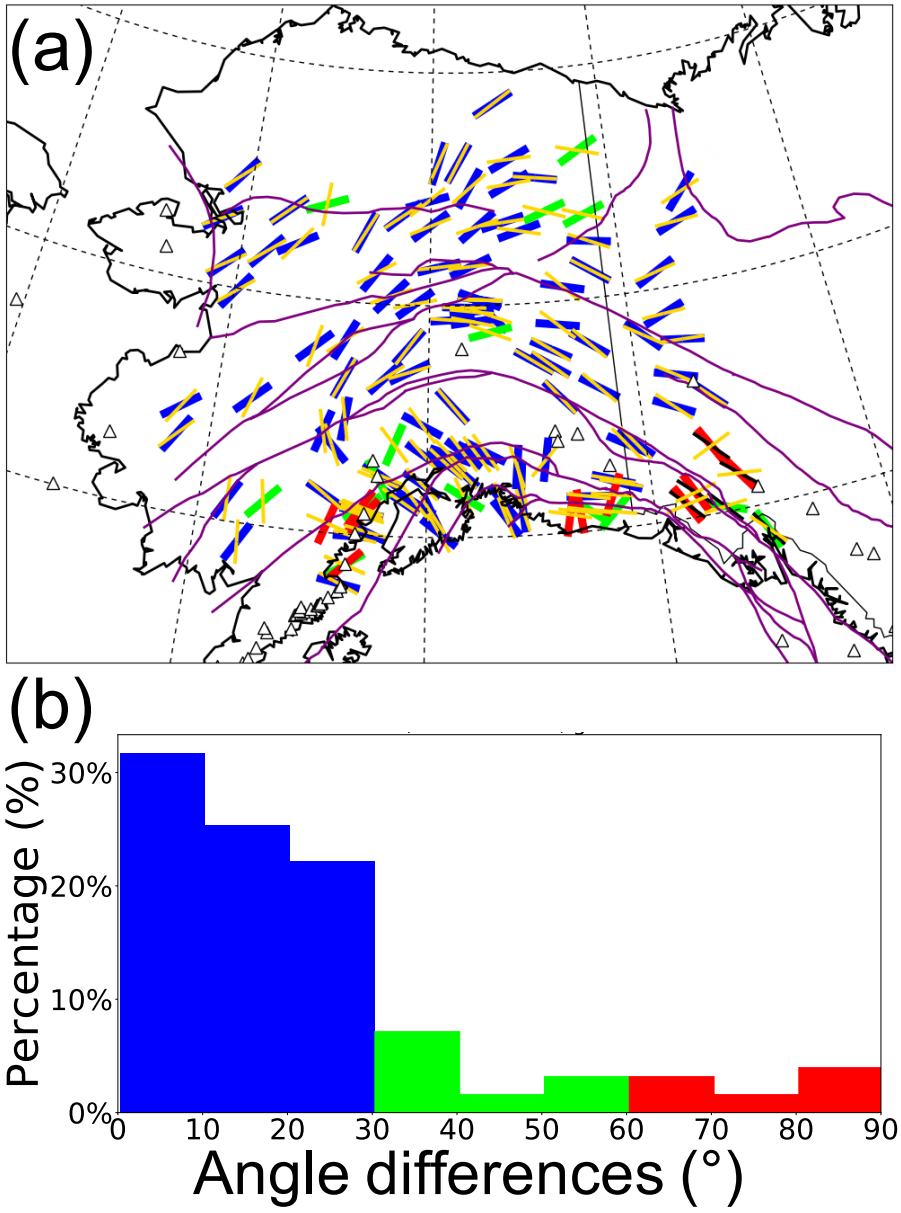

Figure 4-11 Comparing with SKS Fast Directions

(a) Comparison of fast directions determined by SKS splitting (Venereau et al., 2019) and this study, data points with fast azimuth uncertainties larger than 30°are discarded for this comparison. The yellow bars indicate fast directions from this study while the blue, green and red bars represent the fast axis estimated from SKS splitting. Blue bars indicate the locations where the differences in fast directions are smaller than 30°, green ones correspond to the differences of 30°~60° and the red ones identify the points with differences larger than 60°. The black bars located in the Alexander Terrane identify the sample points where we perform inversion by adding an additional anisotropic mantle layer. Those bars also represent fast directions of the lower mantle layer. (b) Corresponding histogram of (a), there are more than 80 % of data points that have an angle difference smaller than 30°.

4.7.2.2 Vertical Coherence of Mantle Deformation

For most of the region of study, the data can be well fit with one azimuthally anisotropic layer in the mantle (**Fig. 4-10**). Therefore, we conclude that the azimuthal anisotropy in the mantle above 200 km (bottom of the model) is consistent with being vertically coherent across most of the region. The depths to which this coherence extends can be constrained by comparing the observed SKS splitting time with the prediction from our model. **Fig. 4-12** presents a histogram of the predicted SKS splitting time in which the observed time is subtracted. The observed SKS splitting delay times are notably larger than the values predicted from our model, with an average difference of 0.66 s which is larger than half of the average observed SKS splitting time (Venereau et al., 2019). Thus, we believe there is a significant contribution to azimuthal anisotropy from deeper in the mantle (> 200 km), and suggest that there may be vertically coherent deformation from the uppermost mantle to a depth larger than 200 km for most of Alaska, except for the Alexander Terrane and Koyukuk Terrane.

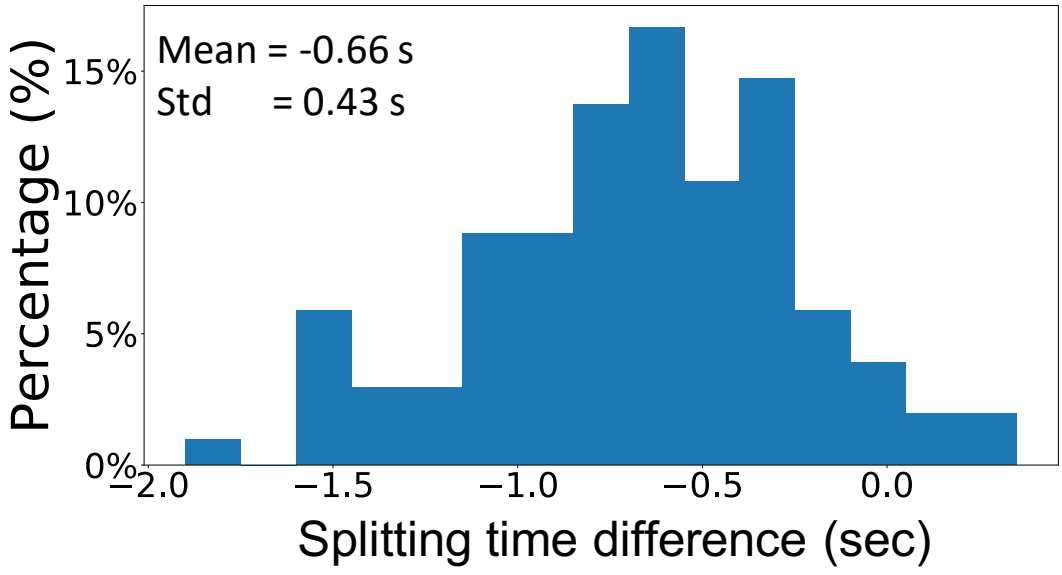

Figure 4-12 Comparing with SKS Splitting Times

Histogram illustrating the differences between predicted SKS splitting time and observed SKS splitting time, by subtracting the observed ones from the predicted ones.

4.7.2.3 Regions with Multiple Layers

As indicated in **Fig. 4-10a**, there are two principal regions where the fast azimuth cannot be well fit with a single anisotropic layer in the mantle. One is the Alexander Terrane while another is the Koyukuk Terrane (identified as AT and KT in **Fig. 4-1**). For both regions, significant improvement in data fit is achieved by adding another layer below a depth of 100 km. This results in two anisotropic mantle layers in which the fast azimuth of the upper one is nearly perpendicular to the lower one's. We interpret these layers as being decoupled.

At the Alexander Terrane, we choose six sample points (identified as black bars in **Fig. 4-11a**) to perform the inversion with an additional mantle layer below 100 km depth. These sample points are selected because they have corresponding SKS splitting measurements. **Figs. 4-13a,b** show the data fit to one of the six sample points, whose location is indicated as point C in **Fig. 4-1**. Data fitness is improved significantly by adding a second mantle layer of anisotropy. The black bars in **Fig. 4-11a** represent the fast azimuth of the lower mantle layer. The fast directions of the upper mantle layer are simply nearly perpendicular to the lower ones so they are not drawn. Because the fast directions in the lower mantle layer are similar to the SKS splitting results, we suggest that the SKS splitting in Alexander Terrane is dominantly controlled by the asthenosphere, and deformation in the lithosphere and asthenosphere are sub-perpendicular to each other.

Fig. 4-13c and **4-13d** show the improvement in data fit for a second point located in the Koyukuk Terrane (point D identified in **Fig. 4-1**). The inversion yields a fast azimuth of 87° in the upper layer and 10° in the lower one. The lower layer's fast direction is similar to the fast direction in Arctic Alaska, to the north of this point.

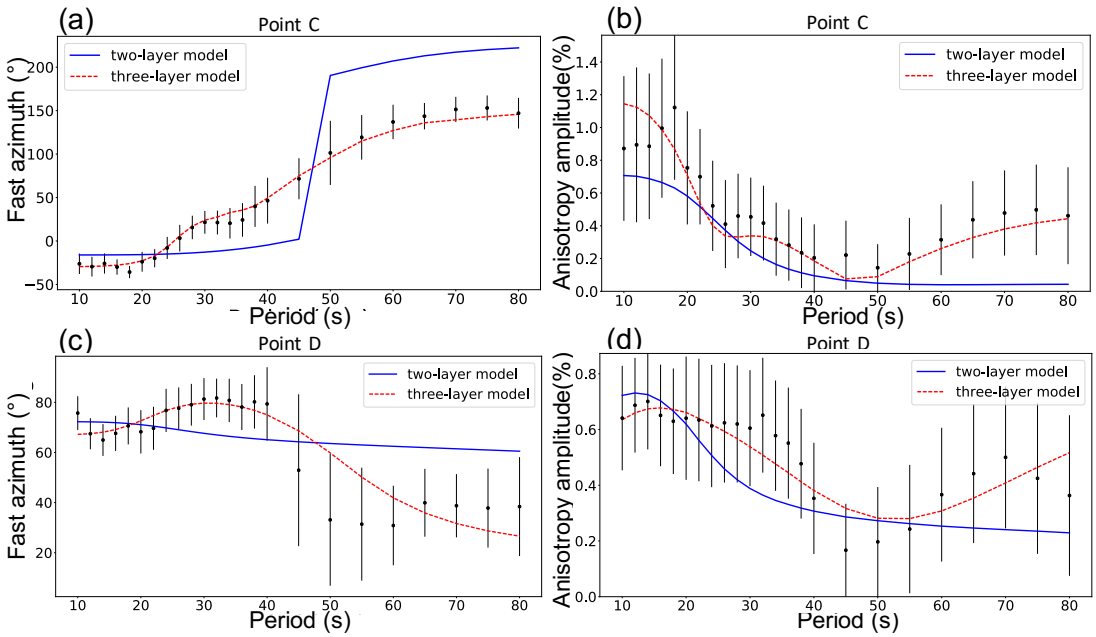

Figure 4-13 Sample Inversion with Additional Mantle Layer

Anisotropy dispersion curves of fast azimuth and anisotropy amplitude for the sample points C and D identified in Fig. 4-1 where an additional anisotropic mantle layer is required to fit data. The black dots with error bars are observed data. The blue lines are predictions from two-layer azimuthal anisotropic models and while the red lines represent predictions from three-layer models. (a)-(b) point C; (c) – (d): Point D.

4.8 Conclusions

We present a shear wave azimuthally anisotropic model of the crust and uppermost mantle beneath Alaska and surroundings. The model is represented by two-layer parameterization of anisotropy where azimuthal anisotropy is confined to the brittle upper crust and uppermost mantle from the Moho to 200 km depth. This study is essentially a hypothesis test and confirms that such a model can reasonably fit the observed azimuthal variation of Rayleigh wave phase speed measurements. The Rayleigh wave dispersion data is taken directly from Feng & Ritzwoller (2019), which derives from waveforms of all broad-band seismic stations across the study region openly available from January 2001 to February 2019, totaling more than 500 stations taken from 22 networks (Transportable Array, Alaska Networks, etc.). Our Rayleigh wave azimuthal anisotropy maps are constructed by both ambient noise and earthquake tomography, which extends from 10 to 80 s

period. These data and corresponding uncertainties are the basis for the inversion for the azimuthally anisotropic model as a perturbation to a reference Vsv model across the study region.

The azimuthally anisotropic model derives from an inversion algorithm that is based on Montagner & Nataf (1984)'s first order perturbation theory that relates the azimuthal variation in Rayleigh wave phase speed measurements with azimuthal anisotropy of shear wave structures. The reference Vsv model that is used to compute the sensitivity kernels was constructed by Feng & Ritzwoller (2019), Chapter 3.

The estimated two-layer azimuthally anisotropic model is able to fit the Rayleigh wave azimuthal anisotropy data across the vast majority of the region of study, except for the Alexander Terrane and Koyukuk Terrane where an additional layer in the mantle is required to fit the long period data. We summarize the major findings of the hypothesis test and the structural features revealed by the azimuthally anisotropic model as follows:

(1) In the crust, confining azimuthal anisotropy to the brittle upper crust is justified by the data, and the fast directions of the apparent crustal azimuthal anisotropy closely follow the orientation of major fault lines. Those facts are consistent with the understanding that crustal azimuthal anisotropy is dominantly caused by deformationally-aligned cracks and fractures (e.g., Crampin, 1984).

(2) For most of the region of study, the data can be fit with a single azimuthally anisotropic layer in the uppermost mantle extending from the Moho to a depth of 200 km, which is consistent with vertical coherent deformation in the uppermost mantle beneath Alaska and surroundings. In addition, the fast directions in the model are largely consistent with SKS splitting results (Venereau et al., 2019). Because the SKS delay times predicted from our model are significantly smaller than the observed values, we suggest that vertical coherent

mantle deformation may extend to depths greater than 200 km across much of the region of study.

(3) The fast directions in the mantle located at the Alaska-Aleutian subduction zone compose a toroidal pattern that is consistent with mantle flow directions predicted by geodynamical modelling (Jadamec & Billen, 2010). This implies that the azimuthal anisotropy in the back-arc area may be controlled by toroidal mantle flow.

(4) An additional anisotropic mantle layer is required to fit data in the Alexander Terrane and Koyukuk Terrane. The fast directions of the lower mantle layer in the Alexander Terrane are consistent with SKS splitting results, providing evidence for the existence of two azimuthally anisotropic mantle layers with fast directions sub-perpendicular to each other.

The hypothesis test and the azimuthally anisotropic model presented in this chapter is designed to be a useful reference for a variety of purposes, including inferring deformation in the upper crust and to constrain various details in upper mantle dynamics. However, future work is needed to continue to improve the depth resolution of the azimuthally anisotropic model. There are many other fertile directions to pursue in order to improve and extend the model, but we mention only one. Rayleigh wave azimuthal anisotropy can be combined with Love wave dispersion data to invert for an integrated model of inherent anisotropy represented by the depth-dependent tilted elastic tensor, as described by Xie et al., (2015, 2017). This approach may provide better depth constraints on anisotropy than the data set and procedures applied in the current chapter.

Chapter 5
Conclusions and Future Directions

5.1 Conclusions

In this thesis, I present advances in surface wave studies, including wavefield simulation of surface wave propagating in 3D complex Earth and imaging shear wave isotropic and anisotropic structures with surface wave tomography.

Chapter 2 explores the nature of elastic propagation effects on short period surface waves, particularly their amplitudes downstream from sedimentary basins. My results show that a significant fraction of amplitude variability observed in regionally propagating surface waves (e.g., Bonner et al., 2008) is caused by elastic focusing/defocusing due to lateral wave propagation effects through shallow structures. The focus of this study is to understand elastic focusing effects on Rayleigh waves at 10 sec period, which is typically well excited by small earthquakes and nuclear explosions and is also well represented in ambient noise cross-correlations that are commonly used in tomographic studies. The existence and nature of sedimentary basins strongly affect regionally propagating Rayleigh waves at this period. This chapter present a good example how a high-resolution 3D Earth model could be used to better understand wave propagation phenomena in complex Earth, providing us new insights to improve studies such as estimates of source characteristics, the inference of the anelastic structure of the Earth, and ground motion predictions for hazard assessment.

Chapter 3 is an application of surface wave tomography, in which I use mostly advanced techniques in including eikonal tomography and Bayesian Monte Carlo algorithm to infer the crust and uppermost mantle shear wave structures beneath Alaska. The model I present in the chapter is

a radially anisotropic 3-D model of Vsv and Vsh using Rayleigh wave group and phase speed and Love wave phase speed measurements. Prominent features resolved in the model include: (1) Apparent crustal radial anisotropy is strongest across the parts of central and northern Alaska that were subject to significant extension during the Cretaceous, consistent with crustal anisotropy being caused by deformationally-aligned middle to lower crustal sheet silicates (micas) with shallowly dipping foliation planes beneath extensional domains. (2) Crustal thickness estimates are similar to those from receiver functions by Miller & Moresi (2018). (3) Very thick lithosphere underlies Arctic-Alaska, with high shear wave speeds that extend at least to 120 km depth, which may challenge rotational transport models for the evolution of the region. (4) Subducting lithosphere beneath Alaska is resolved, including what we call the "Barren Islands slab anomaly", an "aseismic slab edge" north of the Denali Volcanic Gap, the "Wrangellia slab anomaly", and Yakutat lithosphere subducting seaward of the Wrangell volcanic field. (5) The geometry of the Alaskan subduction zone generally agrees with the slab model Alaska_3D 1.0 of Jadamec & Billen (2010) except for the Yakutat "slab shoulder region", which is newly imaged in our model.

Chapter 4 is a complementary study of Chapter 3, in which I present a shear wave azimuthally anisotropic model of the crust and uppermost mantle beneath Alaska and surroundings, based on seismic data recorded from more than 500 broadband stations. The model is a simple two-layer anisotropic model with anisotropy confined in the brittle upper crust and uppermost mantle. This study is essentially a hypothesis test to verify if such a model can reasonably predict azimuthal variation in Rayleigh wave phase speed measurements. I find that such a simple two-layer model passes the hypothesis test for most of the region of study, from which I draw two conclusions. (a) The data are consistent with crustal azimuthal anisotropy being dominantly controlled by deformationally-aligned cracks and fractures in the upper crust undergoing brittle deformation. (b)

The data are also consistent with the uppermost mantle beneath Alaska and surroundings experiencing vertically coherent deformation. There are two exceptions to the latter conclusion, for the Alexander Terrane and Koyukuk Terrane where two anisotropic layers in the mantle are required to fit the data. The model also resolves several prominent features. (1) In the upper crust, fast direction alignment is largely associated with the orientation of major fault lines. (2) In the upper mantle, fast directions are regionalized such that the fast axes are aligned with the compressional direction in compressional domains and oriented parallel to the tensional direction in tensional domains. (3) The mantle fast directions located near the Alaska-Aleutian subduction zone and the surrounding back-arc area compose a toroidal pattern that is consistent with mantle flow directions predicted by geodynamical modelling (Jadamec & Billen, 2010).

5.2 Future Directions

In the future, there are several areas that can be further explored. For Chapter 2, it is important to test the principal conclusions of the chapter with real data. This will include tests to observe strong lineations or amplification stripes downstream from sedimentary basins, and perhaps also the de-amplification and propagation deflection stripes that bracket the amplification. In addition, it is also important to test whether the observed features are predicted well with high quality velocity models. To achieve this, there are three major requirements that need to be satisfied. (1) A dense array with high quality seismometers is needed to record accurate spatially resolved amplitude information. The array should be located near to a large sedimentary basin. (2) Seismic events upstream from the basin are also needed with magnitudes large enough to be recorded by the array. Ideally, they would also be small enough and far enough to be considered as point sources. (3) A high-resolution 3D model (or 2D phase velocity map) also should be available for the study region.

For Chapter 3 and 4, it is worthwhile to combine Rayleigh wave azimuthally anisotropic measurements with Love waves to achieve more complete estimates of the elastic tensor and inference of inherent anisotropy, as performed by Xie et al., (2015, 2017) for Western United States and Tibet. This approach is able to reconcile apparent radial and azimuthal anisotropy and thus could possibly provide better depth constraint in anisotropy. It is also important to introduce other types of datasets, including shear wave splitting, receiver functions and H/V ratios to better constrain the anisotropic structures. Those complementary datasets are particularly important to better infer sedimentary and crustal anisotropy.

Bibliography

Aki, K. and Larner, K.L., 1970. Surface motion of a layered medium having an irregular interface due to incident plane SH waves. *Journal of geophysical research*, *75*(5), pp.933-954.

Alex, C.M. and Olsen, K.B., 1998. Lens-effect in Santa Monica? *Geophysical research letters*, *25*(18), pp.3441-3444.

Allam, A.A., Schulte-Pelkum, V., Ben-Zion, Y., Tape, C., Ruppert, N. and Ross, Z.E., 2017. Ten kilometer vertical Moho offset and shallow velocity contrast along the Denali fault zone from double-difference tomography, receiver functions, and fault zone head waves. *Tectonophysics*, *721*, pp.56-69.

Amante, C. and Eakins, B.W., 2009. ETOPO1 arc-minute global relief model: procedures, data sources and analysis.

Babuska, V. and Cara, M., 1991. *Seismic anisotropy in the Earth* (Vol. 10). Springer Science & Business Media.

Backus, G.E., 1962. Long-wave elastic anisotropy produced by horizontal layering, J. geophys. Res., 67(11), 4427–4440.

Bao, X., Dalton, C.A. and Ritsema, J., 2016. Effects of elastic focusing on global models of Rayleigh wave attenuation. *Geophysical Journal International*, *207*(2), pp.1062-1079. Bard, P.Y. and Bouchon, M., 1980a. The seismic response of sediment-filled valleys. Part 1. The case of incident SH waves. *Bulletin of the seismological society of America*, *70*(4), pp.1263-1286.

Bard, P.Y. and Bouchon, M., 1980a. The seismic response of sediment-filled valleys. Part 1. The case of incident SH waves. *Bulletin of the seismological society of America*, *70*(4), pp.1263-1286.

Bard, P.Y. and Bouchon, M., 1980b. The seismic response of sediment-filled valleys. Part 2. The case of incident P and SV waves. *Bulletin of the Seismological Society of America*, *70*(5), pp.1921-1941.

Bard, P.Y., Campillo, M., Chavez-Garcia, F.J. and Sanchez-Sesma, F., 1988. The Mexico earthquake of September 19, 1985—A theoretical investigation of large-and small-scale amplification effects in the Mexico City Valley. *Earthquake spectra*, *4*(3), pp.609-633.

Barmin, M.P., Ritzwoller, M.H. and Levshin, A.L., 2001. A fast and reliable method for surface wave tomography. In *Monitoring the Comprehensive Nuclear-Test-Ban Treaty: Surface Waves* (pp. 1351-1375). Birkhäuser, Basel.

Bensen, G.D., Ritzwoller, M.H., Barmin, M.P., Levshin, A.L., Lin, F., Moschetti, M.P., Shapiro, N.M. and Yang, Y., 2007. Processing seismic ambient noise data to obtain reliable broad-band surface wave dispersion measurements. *Geophysical Journal International*, *169*(3), pp.1239-1260.

Berenger, J.P., 1994. A perfectly matched layer for the absorption of electromagnetic waves. *Journal of computational physics*, *114*(2), pp.185-200.

Bird, K.J. and Molenaar, C.M., 1992. The North Slope Foreland Basin, Alaska: Chapter 13.

Bonner, J., Herrmann, R.B., Harkrider, D. and Pasyanos, M., 2008. The surface wave magnitude for the 9 October 2006 North Korean nuclear explosion. *Bulletin of the Seismological Society of America*, *98*(5), pp.2498-2506.

Bowden, D.C. and Tsai, V.C., 2017. Earthquake ground motion amplification for surface waves. Geophys. Res. Lett., 44, 121–127, doi:10.1002/2016GL071885

Bowers, D. and Selby, N.D., 2009. Forensic seismology and the comprehensive nuclear-test-ban treaty. *Annual Review of Earth and Planetary Sciences*, *37*, pp.209-236.

Brocher, T.M., 2005. Empirical relations between elastic wavespeeds and density in the Earth's crust. *Bulletin of the seismological Society of America*, *95*(6), pp.2081-2092.

Christensen, D.H. and Abers, G.A., 2010. Seismic anisotropy under central Alaska from SKS splitting observations. *Journal of Geophysical Research: Solid Earth*, *115*(B4).

Clouser, R.H. and Langston, C.A., 1991. Qp-Qs relations in a sedimentary basin using converted phases. *Bulletin of the Seismological Society of America*, *81*(3), pp.733-750.

Coney, P.J. and Jones, D.L., 1985. Accretion tectonics and crustal structure in Alaska. *Tectonophysics*, *119*(1-4), pp.265-283.

Crampin, S., 1984. Effective anisotropic elastic constants for wave propagation through cracked solids. *Geophysical Journal International*, *76*(1), pp.135-145.

Dahlen, F. and Tromp, J., 1998. Theoretical global seismology. *Princeton University Press*.

Deng, Y., Shen, W., Xu, T. and Ritzwoller, M.H., 2015. Crustal layering in northeastern Tibet: A case study based on joint inversion of receiver functions and surface wave dispersion. *Geophysical Journal International*, *203*(1), pp.692-706.

Dalton, C.A. and Ekström, G., 2006. Global models of surface wave attenuation. *Journal of Geophysical Research: Solid Earth*, *111*(B5).

Dalton, C.A., Ekström, G. and Dziewoński, A.M., 2008. The global attenuation structure of the upper mantle. *Journal of Geophysical Research: Solid Earth*, *113*(B9).

Day, S.M., Roten, D. and Olsen, K.B., 2012. Adjoint analysis of the source and path sensitivities of basin-guided waves. *Geophysical Journal International*, *189*(2), pp.1103-1124.

Denolle, M.A., Dunham, E.M., Prieto, G.A. and Beroza, G.C., 2014. Strong ground motion prediction using virtual earthquakes. *Science*, *343*(6169), pp.399-403.

Durek, J.J. and Ekström, G., 1996. A radial model of anelasticity consistent with long-period surface-wave attenuation. *Bulletin of the Seismological Society of America*, *86*(1A), pp.144-158.

Eberhart-Phillips, D., Christensen, D.H., Brocher, T.M., Hansen, R., Ruppert, N.A., Haeussler, P.J. and Abers, G.A., 2006. Imaging the transition from Aleutian subduction to Yakutat collision in central Alaska, with local earthquakes and active source data. *Journal of Geophysical Research: Solid Earth*, *111*(B11).

Ekström, G. and Dziewonski, A.M., 1998. The unique anisotropy of the Pacific upper mantle. *Nature*, *394*(6689), p.168.

Ekström, G., 2011. A global model of Love and Rayleigh surface wave dispersion and anisotropy, 25-250 s. *Geophysical Journal International*, *187*(3), pp.1668-1686.

Erdman, M.E., Hacker, B.R., Zandt, G. and Seward, G., 2013. Seismic anisotropy of the crust: electron-backscatter diffraction measurements from the Basin and Range. *Geophysical Journal International*, *195*(2), pp.1211-1229.

Feng, L. and Ritzwoller, M.H., 2017. The effect of sedimentary basins on surface waves that pass through them. *Geophysical Journal International*, *211*(1), pp.572-592.

Feng, L., and M.H.Ritzwoller, 2019. A 3-D shear velocity model of the crust and uppermost mantle beneath Alaska including apparent radial anisotropy, *J. Geophys. Res. Solid Earth*, submitted

Ferreira, A.M.G., Woodhouse, J.H., Visser, K. and Trampert, J., 2010. On the robustness of global radially anisotropic surface wave tomography. *Journal of Geophysical Research: Solid Earth*, *115*(B4).

Ferris, A., Abers, G.A., Christensen, D.H. and Veenstra, E., 2003. High resolution image of the subducted Pacific (?) plate beneath central Alaska, 50–150 km depth. *Earth and Planetary Science Letters*, *214*(3-4), pp.575-588.

Freymueller, J.T., Woodard, H., Cohen, S.C., Cross, R., Elliott, J., Larsen, C.F., Hreinsdottir, S., Zweck, C., Haeussler, P.J., Wesson, R.L. and Ekström, G., 2008. Active deformation processes in Alaska, based on 15 years of GPS measurements. *Active tectonics and seismic potential of Alaska*, *179*, pp.1-42.

Fuis, G.S., Levander, A.R., Lutter, W.J., Wissinger, E.S., Moore, T.E. and Christensen, N.I., 1995. Seismic images of the Brooks Range, Arctic Alaska, reveal crustal-scale duplexing. *Geology*, *23*(1), pp.65-68.

Fuis, G.S., Moore, T.E., Plafker, G., Brocher, T.M., Fisher, M.A., Mooney, W.D., Nokleberg, W.J., Page, R.A., Beaudoin, B.C., Christensen, N.I. and Levander, A.R., 2008. Trans-Alaska Crustal Transect and continental evolution involving subduction underplating and synchronous foreland thrusting. *Geology*, *36*(3), pp.267-270.

Gokhberg, A. and Fichtner, A., 2016. Full-waveform inversion on heterogeneous HPC systems. *Computers & Geosciences*, *89*, pp.260-268.

Gou, T., Zhao, D., Huang, Z. and Wang, L., 2019. Aseismic deep slab and mantle flow beneath Alaska: Insight from anisotropic tomography. *Journal of Geophysical Research: Solid Earth*, *124*(2), pp.1700-1724.

Graves, R., Jordan, T.H., Callaghan, S., Deelman, E., Field, E., Juve, G., Kesselman, C., Maechling, P., Mehta, G., Milner, K. and Okaya, D., 2011. CyberShake: A physics-based seismic hazard model for southern California. *Pure and Applied Geophysics*, *168*(3-4), pp.367-381.

Hacker, B.R. and Abers, G.A., 2004. Subduction Factory 3: An Excel worksheet and macro for calculating the densities, seismic wave speeds, and H2O contents of minerals and rocks at pressure and temperature. *Geochemistry, Geophysics, Geosystems*, *5*(1).

Hacker, B.R., Ritzwoller, M.H. and Xie, J., 2014. Partially melted, mica-bearing crust in Central Tibet. *Tectonics*, *33*(7), pp.1408-1424.

Hanna, J. and Long, M.D., 2012. SKS splitting beneath Alaska: Regional variability and implications for subduction processes at a slab edge. *Tectonophysics*, *530*, pp.272-285.

Hayes, G.P., Wald, D.J. and Johnson, R.L., 2012. Slab1. 0: A three-dimensional model of global subduction zone geometries. *Journal of Geophysical Research: Solid Earth*, *117*(B1).

Haynie, K.L. and Jadamec, M.A., 2017. Tectonic drivers of the Wrangell block: Insights on fore-arc sliver processes from 3-D geodynamic models of Alaska. *Tectonics*, *36*(7), pp.1180-1206.

Heintz, M. and Kennett, B.L., 2005. Continental scale shear wave splitting analysis: investigation of seismic anisotropy underneath the Australian continent. *Earth and Planetary Science Letters*, *236*(1-2), pp.106-119.

Herrmann, R.B., 2013. Computer programs in seismology: An evolving tool for instruction and research. *Seismological Research Letters*, *84*(6), pp.1081-1088.

Jadamec, M.A. and Billen, M.I., 2010. Reconciling surface plate motions with rapid three-dimensional mantle flow around a slab edge. *Nature*, *465*(7296), p.338.

Jiang, C., Schmandt, B., Ward, K.M., Lin, F.C. and Worthington, L.L., 2018. Upper Mantle Seismic Structure of Alaska From Rayleigh and S Wave Tomography. *Geophysical Research Letters*, *45*(19), pp. 10,350 - 10,359

Johnston, S.T., 2001. The Great Alaskan Terrane Wreck: reconciliation of paleomagnetic and geological data in the northern Cordillera. *Earth and Planetary Science Letters*, *193*(3-4), pp.259-272.

Kang, D., Shen, W., Ning, J. & Ritzwoller, M.H., 2016. Crustal and uppermost mantle structure beneath northeastern China from joint inversion of receiver functions, Rayleigh wave dispersion, and Rayleigh wave ellipticity, Geophys. J. Int., 204(1), 215–235.

Kawase, H., 1996. The cause of the damage belt in Kobe: "The basin-edge effect," constructive interference of the direct S-wave with the basin-induced diffracted/Rayleigh waves. *Seismological Research Letters*, *67*(5), pp.25-34.

Kennett, B.L., Engdahl, E.R. and Buland, R., 1995. Constraints on seismic velocities in the Earth from traveltimes. *Geophysical Journal International*, *122*(1), pp.108-124.

Kirkpatrick, S., Gelatt, C.D. and Vecchi, M.P., 1983. Optimization by simulated annealing. *science*, *220*(4598), pp.671-680.

Klemperer, S.L., 2006. Crustal flow in Tibet: a review of geophysical evidence for the physical state of Tibetan lithosphere. In: Searle, M.P., Law, R.D. (Eds.), Channel Flow, Ductile Extrusion and Exhumation of Lower Mid-crust in Continental Collision Zones: Geol. Soc. Spec. Publ., 268, pp. 39–70, 2006.

Köhler, A., Weidle, C. and Maupin, V., 2012. On the effect of topography on surface wave propagation in the ambient noise frequency range. *Journal of seismology*, *16*(2), pp. pp.221-231.

Komatitsch, D. and Tromp, J., 1999. Introduction to the spectral element method for three-dimensional seismic wave propagation. *Geophysical journal international*, *139*(3), pp. 806-822.

Komatitsch, D., Martin, R., Tromp, J., Taylor, M.A. and Wingate, B.A., 2001. Wave propagation in 2-D elastic media using a spectral element method with triangles and quadrangles. *Journal of Computational Acoustics*, *9*(02), pp.703-718.

Komatitsch, D., Barnes, C. and Tromp, J., 2000. Wave propagation near a fluid-solid interface: A spectral-element approach. *Geophysics*, *65*(2), pp.623-631.

Koper, K.D., Herrmann, R.B. and Benz, H.M., 2008. Overview of open seismic data from the North Korean event of 9 October 2006. *Seismological Research Letters*, *79*(2), pp.178-185.

Kustowski, B., Ekström, G. and Dziewoński, A.M., 2008. Anisotropic shear-wave velocity structure of the Earth's mantle: A global model. *Journal of Geophysical Research: Solid Earth*, *113*(B6).

Laske, G., Masters, G., Ma, Z. and Pasyanos, M., 2013, April. Update on CRUST1. 0—A 1-degree global model of Earth's crust. In *Geophys. Res. Abstr* (Vol. 15, p. 2658). Vienna, Austria: EGU General Assembly.

Lawrence, J.F. and Prieto, G.A., 2011. Attenuation tomography of the western United States from ambient seismic noise. *Journal of Geophysical Research: Solid Earth*, *116*(B6).

Lay, T. and Kanamori, H., 1985. Geometric effects of global lateral heterogeneity on long-period surface wave propagation. *Journal of Geophysical Research: Solid Earth*, *90*(B1), pp.605-621.

Levandowski, W., Jones, C.H., Shen, W., Ritzwoller, M.H. and Schulte-Pelkum, V., 2014. Origins of topography in the western US: Mapping crustal and upper mantle density variations using a uniform seismic velocity model. *Journal of Geophysical Research: Solid Earth*, *119*(3), pp.2375-2396.

Levshin, A.L. & Ritzwoller, M.H., 2001. Automated detection, extraction, and measurement of regional surface waves, Pure appl. Geophys., 158(8), 1531–1545.

Levshin, A.L., Pisarenko, V.F. & Pogrebinsky, G.A., 1972. On a frequency time analysis of oscillations, Ann. Geophys., 28, 211–218.

Levshin, A.L., Yang, X., Barmin, M.P. and Ritzwoller, M.H., 2010. Midperiod Rayleigh wave attenuation model for Asia. *Geochemistry, Geophysics, Geosystems*, *11*(8).

Lin, F.C. and Ritzwoller, M.H., 2011. Helmholtz surface wave tomography for isotropic and azimuthally anisotropic structure. *Geophysical Journal International*, *186*(3), pp.1104-1120.

Lin, F.C., Moschetti, M.P. and Ritzwoller, M.H., 2008. Surface wave tomography of the western United States from ambient seismic noise: Rayleigh and Love wave phase velocity maps. *Geophysical Journal International*, *173*(1), pp.281-298.

Lin, F.C., Ritzwoller, M.H. and Snieder, R., 2009. Eikonal tomography: surface wave tomography by phase front tracking across a regional broad-band seismic array. *Geophysical Journal International*, *177*(3), pp.1091-1110.

Lin, F.-C., Ritzwoller, M.H., Townend, J., Bannister, S. and Savage, M.K., 2007. Ambient noise Rayleigh wave tomography of New Zealand. *Geophysical Journal International*, *170*(2), pp.649-666.

Lin, F.-C., Schmandt, B. & Tsai, V.C., 2012. Joint inversion of Rayleigh wave phase velocity and ellipticity using USArray: Constraining velocity and density structure in the upper crust, Geophys. Res. Lett., 39(12), doi:10.1029/2012GL052196.

Long, M.D. and Silver, P.G., 2008. The subduction zone flow field from seismic anisotropy: A global view. *science*, *319*(5861), pp.315-318.

Long, M.D., 2013. Constraints on subduction geodynamics from seismic anisotropy. *Reviews of Geophysics*, *51*(1), pp.76-112.

Marone, F., Gung, Y. and Romanowicz, B., 2007. Three-dimensional radial anisotropic structure of the North American upper mantle from inversion of surface waveform data. *Geophysical Journal International*, *171*(1), pp.206-222.

Marquering, H., Dahlen, F.A. and Nolet, G., 1999. Three-dimensional sensitivity kernels for finite-frequency traveltimes: the banana-doughnut paradox. *Geophysical Journal International*, *137*(3), pp.805-815.

Martin-Short, R., Allen, R.M. and Bastow, I.D., 2016. Subduction geometry beneath south central

Alaska and its relationship to volcanism. *Geophysical Research Letters*, *43*(18), pp.9509-9517.

Martin-Short, R., Allen, R., Bastow, I.D., Porritt, R.W. and Miller, M.S., 2018. Seismic imaging of the Alaska subduction zone: Implications for slab geometry and volcanism. *Geochemistry, Geophysics, Geosystems*, *19*(11), pp.4541-4560.

Miller, E.L. and Hudson, T.L., 1991. Mid-Cretaceous extensional fragmentation of a Jurassic-Early Cretaceous compressional orogen, Alaska. *Tectonics*, *10*(4), pp.781-796.

Miller, M.S. and Moresi, L., 2018. Mapping the Alaskan Moho. *Seismological Research Letters*, *89*(6), pp.2430-2436.

Miller, M.S., O'Driscoll, L.J., Porritt, R.W. and Roeske, S.M., 2018. Multiscale crustal architecture of Alaska inferred from P receiver functions. *Lithosphere*, *10*(2), pp.267-278.

Molnar, P. and Tapponnier, P., 1981. A possible dependence of tectonic strength on the age of the crust in Asia. *Earth and Planetary Science Letters*, *52*(1), pp.107-114.

Montagner, J.-P. & Nataf, H.-C., 1986. A simple method for inverting the azimuthal anisotropy of surface waves, J. geophys. Res., 91(B1), 511, doi:10.1029/JB091iB01p00511.

Montagner, J.P. and Tanimoto, T., 1991. Global upper mantle tomography of seismic velocities and anisotropies. *Journal of Geophysical Research: Solid Earth*, *96*(B12), pp.20337-20351.

Moore, T.E. and Box, S.E., 2016. Age, distribution and style of deformation in Alaska north of 60 N: Implications for assembly of Alaska. *Tectonophysics*, *691*, pp.133-170.

Moschetti, M.P., Ritzwoller, M.H., Lin, F. and Yang, Y., 2010. Seismic evidence for widespread western-US deep-crustal deformation caused by extension. *Nature*, *464*(7290), p.885

Mosegaard, K. and Tarantola, A., 1995. Monte Carlo sampling of solutions to inverse problems. *Journal of Geophysical Research: Solid Earth*, *100*(B7), pp.12431-12447.

Tarantola, A., 2005. Inverse problem theory and methods for model parameter estimation (Vol. 89). *siam*.

Nettles, M. and Dziewoński, A.M., 2008. Radially anisotropic shear velocity structure of the upper mantle globally and beneath North America. *Journal of Geophysical Research: Solid Earth*, *113*(B2).

Nilsen, T.H. and Zuffa, G.G., 1982. The Chugach terrane, a Cretaceous trench-fill deposit, southern Alaska. *Geological Society, London, Special Publications*, *10*(1), pp.213-227.

Nokleberg, W.J., Jones, D.L. and Silberling, N.J., 1985. Origin and tectonic evolution of the Maclaren and Wrangellia terranes, eastern Alaska Range, Alaska. *Geological Society of America Bulletin*, *96*(10), pp.1251-1270.

Nolet, G. and Dahlen, F.A., 2000. Wave front healing and the evolution of seismic delay times. *Journal of Geophysical Research: Solid Earth*, *105*(B8), pp.19043-19054.

O'Driscoll, L.J. and Miller, M.S., 2015. Lithospheric discontinuity structure in Alaska, thickness variations determined by Sp receiver functions. *Tectonics*, *34*(4), pp.694-714.

Olsen, K.B., Archuleta, R.J. and Matarese, J.R., 1995. Three-dimensional simulation of a magnitude 7.75 earthquake on the San Andreas fault. *Science*, *270*(5242), p.1628.

Olsen, K.B., 2000. Site amplification in the Los Angeles basin from three-dimensional modeling of ground motion. *Bulletin of the Seismological Society of America*, *90*(6B), pp.S77-S94.

Olsen, K.B., Day, S.M., Minster, J.B., Cui, Y., Chourasia, A., Faerman, M., Moore, R., Maechling, P. and Jordan, T., 2006. Strong shaking in Los Angeles expected from southern San Andreas earthquake. *Geophysical Research Letters*, *33*(7).

Olsen, K.B., Day, S.M., Dalguer, L.A., Mayhew, J., Cui, Y., Zhu, J., Cruz-Atienza, V.M., Roten, D., Maechling, P., Jordan, T.H. and Okaya, D., 2009. ShakeOut-D: Ground motion estimates using an ensemble of large earthquakes on the southern San Andreas fault with spontaneous rupture propagation. *Geophysical Research Letters*, *36*(4).

Perttu, A., Christensen, D., Abers, G. and Song, X., 2014. Insights into mantle structure and flow beneath Alaska based on a decade of observations of shear wave splitting. *Journal of Geophysical Research: Solid Earth*, *119*(11), pp.8366-8377.

Petersson, N.A. and Sjogreen, B., 2014. User's guide to SW4, version 1.1. *LLNL-SM-662014, Lawrence Livermore National Laboratory*.

Prieto, G.A., Lawrence, J.F. and Beroza, G.C., 2009. Anelastic Earth structure from the coherency of the ambient seismic field. *Journal of Geophysical Research: Solid Earth*, *114*(B7).

Rawlinson, N. and Sambridge, M., 2004. Wave front evolution in strongly heterogeneous layered media using the fast marching method. *Geophysical Journal International*, *156*(3), pp.631-647.

Redfield, T.F., Scholl, D.W., Fitzgerald, P.G. and Beck Jr, M.E., 2007. Escape tectonics and the extrusion of Alaska: Past, present, and future. *Geology*, *35*(11), pp.1039-1042.

Riley, K.F., Hobson, M.P. and Bence, S.J., 2006. Mathematical Methods for Physics and Engineering: A Comprehensive Guide. *Cambridge University Press.*

Ritzwoller, M.H. and Feng, L.I.L.I., 2018. Overview of pre-and post-processing of ambient noise correlations. Seismic Ambient Noise. *Cambridge University Press.*

Ritzwoller, M.H., Lin, F.C. and Shen, W., 2011. Ambient noise tomography with a large seismic array. *Comptes Rendus Geoscience*, *343*(8-9), pp.558-570.

Rondenay, S., Montési, L.G. and Abers, G.A., 2010. New geophysical insight into the origin of the Denali volcanic gap. *Geophysical Journal International*, *182*(2), pp.613-630.

Rouaud M, 2013. Probability, statistics and estimation. Propagation of uncertainties.

Russell, D.R., 2006. Development of a time-domain, variable-period surface-wave magnitude measurement procedure for application at regional and teleseismic distances, part I: Theory. *Bulletin of the Seismological Society of America*, *96*(2), pp.665-677.

Selby, N.D. and Woodhouse, J.H., 2000. Controls on Rayleigh wave amplitudes: attenuation and focusing. *Geophysical Journal International*, *142*(3), pp.933-940.

Selby, N.D., Marshall, P.D. and Bowers, D., 2012. mb: Ms event screening revisited. *Bulletin of the Seismological Society of America*, *102*(1), pp.88-97.

Savage, M.K., Silver, P.G. and Meyer, R.P., 1990. Observations of teleseismic shear-wave splitting in the Basin and Range from portable and permanent stations. *Geophysical Research Letters*, *17*(1), pp.21-24.

Savage, M.K., 1999. Seismic anisotropy and mantle deformation: what have we learned from shear wave splitting?. *Reviews of Geophysics*, *37*(1), pp.65-106.

Shapiro, N.M., Campillo, M., Stehly, L. and Ritzwoller, M.H., 2005. High-resolution surface-wave tomography from ambient seismic noise. *Science*, *307*(5715), pp.1615-1618.

Shapiro, N.M. and Ritzwoller, M.H., 2002. Monte-Carlo inversion for a global shear-velocity model of the crust and upper mantle. *Geophysical Journal International*, *151*(1), pp.88-105.

Shapiro, N.M., Ritzwoller, M.H., Molnar, P. and Levin, V., 2004. Thinning and flow of Tibetan crust constrained by seismic anisotropy. *Science*, *305*(5681), pp.233-236.

Shen, W. and Ritzwoller, M.H., 2016. Crustal and uppermost mantle structure beneath the United States. *Journal of Geophysical Research: Solid Earth*, *121*(6), pp.4306-4342.

Shen, W., Ritzwoller, M.H., Schulte-Pelkum, V. and Lin, F.C., 2012. Joint inversion of surface wave dispersion and receiver functions: a Bayesian Monte-Carlo approach. *Geophysical Journal International*, *192*(2), pp.807-836.

Shen, W., Ritzwoller, M.H., Kang, D., Kim, Y., Lin, F.C., Ning, J., Wang, W., Zheng, Y. and Zhou, L., 2016. A seismic reference model for the crust and uppermost mantle beneath China from surface wave dispersion. *Geophysical Journal International*, *206*(2), pp.954-979.

Shin, J.S., Sheen, D.H. and Kim, G., 2010. Regional observations of the second North Korean nuclear test on 2009 May 25. *Geophysical Journal International*, *180*(1), pp.243-250.

Silver, P.G. and Savage, M.K., 1994. The interpretation of shear-wave splitting parameters in the presence of two anisotropic layers. *Geophysical Journal International*, *119*(3), pp.949-963.

Silver, P.G. and Chan, W.W., 1988. Implications for continental structure and evolution from seismic anisotropy. *Nature*, *335*(6185), p.34.

Silver, P.G., 1996. Seismic anisotropy beneath the continents: Probing the depths of geology. *Annual review of earth and planetary sciences*, *24*(1), pp.385-432.

Smith, D.B., Ritzwoller, M.H. and Shapiro, N.M., 2004. Stratification of anisotropy in the Pacific upper mantle. *Journal of Geophysical Research: Solid Earth*, *109*(B11).

Stacey, R., 1988. Improved transparent boundary formulations for the elastic wave equation, Bull. seism. Soc. Am., 78, 2089–2097.

Thomsen, L., 1986. Weak elastic anisotropy. *Geophysics*, *51*(10), pp.1954-1966.

You, T. and Zhao, D., 2012. Seismic anisotropy and heterogeneity in the Alaska subduction zone. *Geophysical Journal International*, *190*(1), pp.629-649.

Trampert J., van Heijst H. J., 2002. Global azimuthal anisotropy in the transition zone, Science, 296, 1297-1299.

Vinnik, L.P., Makeyeva, L.I., Milev, A. and Usenko, A.Y., 1992. Global patterns of azimuthal anisotropy and deformations in the continental mantle. *Geophysical Journal International*, *111*(3), pp.433-447.

Wang, Z., Dahlen, F.A. and Tromp, J., 1993. Surface wave caustics. *Geophysical Journal International*, *114*(2), pp.311-324.

Wang, Z. and Dahlen, F.A., 1995. Validity of surface-wave ray theory on a laterally heterogeneous earth. *Geophysical Journal International*, *123*(3), pp.757-773.

Wang, Y. and Tape, C., 2014. Seismic velocity structure and anisotropy of the Alaska subduction zone based on surface wave tomography. *Journal of Geophysical Research: Solid Earth*, *119*(12), pp.8845-8865.

Ward, K.M., 2015. Ambient noise tomography across the southern Alaskan Cordillera. *Geophysical Research Letters*, *42*(9), pp.3218-3227.

Ward, K.M. and Lin, F.C., 2018. Lithospheric structure across the Alaskan cordillera from the joint inversion of surface waves and receiver functions. *Journal of Geophysical Research: Solid Earth*, *123*(10), pp.8780-8797.

Wiemer, S., Tytgat, G., Wyss, M. and Duenkel, U., 1999. Evidence for shear-wave anisotropy in the mantle wedge beneath south central Alaska. *Bulletin of the Seismological Society of America*, *89*(5), pp.1313-1322.

Woodhouse, J.H. and Wong, Y.K., 1986. Amplitude, phase and path anomalies of mantle waves. *Geophysical Journal International*, *87*(3), pp.753-773.

Xie, J., Ritzwoller, M.H., Shen, W., Yang, Y., Zheng, Y. and Zhou, L., 2013. Crustal radial anisotropy across eastern Tibet and the western Yangtze craton. *Journal of Geophysical Research: Solid Earth*, *118*(8), pp.4226-4252.

Xie, J., Ritzwoller, M.H., Brownlee, S.J. and Hacker, B.R., 2015. Inferring the oriented elastic tensor from surface wave observations: preliminary application across the western United States. *Geophysical Journal International*, *201*(2), pp.996-1021.

Xie, J., Ritzwoller, M.H., Shen, W. and Wang, W., 2017. Crustal anisotropy across eastern Tibet and surroundings modeled as a depth-dependent tilted hexagonally symmetric medium. *Geophysical Journal International*, *209*(1), pp.466-491.

Yang, X., and H. Gao, 2019. Seismic imaging of slab segmentation and correlation with volcano distribution along the Aleutian-Alaska subduction zone, Nature Communications, submitted.

Yang, X., Fischer, K.M. and Abers, G.A., 1995. Seismic anisotropy beneath the Shumagin Islands segment of the Aleutian-Alaska subduction zone. *Journal of Geophysical Research: Solid Earth*, *100*(B9), pp.18165-18177.

Yang, Y. and Forsyth, D.W., 2006. Regional tomographic inversion of the amplitude and phase of Rayleigh waves with 2-D sensitivity kernels. *Geophysical Journal International*, *166*(3), pp.1148-1160.

Yang, Y., Ritzwoller, M.H., Levshin, A.L. and Shapiro, N.M., 2007. Ambient noise Rayleigh wave tomography across Europe. *Geophysical Journal International*, *168*(1), pp.259-274.

Yuan, H.Y., Romanowicz, B., Fischer, K.M. & Abt, D., 2011. 3-D shear wave radially and azimuthally anisotropic velocity model of the North American upper mantle, Geophysical Journal International, 184**,** 1237-1260.

Zhang, Y., Li, A. and Hu, H., 2019. Crustal Structure in Alaska From Receiver Function Analysis. *Geophysical Research Letters*, *46*(3), pp.1284-1292.

Zhao, D., Christensen, D. and Pulpan, H., 1995. Tomographic imaging of the Alaska subduction zone. *Journal of Geophysical Research: Solid Earth*, *100*(B4), pp.6487-6504.

Zhao, L.F., Xie, X.B., Wang, W.M. and Yao, Z.X., 2008. Regional seismic characteristics of the 9 October 2006 North Korean nuclear test. *Bulletin of the Seismological Society of America*, *98*(6), pp.2571-2589.